FIRST PRINCIPLE CALCULATION OF CATALYTIC ACTIVITY OF PALLADIUM AND PLATINUM ALLOY WITH NON-PRECIOUS METALS

NANYANG TECHNOLOGICAL UNIVERSITY
SINGAPORE

FIRST PRINCIPLE CALCULATION OF CATALYTIC ACTIVITY OF PALLADIUM AND PLATINUM ALLOY WITH NON-PRECIOUS METALS

LIU JI

LIU JI

SCHOOL OF ELECTRICAL & ELECTRONIC ENGINEERING

2019

2019

FIRST PRINCIPLE CALCULATION OF CATALYTIC ACTIVITY OF PALLADIUM AND PLATINUM ALLOY WITH NON-PRECIOUS METALS

LIU JI

LIU JI

School of Electrical & Electronic Engineering

A thesis submitted to the Nanyang Technological University
in partial fulfillment of the requirement for the degree of
Doctor of Philosophy

2019

Statement of Originality

I hereby certify that the work embodied in this thesis is the result of original research, is free of plagiarised materials, and has not been submitted for a higher degree to any other University or Institution.

[2019-01-16]	[Ji Liu]
. . . . .	. . . . .
Date	[Ji Liu]

Supervisor Declaration Statement

I have reviewed the content and presentation style of this thesis and declare it is free of plagiarism and of sufficient grammatical clarity to be examined. To the best of my knowledge, the research and writing are those of the candidate except as acknowledged in the Author Attribution Statement. I confirm that the investigations were conducted in accord with the ethics policies and integrity standards of Nanyang Technological University and that the research data are presented honestly and without prejudice.

2019-01-16	Sun Changqing
. . . .	. . . .
Date	[Prof. Sun Changqing]

Authorship Attribution Statement

This thesis contains material from 4 paper(s) published in the following peer-reviewed journal(s) where I was the first and/or corresponding author.

Chapter 4 is published as Liu, J.; Fan, X.; Sun, C. Q.; Zhu, W., Layer effect on catalytic activity of Pd-Cu bimetal for CO oxidation. *Applied Catalysis A: General* **2017**, 538, 66-73. DOI: 10.1016/j.apcata.2017.03.019.

The contributions of the co-authors are as follows:

- Dr. Fan xiaofeng and I proposed this idea. Dr. Fan Xiaofeng guided the simulation model and method.
- I performed the DFT calculations. Dr. Fan xiaofeng assisted in data analysis. Prof. Zhu weiguang and Prof. Sun changqing joined the discussion.
- I prepared the manuscript drafts. The manuscript was revised by Dr. Fan Xiaofeng, Prof. Zhu weiguang, and Prof. Sun Changqing.
- Prof. Zhu weiguang provided finial support for HPC.

Chapter 5 is published as Liu, J.; Fan, X.; Sun, C. Q.; Zhu, W., DFT Study on bimetallic Pt/Cu (111) as efficient catalyst for H_2 dissociation. *Applied Surface Science* **2018**, 441, 23-28. DOI: 10.1016/j.apsusc.2018.02.010.

The contributions of the co-authors are as follows:

- Dr. Fan xiaofeng and I proposed this idea. Dr. Fan Xiaofeng guided the simulation model and method.
- I performed the DFT calculations. Dr. Fan xiaofeng assisted in data analysis. Prof. Zhu weiguang and Prof. Sun changqing joined the discussion.

- I prepared the manuscript drafts. The manuscript was revised by Dr. Fan Xiaofeng, Prof. Zhu weiguang, and Prof. Sun Changqing.
- Prof. Zhu weiguang provided finial support for HPC.

Chapter 6 is published as (a) Liu, J.; Fan, X.; Sun, C. Q.; Zhu, W., DFT Study on Intermetallic Pd–Cu alloy with cover layer Pd as efficient catalyst for oxygen reduction reaction. *Materials* **2017**, 11 (1), 33. DOI: 10.3390/ma11010033; (b) Liu, J.; Sun, C.; Zhu, W., Origin of efficient oxygen reduction reaction on Pd monolayer supported on Pd-M (M=Ni, Fe, Fe) intermetallic alloy. *Electrochimica Acta* **2018**, 282, 680-686. DOI: 10.1016/j.electacta.2018.06.041.

The contributions of the co-authors are as follows:

(a)

- Dr. Fan xiaofeng and I proposed this idea.
- I performed the DFT calculations. Dr. Fan xiaofeng assisted in data analysis. Prof. Zhu weiguang and Prof. Sun changqing joined the discussion.
- I prepared the manuscript drafts. The manuscript was revised by Dr. Fan Xiaofeng, Prof. Zhu weiguang, and Prof. Sun Changqing.
- Prof. Zhu weiguang provided finial support for HPC.

(b)

- I proposed this idea.
- I performed the DFT calculations and data analysis. Prof. Zhu weiguang and Prof. Sun changqing joined the discussion.
- I prepared the manuscript drafts. The manuscript was revised by Prof. Zhu weiguang, and Prof. Sun Changqing.
- Prof. Zhu weiguang provided finial support for HPC.

Chapter 7 is not published yet.

The contributions of the co-authors are as follows:

- I proposed this idea.
- I performed the DFT calculations and data analysis.
- I prepared the manuscript drafts. The manuscript was revised by Prof. Zhu weiguang, and Prof. Sun Changqing.
- Prof. Zhu weiguang provided finial support for HPC.

[2019-01-16] [Ji Liu]

. . . .

Date [Ji Liu]

Acknowledgments

To begin with, I would like to give thanks to my supervisor Prof. Zhu Weiguang. During four-year studies, Prof. Zhu gives valuable support to my research. Also I would like to show appreciation to my co-supervisor Prof. Sun Changqing. Working with Prof. Zhu and Prof. Sun is an unique experience in my research career. I am really inspired and impressed by the hard-working attitude of both professors.

Secondly, I would like to thank Dr. Fan Xiaofeng from Jilin University. I have enjoyed the time with Dr. Fan when he was a visiting research fellow in our group. Thanks for the fruitful discussions and useful guidance at the start of my PhD research.

Thirdly, I would also like to thank all the colleagues and friends for the support, encouragement and help during my PhD journey. Special thanks give to Dr. Shideh Ahmadi, Dr. Zhang Xi, Dr. Wang Haibin, Mr. Guo Xiao, Mr. Wang Wei, and Mr. Huang Zhongkai.

Additionally, I would like to show gratitude to my family for their countless support and trust. I specially acknowledge my mother and my brother. Especially, this thesis is dedicated to my father. I miss you so much and you are always in my heart.

Finally, thanks to Nanyang Technological University for offering this opportunity to be enrolled in PhD program.

To my family

Table of Contents

Summary

Noble metals are widely used and researched in heterogeneous catalysis due to remarkable catalytic performance. For years, researchers have dedicated to study the catalytic mechanism in order to enhance the catalytic activity. It is widely known that noble metals are expensive and rare. By alloying, the usage of noble metals can be reduced. The challenge is how to maintain the same or achieve even better catalytic performance with limited usage of noble metals. First principle density functional theory (DFT) calculation provides a powerful way to perform large-scale and high-computing simulations to investigate the design rule in heterogeneous catalysis theoretically.

In this thesis, we have investigated on the catalytic activity of palladium (Pd) and platinum (Pt) based bimetallic alloy by density functional theory calculation. Firstly, we have focused on the layer effect on the catalytic activity of Pd-Cu and Pt-Cu bimetallic alloy. It is found out that the number of Pd (or Pt) cover layer can effectively influence the surface Pd (or Pt) activity. This is explained and supported by the *d*-band center theory, where the *d*-band center of Pd (or Pt) atom is modulated by both the number of cover layer and substrate Cu. The proposed Pd-Cu bimetallic alloy is found to perform effectively as CO oxidation catalyst and the proposed Pt-Cu bimetallic alloy can be used as fuel cell anode materials with enhanced CO-tolerance

ability. Secondly, we have studied the catalytic activity of Pd monolayer model with single-layer Pd on top of Pd-M (M=Cu, Fe and Ni) intermetallic alloy. It is experimentally proved that Pd-Cu alloy can be transformed from face-center cubic (*fcc*) structure to body-center cubic (*bcc*) structure, and Pd-Fe and Pd-Ni alloy can be transformed from *fcc* structure to face-centered tetragonal (*fct*) structure under certain conditions. We have investigated on the activity of these Pd monolayer models as electrocatalysts for oxygen reduction reaction (ORR). Thirdly, in order to achieve the minimization of noble metal usage, we have proposed the Pt-based single-atom alloy (SAA) model with Pt atoms dispersedly doped at Cu nanocluster and studied the catalytic activity for hydrogenation.

List of Figures

List of Tables

Chapter 1 Introduction

1.1 Motivation

Noble metals have been studied for years both experimentally and theoretically since the development of nanotechnology.[1-11] Typically, for heterogeneous catalysis, the noble metal nanoparticles can either be supported on substrate or form alloys to exhibit superior catalytic properties due to the tuning of electronic structure. For supported case, transition metal oxides are often used as substrate and noble metal nanoparticles are anchored on the transition metal oxide surface.[4, 12] For example, the cerium oxide (CeO_2) has long been investigated in heterogeneous catalysis for reforming of methane or water-gas shift when supporting noble metals such as gold and ruthenium.[13-16] The titanium dioxide (TiO_2) is widely applied in heterogeneous catalysis for fuel cells, water-gas shift or CO oxidation when supporting noble metals such as platinum or gold.[3, 7, 17-20] Other chemical reactions such as NO reduction and hydrogenation are also among the practical applications of supported heterogeneous catalysis.[21-23] The theory of strong metal-support interactions (SMSIs) is proposed and applied in supported heterogeneous catalysis case. The size-dependent effect and support effect are two major concepts in supported heterogeneous catalysis. In the early years, the structure, electronic properties and chemical reactivity have been studied and the corresponding surface science techniques have been established.[24-26] Experimentally, the metal oxide can be either thin films or single crystals. During the

process, the morphology, electronic structure and catalytic properties are often investigated by techniques such as X-ray photoelectron spectroscopy (XPS). In this thesis, oxide supported noble metal is excluded. This thesis focuses on metal alloy case and the way of manipulating the catalytic activities are studied and discussed in detail.

The noble metal alloys have long been studied owing to the outstanding catalytic properties.[11, 27-30] Considering the fact that the catalytic reactions occur on the surface of noble metals (also known as active sites), a considerable proportion of the atoms are not utilized. The performance and cost issue are part of the challenges for the application in heterogeneous catalysis. When forming intermetallic alloys or compounds, the properties can be largely extended and the cost is reduced to affordable range. This idea is widely applied in heterogeneous catalysis. However, the types and structures of metal alloys are various and complicated. Possible patterns include core-shell structure, segregated cluster structure, and mixed structure as shown in Figure 1-1.[28] Factors such as relative strength of ironic bond, surface energy and relative atomic sizes determine the favorable patterns. For bimetallic system, three major effects are considered to govern the reactivity: the ligand effect, the ensemble effect and the geometric effect.[11, 31-36] The ligand effect is about the changes in the catalytic selectivity and activity due to the electronic interaction between the two components. The ensemble effect refers to the ensemble of active sites for certain

chemical reactions. The geometric effect results from the lattice mismatch between two metals. Experimentally, the method for generating metal alloys includes molecular beams, ion implantation, and chemical synthesis.[28, 36] Techniques such as mass spectrometry, electron diffraction, and transmission electron microscopy (TEM)

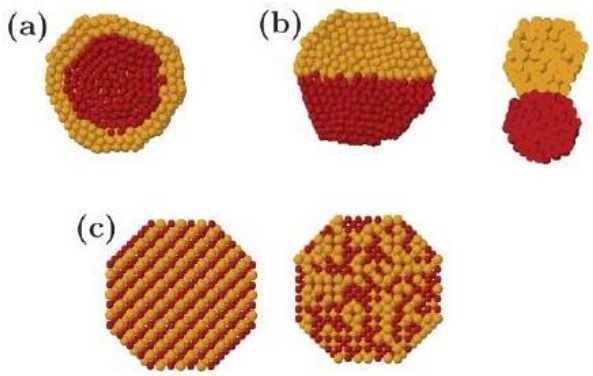

Figure 1-1. The possible patterns of (a) core-shell, (b) segregated cluster, and (c) mixed structure when forming alloys. (Reprinted with permission from Ref.[28])

are applied to characterize and study the alloy structures and properties. From the theoretical point of view, two basic types of methods are developed including cluster model and slab model.[37] Both models are widely applied in heterogeneous catalysis. For surface alloy, the surface formation energy is used to study the stability, which is calculated by the following formula,

$$E = \frac{1}{2A}\left(E_{slab} - nE_{A_{bulk}} - mE_{B_{bulk}}\right) \qquad (1.1)$$

the E_{slab}, $E_{A_{bulk}}$, and $E_{B_{bulk}}$ represent the total energy for the slab per unit cell, the bulk energy of material A, and the bulk energy of material B, respectively; the n and m denote the number of atoms of each species in the unit cell; and A is for the area of the surface unit cell. Except for the stability, the electronic and catalytic properties of noble bimetallic systems are of great interests.[28, 36, 38-41] Among various bimetallic metal alloys, Pt-based and Pd-based bimetallic systems are most widely investigated both experimentally and theoretically. Pd-based bimetallic metal alloys have been extensively studied for catalytic applications for hydrogenation reactions, oxidation and oxygen reduction reaction in fuel cells.[31, 35, 40, 42-44] Pt-based bimetallic metal alloys have been widely investigated in reactions such as electro-oxidation and fuel cell applications.[10, 45-51] The alloying component can be either other noble metals such as ruthenium and silver or non-precious metals such as copper and iron. For example, for PdAg/Pd surface alloy, Mancera *et al.* found that the CO adsorption is dominated by ensemble effect while the ligand effect and strain effect effectively cancel each other out.[52] This is also witnessed and confirmed by the experimental study.[53] For PdAu/Pd surface alloy, Zhang *et al.* have found that upon 100% Au surface concentration, the CO oxidation barrier is reduced to only 0.21eV compared with 0.87eV for pure Pd surface. Hence, a Pd(core)/Au(shell) structure is proposed for Au/Pd nanoparticles towards the CO oxidation application in the study.[32] For O_2 dissociation, Xu *et al.* have studied Pt-M bimetallic alloy.[47] The proposed structure

includes Pt monolayer and Pt-M substrate, which is the combination of non-precious metal (Fe or Co) and noble metal (Pt). This structure of thin Pt skins on top of Pt-Co or Pt-Fe alloy surface is more active towards ORR due to the enhanced resistivity to CO poisoning. For the hydrogenation, the critical step, dissociation of H_2 on metal surfaces, is widely studied. Recent experimental results found that when doped with Pd atoms, Cu(111) surface can effectively dissociate H_2 with a small energy barrier.[54] Theoretically, researchers found that the subsurface ensemble Pd atoms and the surface single Pd atom together act as the catalytic sites.[55]

The idea of active site is widely applied in heterogeneous catalysis. With the development of nanotechnology, noble metal nanoparticles have shown superior catalytic activity and selectivity. The unsaturated coordination environment results in higher activity than bulk materials. As the size is further reduced, the idea of single atom catalyst (SAC) is presented and has attracted increasing attention in recent years.[54, 56-62] Catalysts with well-designed single active site are expected to improve the performance for various chemical reactions. For example, the Pt_1/FeO_x single atom catalyst is 2 or 3 times more active than the corresponding Pt nanoparticles towards CO oxidation.[57] Superior performances of SACs in methane or alcohol oxidation reactions have also been reported recently.[59] The reason for the beneficial of size reduction can be explained in the following aspects: low-coordination environment of active centers, the quantum size effects and the metal support interactions.[39, 41, 63]

Although single atom catalysts can offer fascinating prospects, especially cost reduction and higher activity, the synthesis such as the robust stabilization of surface single metal atoms is full of challenge. The anchoring site is vital for SACs considering the stability during the chemical reactions. Usually, the single atom can be anchored on metal oxide, metal surface, and two-dimensional materials (such as graphene) as shown in Figure 1-2. Recently, the successfully prepared Pt single atom catalyst supported on iron oxide has triggered technological innovation and revolution for SACs.[57] The major issue for the preparation of SACs is Figure 1-2. The possible

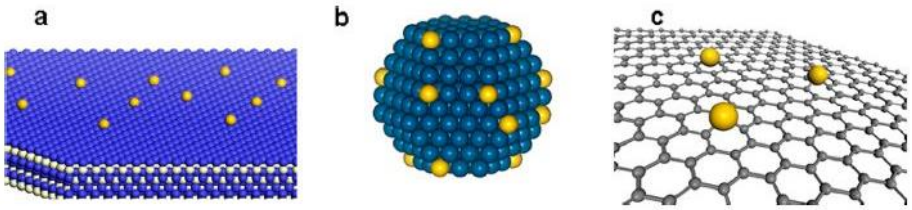

types of single atom anchored sites including (a) metal oxide, (b) metal surfaces, and (c) two-dimensional materials (graphene). (Reprinted with permission from Ref.[64])

to overcome the tendency of aggregation of single metal atoms. This is due to the increasing surface free energy when downsizing particle size. It is found that the surface vacancies or defects can serve as good anchoring sites for single metal atoms. For example, single Pt atom is located at the cationic vacancies on magnetite or γ-Al_2O_3.[65-66] Similarly, the single atoms are located on the defects involving carbon vacancies when supported on graphene.[67-68] Until now, the preparation of SACs with

isolated single atoms finely, densely and tightly anchored to the support is still under active investigation.

Theoretically, density functional theory modeling is applied to deal with the mechanism of high activity of SACs. For example, for Pt_1/FeO_x single atom catalyst, DFT calculations have confirmed the location of Pt atoms and the possible reaction pathway is proposed and shown in Figure 1-3.[57] Followed by the success of single Pt atom catalyst, Kwak *et al.* reported about the Pt single atom catalyst anchored on the γ-Al_2O_3.[69] The single gold atom catalyst supported on iron oxide is also reported, and the ultra-high stability is confirmed by theoretical studies.[58] Except for the explanation for existing experimental findings, Li *et al.* have provided new guidelines to design heterogeneous catalysts by DFT calculations.[70] They reported various single-atom catalysts supported on iron oxide (M_1/FeO_x) and studied the catalytic activity for CO oxidation. The results show that noble metal Rh, Pd, Ru and transition metal Ti, Co can exhibit overall or even better catalytic performance than Pt. Narula and co-workers, on the other hand, have proposed a new pathway for CO oxidation on Pt_1/θ-Al_2O_3 single atom catalyst.[71] They have pointed out that the single Pt atom prefers to bind O_2 rather than CO. The CO then binds to the oxygenated Pt atom and forms a carbonate. This new pathway is proposed for the appearance of CO_3 coverage.

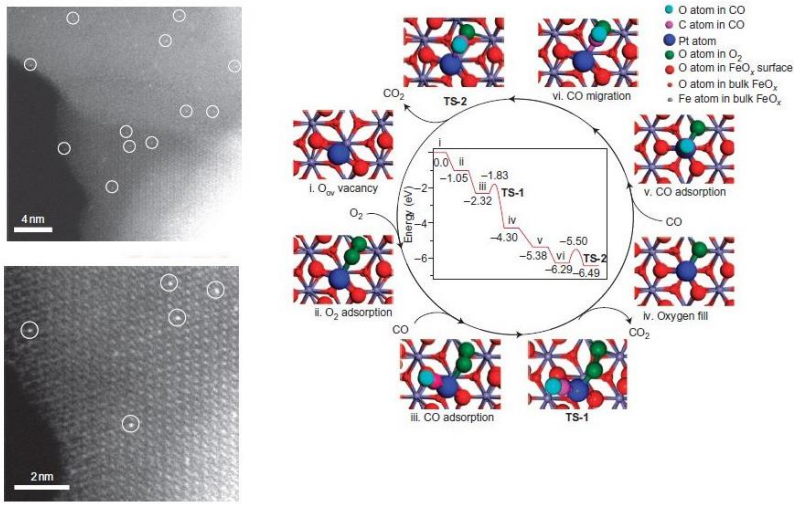

Figure 1-3. (left) Prepared Pt single atoms (white circles) are seen to be uniformly dispersed on the FeO_x support and occupy exactly the positions of the Fe atoms; (right) The proposed reaction pathways for CO oxidation on the Pt_1/FeO_x catalyst. (Reprinted with permission from Ref.[57])

Except for the widely investigated metal oxide support, metal and other support have also been studied by DFT calculations. The structure of single Pt atom dispersed on TiN substrate is very promising for fuel cells. The surface N vacancy sites is responsible for anchoring the Pt atom. This breakthrough provides a low-cost but high performance way for proton exchange membrane fuel cells (PEMFCs) applications.[72] For the hydrogenation, the noble metal doped in Cu(111) or Cu nanoparticles have been studied. Based on the cluster model, Cao *et al.* have considered single Pd atom doped on top, edge or inner site of Cu nanoparticles. The edge site doping with high stability can reduce the activation energy of H_2.[73] Fu and co-workers have studied the

transition metal atom (group VIIIB) doped in Cu(111) surface to investigate the hydrogenation performance.[74]

1.2 Objectives

Catalysis is widely used in our daily lives such as chemical manufacture and pharmaceutical engineering. Catalyst can increase the chemical reaction rate by decreasing the activation energy but without being consumed.[75] Generally, catalysis can be classified into two groups including heterogeneous catalysis and homogenous catalysis. Heterogeneous catalysis involves reactants, catalyst and products with several phases; while for homogeneous catalysis, catalyst, reactants and products have the same phase (such as acid catalysis).[76] Typical heterogeneous catalysis includes ammonia synthesis, hydrogenation and oxidation. Most heterogeneous catalysts are in solid phase and the reactants are usually in gas or liquid phase. The adsorption of reactants is the first step for catalysis reaction. Two types of adsorption are considered in heterogeneous catalysis, naming physisorption and chemisorption. After adsorbed on surface, the reaction mechanism is addressed due to the way of manipulating the catalyst surface for superior catalytic activity. Typical mechanisms include Rideal-Eley (RE) mechanism and Langmuir-Hinshelwood (LH) mechanism.[77] After reaction, the interaction between the products and surface affects the reaction rate. Once the product is desorbed from surface, the whole system is ready to perform the next catalytic cycle automatically.

With the development of nanotechnology, noble metals in nano-size or even smaller size have shown different catalytic ability compared with their bulk components. Noble metal nanoparticles such as Au, Pd and Ru are regarded as promising catalyst towards specific reactions. The pioneering work of Haruta *et al.*[78-79] on Au nanoparticles for CO oxidation has triggered the research on supported noble metal nanoparticles towards exceptional catalytic activity. The excellent catalytic activity and selectivity for low-coordination surface atoms have broadened the view of surface science. The design of metal surface is of great importance to enhance the use efficiency. Considering that noble metals are expensive and rare, it is vital to reduce the usage of noble metals while at least maintain the catalytic ability for a certain reaction. Based on this light, the idea of bimetallic alloy is proposed. Bimetallic catalysts are under research for years due to the enhanced catalytic activity and selectivity.[80-83] The chemical properties can be manipulated by the design of metal surfaces. For the structure of bimetallic alloy, core-shell nanoparticles[84] and near surface alloy[11] are two representative structures with high catalytic efficiency. The usage of noble metals is reduced in both structures. Early studies about adsorption on alloy surface have indicated that the lattice mismatch can induce strain on surface atoms.[85-88] This is a common method to manipulate the adsorption strength towards optimized range for better activity. Very recently, in order to improve the utilization of noble metals, the idea of single-atom alloy is proposed.[56, 64] One of the main

challenges is how to stabilize the single atom. Usually, single metal atom is anchored on metal oxides (such as CeO_2)[89], metal surfaces (such as Cu(111))[54], or two-dimensional materials (such as graphene)[90]. The surface defects, for example oxygen vacancy, can stabilize the single metal atom. However, the durability is one of the major concerns and the mechanism varies on different substrates.

Noble metals alloying with transition metals can result in enhanced stability and catalytic performance. The improvements are ascribed to effects including the ligand effect (electronic effect), strain effect (lattice mismatch) and ensemble effect.[91] These effects can modify the *d*-states of surface atoms. The famous *d*-band model is widely used to analyze and predict the catalytic activity in heterogeneous catalysis.[92-95] The adsorption strength shows linear relationship to the *d*-states of surface atoms (represented by *d*-band center ε_d). The stronger the adsorption strength, the upper shift the *d*-states (moving closer to the Fermi level). Based on famous Brønsted-Evans-Polanyi (BEP) relation, the adsorption strength is related to the energy barrier of the reaction.[96-97] All these parameters can be obtained or derived from DFT calculations. This can act as a guideline to predict catalytic ability and search for new catalyst.[98-100] Additionally, one can gain insight understanding for the reaction mechanism by performing DFT calculations.

Computational modeling is used to explore, explain and predict the properties of materials. The design of metal alloy and search for suitable catalyst cannot be done by

experiments one by one. With the help of simulation tool, we can estimate the catalytic activity, which can act as a reference or guideline for experiments. Additionally, theoretical analysis can be used to explain experimental results, which are difficult to be understood. This thesis focuses on computational study of catalytic activity for palladium (Pd) and platinum (Pt) alloying with non-precious metals. It is well known that Pd is commonly used as oxidation catalyst, while Pt is the perfect electrocatalyst for oxygen reduction reaction. When alloying with non-precious metals such as copper (Cu) and iron (Fe), the *d*-states of surface Pd and Pt atoms can be modulated. The reason behind this modulation and the corresponding design rule for certain reactions are studied in this thesis. In addition, the intermetallic alloy is discussed in detail with respect to the effect of Pd and host metal ratio on alloy structure. Moreover, the Pt single atom alloy model is studied in detail to expand the possible applications for hydrogenation.

1.3 Major Contribution of the Thesis

The major contributions are summarized as (1) the discovery of the scaling relations for predicting catalytic activity of CO oxidation catalyst, and (2) the computational study of the catalytic mechanism for CO oxidation, H_2 dissociation, and ORR. They are shown below:

I. Structure modeling of bimetallic alloy Pd-Cu and Pt-Cu

The proposed model of bimetallic alloy Pd-Cu (or Pt-Cu) is based on simple overlayer model with the idea of phase segregation. The effect of number of Pd (or Pt) cover layer is studied in detail with the combination of *d*-band model. It is found that the number of Pd (or Pt) cover layer can effectively influence the surface Pd (or Pt) activity. This is explained and supported by the *d*-band center theory, where the *d*-band center of Pd (or Pt) atom is modulated by both the number of cover layer and substrate Cu.

II. Catalytic activity of bimetallic alloy Pd-Cu and Pt-Cu

Prototypical reactions including CO oxidation and H_2 dissociation are used to investigate the catalytic activities of bimetallic alloy Pd-Cu and Pt-Cu, respectively. The energy barriers and scaling relations are verified. For Pd-Cu bimetallic alloy, the calculated barriers are found to show increasing trend with respect to *d*-band center for direct O_2 dissociation and decreasing trend with respect to *d*-band center for CO oxidation. The case of CO-assisted O_2 dissociation does not simply obey this rule. The proposed 2L-Pd/Cu(111) is found to benefit from low O_2 dissociation barrier and low CO oxidation barrier. Pt-Cu bimetal alloy is found to be effective for fuel cell anode catalyst. We have focused on 2L-Pt/Cu(111) due to good stability. The CO-tolerance ability is estimated by calculating the CO saturation coverage. 2L-Pt/Cu(111) has much lower CO saturation coverage (40%) compared with that of Pt(111) (75%).

III. Structure modeling of Pd monolayer structure Pd/Pd-M (M=Cu, Fe or Ni)

The proposed model of Pd monolayer structure is based on experimental results with the concept of phase transformation consisting of monolayer Pd surface and Pd-M intermetallic core. Due to phase transformation, the substrate has either *bcc* (PdCu) or *fct* (PdNi, PdFe) structure. The ratio of Pd and M is 50:50 for these ordered intermetallic alloy. The dissolution potential analysis indicates that Pd/PdCu(110), Pd/PdNi(111) and Pd/PdFe(111) are stable in operating conditions.

IV. Catalytic activity of Pd monolayer structure Pd/Pd-M (M=Cu, Fe or Ni)

The oxygen reduction reaction is used to verify the catalytic activity of Pd monolayer structure Pd/Pd-M (M=Cu, Fe or Ni). The scaling relations and free energy diagram are discussed in detail. O_2 is found to undergo hydrogenation process into OOH species instead of direct dissociation on Pd/PdM(111) surfaces while it shows different trend on Pd/PdCu(110) surface, which prefers direct dissociation mechanism. The enhanced activity for Pd monolayer structures is ascribed to moderate adsorption strength for ORR intermediates due to compression strain and substrate electron transfer.

V. Structure modeling of single-atom alloy Pt/Cu(111)

The proposed model of single-atom alloy is studied with both slab model and icosahedral nanocluster model. The aggregation effect (formation of Pt dimmer or Pt trimmer) is studied in detail for both structures. It is found that single Pt atom prefers surface (slab model) or outmost shell (nanocluster) sites instead of subsurface or core

sites. When adding Pt atoms one by one, the additional Pt atoms tends to occupy surface sites to form isolated structure or outmost shell sites to form adjunctive structure.

VI. Catalytic activity of single-atom alloy Pt/Cu(111)

The hydrogenation reaction is used to test the catalytic activity of Pt/Cu(111). H_2 dissociation with respect to H_2 surface coverage and Pt dopant concentration and sites are studied. The possibility of multi-catalytic sites are also checked. For both slab model and nanocluster model, it is noted that the most stable configurations do not always correspond to the most effective structure for H_2 dissociation. Additionally, with the help of subsurface Pt substitution (slab model) or inner Pt substitution (nanocluster), the ability for dissociation of H_2 is improved and surface isolated Pt atoms can serve as multi-active sites for H_2 dissociation.

1.4 Organization of the Thesis

This thesis includes eight chapters. In Chapter 1, the motivation and objectives of this thesis are discussed. The major contribution is summarized as well. Chapter 2 explains the theoretical background based on first principle quantum calculations. Chapter 3 summarizes the fundamental theory in heterogeneous catalysis such as Volcano curve and *d*-band center model. Chapter 4 to Chapter 7 summarize the results of calculations and discussions. Chapter 4 presents the results of bimetallic overlayer structure of Pd-Cu and the application for CO oxidation. Chapter 5 describes the

results of bimetallic overlayer structure of Pt-Cu and the application for fuel cell catalyst. Chapter 6 summarizes the results of intermetallic alloy Pd-M (M=Cu, Fe, or Ni) and the application for oxygen reduction reaction catalyst. Chapter 7 summarizes the results of single-atom alloy Pt/Cu(111) and the application for hydrogenation. Chapter 8 includes conclusions and some recommendations for future works.

Chapter 2 Theoretical Framework

In Chapter two, we will describe the theoretical framework of first principle density functional theory calculations which are employed in this thesis.

2.1 Schrödinger Equation

The Schrödinger equation is a well-known mathematical equation used in quantum mechanics that describes the changes over time of a physical system.[101] One representative form is the time-independent formula shown below:

$$H\Psi = E\Psi \qquad (2.1)$$

where H, Ψ and E represents the Hamiltonian operator (containing two factors: potential energy V and kinetic energy T), wave function, and the total energy, respectively.[102] For a single particle, the time-independent Schrödinger equation is given below, where m is the mass and $\hbar$ is the reduced Planck's constant

$$[\frac{-\hbar^2}{2m}\nabla^2 + V(r)]\,\Psi(r) = E\Psi(r) \qquad (2.2)$$

However, for the many-body system, it generally consists of multiple electrons and multiple nuclei. In order to solve the Schrödinger equation, we need a more detailed description of interactions. It is known that in terms of mass, the nuclei are much heavier than electrons. The Born-Oppenheimer (BO) approximation can be applied to separate the motion of electrons and atomic nuclei.[103] We can first solve the equation about electron motion by considering atomic nuclei with fixed position. And then the ground state for electrons moving in the field of nuclei is obtained. This approximation

can downgrade the degree-of-freedom and we can rewrite the Hamiltonian operator as follows for many-body system:

$$H = \frac{\hbar^2}{2m}\sum_{i=1}^{N}\nabla_i^2 + \sum_{i=1}^{N}V(r_i) + \sum_{i=1}^{N}\sum_{j<i}U(r_i, r_j) \qquad (2.3)$$

where m and $\hbar$ represents electron mass and reduced Planck's constant, respectively. Three parts are considered for the Hamiltonian operators including the electron kinetic energy (first part), the interaction energies which are corresponding to electron and atomic nuclei (second part, V is the potential operator) and various electrons (third part, U is the potential operator).

2.2 Hartree-Fock Theory

The many-body problem described by the Schrödinger equation can be solved by Hartree-Fock (HF) theory. The Hartree-Fock approximation is an extension to the previous Hartree equation based on the independent particle model.[104] HF theory is a mean-field method that assumes the electron moves independently in a mean potential field created by the rest electrons.[105] In this way, the energy of a quantum many-body system and ground-state wave function can be approximately solved by numerical techniques. HF theory complies with two classical principles including anti-symmetry principle and Pauli exclusion principle. The anti-symmetry principle demonstrates that when two arguments are swapped, the wavefunction changes sign.

$$\Psi(\xi_1, \xi_2, \ldots, \xi_N) = -\Psi(\xi_N, \ldots, \xi_2, \xi_1) \qquad (2.4)$$

The Pauli exclusion principle states that the same quantum state cannot be occupied by more than two identical fermions (including two) simultaneously. For the N-electron wave function discussed here, we can do a further approximation with Slater determinant.[106] For N-electron system, the Slater determinant can be viewed as follows:

$$\Psi(r_1, r_2, \dots, r_N) = \frac{1}{\sqrt{N!}} \begin{bmatrix} \varphi_1(r_1) & \cdots & \varphi_1(r_N) \\ \vdots & \ddots & \vdots \\ \varphi_N(r_1) & \cdots & \varphi_N(r_N) \end{bmatrix} \quad (2.5)$$

where $\varphi_i(r_j)$ is the one-electron spin orbital which is orthonormal and $\frac{1}{\sqrt{N!}}$ acts as the normalization factor.

Hartree-Fock (HF) calculation can be used to get the many-body system energy in relation to all wave functions. The HF equation can be written as follows:

$$\left[-\frac{1}{2}\nabla_i^2 + \sum_I V(R_I - r_i)\right]\varphi_\lambda(r_i) + \left[\sum_\mu \int \varphi_\mu^*(r_j)\frac{1}{|r_j - r_i|}\varphi_\mu(r_j)dr_j\right]\varphi_\lambda(r_i)$$

$$- \sum_\mu \delta_{\sigma_i \sigma_j}\left[\int \varphi_\mu^*(r_j)\frac{1}{|r_j - r_i|}\varphi_\lambda(r_j)dr_j\right]\varphi_\mu(r_i) = \varepsilon\varphi_\lambda(r_i) \quad (2.6)$$

It is noted that the HF equation requires self-consistent method to solve. The electron density can be defined based on an initial estimation of the spin orbital. The derived electron density is then used to solve the single-electron equations for the spin orbital, where the solved spin orbital must be consistent with the initial spin orbital under certain convergence. In this way, the HF theory can be applied in theoretical calculations to deal with the atoms and molecules. However, the HF theory has

limitations. The main challenge is that the HF theory assumes the electron correlations in an average way. Thus, there is a non-negligible deviations between the calculated solutions and actual experimental results. Today, first principle density functional theory acts as an optional way to HF calculations applied to solve the many-body problems.[107]

2.3 Density Functional Theory

2.3.1 Hohenberg-Kohn Theorem

Two fundamental theorems constitute the Hohenberg-Kohn theorem, which was proposed in 1964.[108-109] The first theorem proves that there exists a function of electron density which can be used to solve the Schrödinger equation; the second theorem provides an explanation about what the function is. Hohenberg-Kohn theorem points out that for a quantum mechanical system, the electron density can uniquely determine the corresponding energy. At position r, the electron density and ground state energy are described as $n(r)$ and $E[n(r)]$.

$$E[n(r)] = \int n(r)V_{ext}(r)dr + F[n(r)] \qquad (2.7)$$

However, the Hohenberg-Kohn theorem has its own limitations. The method of finding $E[n(r)]$ is not covered. This problem is solved by Kohn-Sham theory.

2.3.2 Kohn-Sham Theory

The Kohn-Sham theory acts as new method to handle the Schrödinger equation by considering a reference system that is non-interacting and has the identical ground

state density with given interacting system.[110] In this way, the Schrödinger equation is simplified to a single-particle system. The energy function is shown below:

$$E[n(r)] = T_s[n(r)] + \frac{1}{2}\iint \frac{n(r)n(r')}{|r-r'|}drdr' + E_{xc}[n(r)] + \int n(r)V_{ext}(r)dr \quad (2.8)$$

$$T_s[n(r)] = -\frac{\hbar}{2m}\sum_i \phi_i^*(r)\nabla_i^2\,\phi_i(r) \quad (2.9)$$

where T_s stands for the non-interacting electron kinetic energy, the middle integrating term represents the self-interaction, and $E_{xc}[n(r)]$ and $V_{ext}(r)$ are exchange-correlation energy and external potential, respectively. And the single-particle Schrödinger equation is shown below:

$$\int n(r)dr = N \quad (2.10)$$

$$n(r) = \sum_i |\phi_i(r)|^2 \quad (2.11)$$

$$\left[-\frac{1}{2}\nabla^2 + (V_{ext}(r) + \int \frac{n(r')}{|r-r'|}dr' + V_{xc}(r))\right]\Psi = E\Psi \quad (2.12)$$

The $V_{xc}(r)$ is related to the exchange-correlation energy E_{xc} and calculated as below:

$$\frac{\delta E_{xc}[n(r)]}{\delta n(r)} = V_{xc}(r) \quad (2.13)$$

We can rewrite equation 2.11 to the following equation:

$$\left[-\frac{1}{2}\nabla^2 + V_{eff}(r)\right]\Psi = E\Psi \quad (2.14)$$

$$V_{eff}(r) = V_{ext}(r) + \int \frac{n(r')}{|r-r'|}dr' + V_{xc}(r) \quad (2.15)$$

By solving the single-particle equation, the ground state energy are given by

$$E_{KS}(n) = \sum_{i}^{N} \varepsilon_i - \frac{1}{2} \int d^3r d^3r' \frac{n_{(r)} n_{(r')}}{|r - r'|} + E_{xc}[n(r)] - \int d^3r \, V_{xc}(r) n(r) \qquad (2.16)$$

Finally, $E_{xc}[n]$ will be covered to solve the Kohn-Sham equation.

2.3.3 Exchange-Correlation Functional

$E_{xc}[n]$ has been developed to deal with the Kohn-Sham equation. Generally, three commonly used functional are performed in DFT calculations, which include the local density approximation (LDA), the generalized gradient approximation (GGA), and the hybrid functionals. For LDA and GGA, the general form can be written as below:

$$E_{xc}[n] = \int \varepsilon_{xc}[n(r)] \, n(r) dr \quad (2.17)$$

where n(r) is the number of electrons per unit volume and $\varepsilon_{xc}[n(r)]$ represents the exchange-correlation energy per electron.

The local density approximation was first proposed by Kohn and Sham. Homogeneous electron gas model is applied to obtain the corresponding $E_{xc}[n]$.[111-112]

$$E_{xc}^{LDA}[n(r)] = \int \varepsilon_{xc}[n(r)] n(r) dr \quad (2.18)$$

$$E_{xc}^{LDA}[n] = E_x^{LDA}[n] + E_c^{LDA}[n] \qquad (2.19)$$

$$E_x^{LDA}[n] = C \int n^{\frac{4}{3}}(r) dr \qquad (2.20)$$

where C is the constant ($C = -\frac{3}{4}(\frac{3}{\pi})^{1/3}$). The correlation part $E_c^{LDA}[n]$ can be obtained by fitting to the results of accurate Quantum Monte Carlo (QMC) calculations.[113] This

approximation is simple but with good accuracy. Thus, it can be applied in solid-state physics and provide reasonable results for metallic and semiconducting materials. However, the LDA usually underestimate the atomic ground state energy and ionization energy. LDA also cannot accurately describe highly localized *d*-sates of transition metals and the binding energy.

An improvement has been made for generalized gradient approximation method. Considering that electron density is not uniform for a real system, its gradient ∇n(r) is taken into account.[114-116] A modification to LDA energy density is thus made. The E_{xc}^{GGA} can be viewed as

$$E_{xc}^{GGA}[n(r)] = \int n(r)\varepsilon_{xc}[n(r)]F_{xc}[n(r), \nabla n(r)]dr \qquad (2.21)$$

$$E_{xc}^{GGA}[n] = \int n(r)\varepsilon_{xc}(n(r), |\nabla n(r)|)dr \qquad (2.22)$$

$$\varepsilon_{xc}^{GGA}[n] = \varepsilon_{xc}^{LDA}[n] + \Delta\varepsilon_{xc}\left[\frac{|\nabla n(r)|}{n^{\frac{4}{3}}(r)}\right] \qquad (2.23)$$

where $\Delta\varepsilon_{xc}$ is the correction term added to the LDA function. Generally, GGA can provide better results for chemical accuracy than LDA such as bond dissociation energy and transition-state barrier. There are several forms for gradient approximations implemented in VASP such as Perdew-Wang (PW91)[117] and Perdew-Burke-Ernzerhof (PBE)[118]. In this thesis, GGA in form of PBE is applied for most of the calculations.

Hybrid functionals can be seen as a group of exchange-correlation energy functional approximations involving part of Hartree-Fock (HF) exchange energy. And the resulting new exchange term is a summary of local or semi-local DFT exchange energy (LDA, GGA) and HF exchange energy. The general hybrid functional can be written as follows:

$$E_{xc} = \alpha E_x^{HF} + (1-\alpha)E_{xc}^{DFT} \qquad (2.24)$$

where α is a percentage content for the HF exchange energy. Typically, two most commonly used hybrid functionals are the three-parameter B3LYP functional[119] and Heyd-Suseria-Ernzerhof (HSE) functional[120-121]. The B3LYP functional can be viewed as:

$$E_{xc}^{B3LYP} = E_{xc}^{LDA} + a(E_x^{HF} - E_x^{LDA}) + b(E_x^{GGA} - E_x^{LDA}) + c(E_c^{GGA} - E_c^{LDA}) \qquad (2.25)$$

where a, b, and c are empirical parameters. The HSE functional can be viewed as:

$$E_{xc}^{\omega PBEh} = aE_x^{HF,SR}(\omega) + (1-a)E_x^{PBE,SR}(\omega) + E_x^{PBE,LR}(\omega) + E_c^{PBE} \qquad (2.26)$$

where a=1/4 and ω = 0.2 for HSE06, SR represents short range and LR is for long range.

2.3.4 Bloch's Theorem

For periodic material systems, the atomic nuclei are arranged in a periodic array. The Bloch's theorem is applied to deal with the effectively infinite number of

electrons within periodic material. This theorem means that it is only necessary to consider the number of electrons within the unit cell. The potential of a periodic material system can be written as

$$V^{SP}(r+R) = V^{SP}(r) \qquad (2.27)$$

and the single-particle wavefunctions can be expressed as follows:

$$\varphi_k(r+R) = e^{ikR}\varphi_k(r) \qquad (2.28)$$

2.3.5 Project Augmented Wave (PAW) Method

In 1994, Peter Blöchl developed the PAW method.[122] In general, PAW method combines the linear augmented-plane-wave method and pseudopotential method.[123] The electronic structures can be accurately described by PAW method within the framework of DFT. A linear transformation operator *T* is used to transform the auxiliary smooth wave function to all electron Kohn-Sham (KS) single particle wave function:

$$|\Psi_n\rangle = T\big|\widetilde{\Psi}_n\rangle \qquad (2.29)$$

The relationship between the Blöchl wave function and the smooth auxiliary wave function is shown below;

$$\Psi_{nk}(r) = \widetilde{\Psi}_{nk}(r) + \sum_{a,i}\big[\phi_i^a(r) - \tilde{\phi}_i^a(r)\big]\langle\tilde{p}_i^a|\widetilde{\Psi}_{nk}\rangle \qquad (2.30)$$

where three components are taken into consideration: the partial waves $\phi_i^a(r)$, the smooth partial waves $\tilde{\phi}_i^a(r)$, and the smooth projector functions $\tilde{p}_i^a$. In this thesis, the project augmented wave (PAW) method is used.

2.4 Computational Codes

In this research, Vienna ab initio simulation package (VASP) code is applied to carry out the theoretical calculations by the implementation of first principle density functional theory. VASP is a package for performing ab-initio quantum-mechanical molecular dynamics based on density functional theory using pseudopotentials and a plain wave basis set. Both LDA and GGA potentials/functions are available. When performing the calculations, structure relaxing and convergence are two key parts before obtaining any useful results. For structure relaxing, the forces between the atoms are minimized. It is noted that a relaxed structure can be different from an experimental structure due to the description of potentials in POTCAR file. For convergence, it means to optimize parameters such as cutoff energy and number of k-point to be sampled over the Brillouin zone.

In this thesis, all the calculations are performed based on supercomputing cluster of the high-performance computing center (HPCC) in Nanyang Technological University.

2.5 Summary

In this work, DFT calculations have been performed to do all the calculations as implemented in VASP. In the past decades, DFT with LDA and/or GGA has obtained acceptable accuracy for classes of materials and is widely applied in computational

material science. However, it should be noted that DFT calculations cannot provide exact solutions to the full Schrödinger equation.

Chapter 3 Fundamental Theory in Heterogeneous Catalysis

In Chapter three, we will present the fundamental theory in heterogeneous catalysis such as *d*-band center theory and Brønsted-Evans-Polanyi relation. These fundamental theories are performed as guidelines to analyze the catalytic activity and large-scale screen search for possible catalyst.

3.1 *d*-band Center Theory

Transition metals, especially precious metals, are widely used in heterogeneous catalysis. The understanding of surface chemistry or catalytic reaction is necessary to design catalyst and improve the catalytic efficiency. DFT calculations are successfully applied in surface science such as surface adsorption and reaction.[98, 124-125] It is essential to develop a model or method to figure out and predict the catalytic activity from one transition metal to another. The *d*-band model proposed by Nøskov and Hammer[92, 95, 126] is a great breakthrough in theoretical surface science and catalysis. This model is quite powerful in understanding the bond formation and predicting the origin of catalytic trend for transition metals.

When adsorbate chemisorbed on metal surface, the adsorption process can be analyzed by plotting the density of states (DOS) of adsorbate and metal surface atoms. For example, the change in local electronic structure at an oxygen atom upon adsorption on noble metal Pt surface is shown in Figure 3-1.[94]

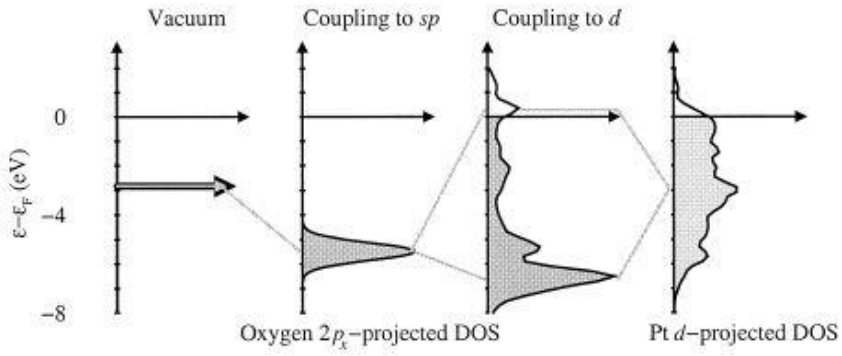

Figure 3-1. The illusion of the change in local electronic structure at an oxygen atom upon adsorption on Pt surface. (Reprinted with permission from Ref.[94])

We can view the adsorption interaction (bond formation) in two steps. First, the coupling between the adsorbate valance 2*p* state and metal *s* electrons is considered. As a consequence, the sharp atomic states of oxygen atom are broadened into resonances and shifted downward. Second, the effect of coupling with *d* electrons are taken into account. As a result, the oxygen resonance is found to be splitting into two states: covalent bonding and anti-bonding states. Coupling to *s* electrons gives rise to a shift and broadening of the adsorbate states; Coupling to *d* electrons leads to the formation of anti-bonding states and bonding states.[98] Thus the description of metal surface *d*-states is quite useful to predict the reactivity of transition metals considering that the adsorption strength is related to the filling of anti-bonding states.

The *d*-band center (ε_d) represents the energy average of the *d* electrons and can serve as a descriptor to analyze the surface adsorption and reaction.[11, 99, 127] The adsorption strength becomes stronger with upper shift of the *d*-band center (moving closer to the Fermi level). The *d*-band center (ε_d) of selected transition metals in periodic table are shown in Figure 3-2.[94] Based on the *d*-band center theory, two general trends can be concluded. One is that from left to right, the bond becomes stronger; the other one states that the farther down the periodic table, the weaker the interaction.

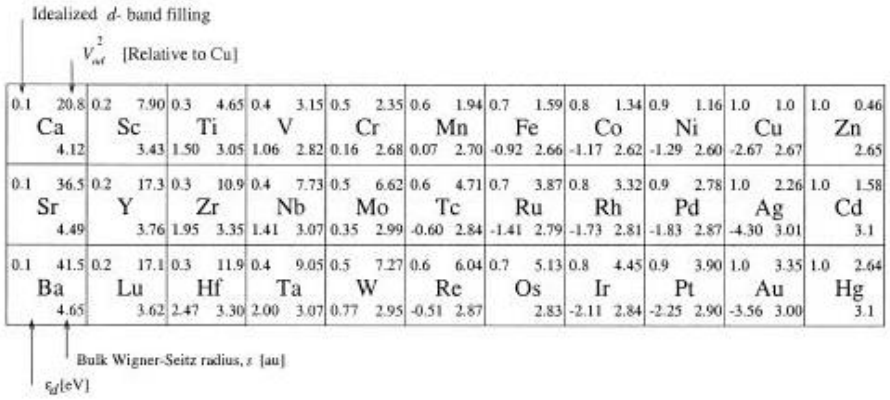

Figure 3-2. The *d*-band center (ε_d) of selected transition metals in periodic table. (Reprinted with permission from Ref.[94])

3.2 Brønsted-Evans-Polanyi Relation

The Brønsted-Evans-Polanyi (BEP) relations[128-129] is widely used in physical chemistry and demonstrates that the activation energy (E_a) is linearly related to the

enthalpy of reaction (*ΔH*) for the reactions belong to the same family.[96-97, 130] The BEP relation can be mathematically viewed as:

$$E_a = E_0 + \alpha \Delta \mathrm{H} \qquad (3.1)$$

where ΔH represents the enthalpy change of each reaction, and E_0 and α are constants. From the results of DFT calculations, we can derive different forms of BEP relations. These derived BEP relations are widely applied to analyze the surface catalytic ability and search for efficient catalyst in heterogeneous catalysis.[131-133] The activation energy can be obtained experimentally by the Arrhenius equation:

$$k = Ae^{-\frac{E_a}{RT}} \qquad (3.2)$$

where k and R represent rate constant and gas constant, respectively and A stands for the pre-exponential factor. After a simple logarithm derivation, the activation energy can be obtained by the equation shown below:

$$E_a = \frac{Rln\frac{k_2}{k_1}}{\frac{1}{T_1} - \frac{1}{T_2}} \qquad (3.3)$$

An interesting conclusion can be drawn from BEP relation is that the interaction between the catalyst surface and adsorbate should be intermediate. This is known as volcano curve, which is derived from the Sabatier principle.[134] Too weak interaction can result in difficult of activation (rate-limiting step); while too strong interaction can hinder the desorption and block the catalytic site. This curve is widely used in heterogeneous catalysis as a descriptor for catalyst design through large-scale

screening approach. Additionally, nowadays the scaling relation is playing an important role in theoretical calculations.[135] The scaling relation can be used to figure out the catalytic trend by relating the adsorption energies of various intermediates across a variety of catalyst surfaces. An example of scaling relation is shown in Figure 3-3.[136]

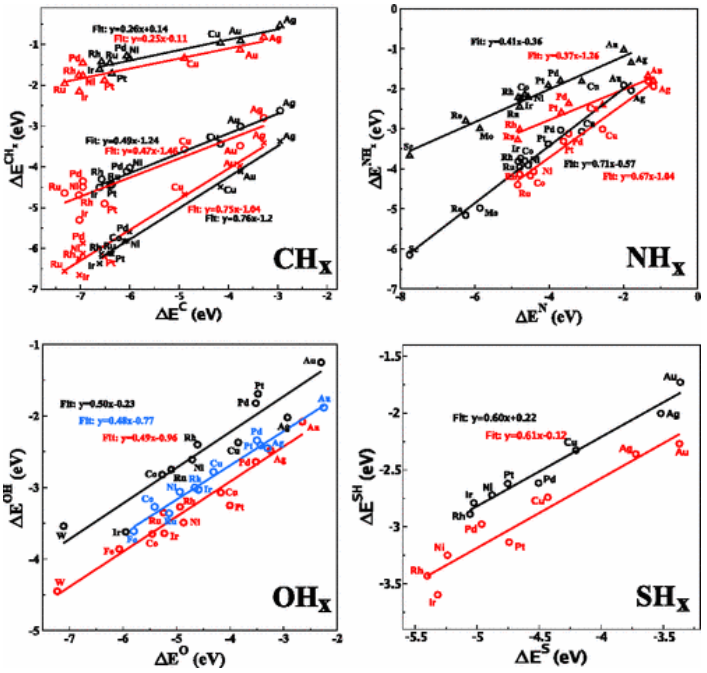

Figure 3-3. Example of scaling relations on *fcc* transition metals. (Reprinted with permission from Ref.[136])

3.3 Kinetics of Catalytic Reactions

Heterogeneous catalysis is widely applied and researched for years, where chemical reactions play a vital role. Since the involved chemical reactions usually take place on the surface, it is essential to understand the kinetics of catalytic reactions.

Catalyst can participate in chemical reactions in way of reducing activation energy and increasing the reaction rate. We can use a gas-phase reaction catalyzed on solid surface as an example to illustrate the kinetics of heterogeneous catalysis.

Firstly, we will consider unimolecular reaction and the reaction can be viewed as follows:

$$A(g) + C(s) \leftrightarrow AC(s) \qquad (3.4)$$

$$AC(s) \rightarrow P(g) + C(s) \qquad (3.5)$$

where two steps are involved. Step one is transforming the gas-phase molecular A to transition state AC; and step two is to obtain product P. C represents the catalyst and is not changed or consumed. Step one is reversible with adsorption rate k_1 and desorption rate k_{-1}. Step two has a reaction rate with k_2. The surface coverage of A (represented by θ) can be derived under steady state approximation:

$$\frac{d[AS]}{dt} = k_1[A](1-\theta)[S]_0 - k_{-1}\theta[S]_0 - k_2\theta[S]_0 = 0 \qquad (3.6)$$

$$\theta = \frac{k_1[A]}{k_1[A] + k_{-1} + k_2} \qquad (3.7)$$

where $[S]_0$ is the concentration of total active sites. Thus, the rate of production P can be written as follows:

$$\frac{d[p]}{dt} = \frac{k_1 k_2}{k_1[A] + k_{-1} + k_2}[A]\Theta[S]_0 \quad (3.8)$$

Secondly, we will consider the bimolecular gas-phase reactions on surface. Generally, the Langmuir-Hinshelwood (LH) mechanism[137-138] and Eley-Rideal (ER) mechanism[139] are widely used in heterogeneous catalysis. For LH mechanism, the gas-phase reactants are both adsorbed on catalyst surfaces; while for ER mechanism, only one reactant is adsorbed on catalyst surface. The LH reaction mechanism can be viewed as follows:

$$A(g) + C(s) \leftrightarrow AC(s) \quad (3.9)$$

$$B(g) + C(s) \leftrightarrow BC(s) \quad (3.10)$$

$$AC(s) + BC(s) \rightarrow P \quad (3.11)$$

Three steps are considered for LH reaction. Step one (or two) is transforming the gas-phase molecular A (or B) to transition state AC (or BC); step three is to obtain product P. Step one (or two) is reversible with adsorption rate k_1 (or k_2) and the desorption rate k_{-1} (or k_{-2}). Step three has a reaction rate with k. Similarly, we can derive the surface coverage of A (represented by θ_A):

$$\theta_A = \frac{k_1 C_A \theta_E}{k_{-1} + kC_S\theta_B} \quad (3.12)$$

where $\theta_A + \theta_B + \theta_E = 1$, $\theta_E$is for the concentration of empty site. The ER reaction mechanism can be viewed as follows:

$$A(g) + C(s) \leftrightarrow AC(s) \qquad (3.13)$$

$$B(g) + AC(s) \rightarrow P + C(s) \qquad (3.14)$$

where step one is reversible with adsorption rate k_1 and desorption rate k_{-1}. Step two has a reaction rate with k_2. The surface coverage of A (represented by θ_A) can be derived under steady state approximation:

$$\frac{d[AS]}{dt} = k_1[A](1-\theta)[S]_0 - k_{-1}\theta[S]_0 - k_2\theta[S]_0[B] = 0 \qquad (3.15)$$

$$\theta_A = \frac{k_1[A]}{k_1[A] + k_{-1} + k_2[B]} \qquad (3.16)$$

Both equation 3.12 and equation 3.16 can be developed under rate limiting step given. This can be applied in different reactions and is not discussed here.

3.4 Modeling of Bimetallic Alloy

Bimetallic alloy is widely applied in heterogeneous catalysis due to improved catalytic activity and selectivity compared with pure metals.[140-142] Based on the *d*-band center theory, it is interesting and important to understand the source governing chemical activity. For bimetallic alloy, the enhanced activity is mainly attributed to effects including ligand effect, ensemble effect and geometric effect.[91] The ligand

effect is related to electronic interaction between the two components and thus modify the catalytic activity and selectivity. The ensemble effect is about a certain number of active sites required for some reactions. The selectivity can be ensured by blocking the ensemble of active sites. The geometric effect is about the modification of the inter-atomic distances when forming bimetallic alloy. First principle density functional theory calculations can be applied to study the bimetallic alloy and corresponding mechanism, which is essential to design novel catalysts.

Bimetallic overlayer structure is usually used to simulate the bimetallic alloy. The overlayer structure consists of two parts: the substrate and the pseudomorphic surface layer. The pseudomorphic layer has the same lattice spacing as the substrate. It is expected that overlayer experiences strain due to lattice mismatch. This strain can induce changes in the adsorption energies and reaction barriers. In this thesis, we have adopted this bimetallic overalyer structure to study the Pd-Cu and Pt-Cu bimetallic alloy systems. The detailed calculation and discussion are summarized in Chapter 4 and Chapter 5. Recently, another representative bimetallic alloy structure, the intermetallic alloy, has drawn much attention due to enhanced stability and activity.[143-146] The major challenge for the synthesis of intermetallic alloy is how to transform the disordered solid dilution phase to the ordered intermetallic phase. The ordered intermetallic structure is reported to possess high chemical and structural stability and allow precise predictions on the composition of the near-surface region and

distribution of the active sites.[143] In this thesis, we have performed DFT calculations to investigate on the Pd based intermetallic alloy including PdCu, PdFe and PdNi with Pd monolayer structure. The detailed calculation and discussion can be found in Chapter 6.

3.5 Summary

These fundamental theories are widely used nowadays and can even be developed by modern computational calculations to broaden the view of surface science. Computational surface science in combination with fundamental theories will continue play an important role in heterogeneous catalysis, especially in large-scale screen searching for catalyst.

Chapter 4 DFT Study on Layer Effect on Catalytic Activity of Pd-Cu Bimetal Alloy for CO Oxidation

In this chapter, we will present our work on Pd-Cu bimetal alloy towards CO oxidation. The overlayer model is adopted to simulate the Pd-Cu bimetal alloy. We have first addressed on the effect of number of Pd overlayer on the catalytic performance. And then the origin of the catalytic trend is discussed.

4.1 Overview

Heterogeneous catalysis with the design of surface is an important way to enhance the use efficiency of fossil fuel and energy conversion with an environment-friendly way.[147-149] In the research of heterogeneous catalyst, the manipulation of the chemical properties of catalysts has attracted great interest.[52, 150-151] Bimetallic catalysts due to their superior catalytic activities and selectivity have been used in different reactions, such as catalytic reforming[152] and alcohol oxidation.[153] CO oxidation is a prototypical reaction in heterogeneous catalysis and is usually used to test the catalytic activity of a designed oxidation catalyst.[154] CO oxidation can be applied in clean technology for purification of the effluent streams particularly in car exhausts or reformate streams.[4, 155-156] Additionally, continuous supply of CO-free hydrogen under the operation condition is a critical challenge for proton exchange membrane fuel cells.[157] Among the novel metals, palladium (Pd) is considered as a quite efficient catalyst for CO oxidation.[158-160] Based on the fact that alloying with a second metal can enhance the

catalytic performance of noble metals by tailoring the electronic structures, we have considered the Pd-Cu bimetallic alloy as the catalyst for CO oxidation in this work. The bimetallic nanoparticles with controlled size and composition open enormous possibility to enhance the catalytic activity and selectivity. Experimental evidence has proved that Pd-M alloys (M represents transition metals) undergo phase segregations and the noble metal Pd tends to form a pure Pd overlayer on the bulk alloys.[44, 161] For example, in the bimetallic nanoparticle of Pd alloy with other metal, such as Ni, Fe, and Cu, it is expected to form the Pd shell as an effective catalyst. Theoretically, the pseudomorphic layer model is usually adopted to simulate the binary alloy surfaces.[162-163] In this work, in order to analyze the effect of layers, we have considered the thin overlayer or shell (1-3 atomic layers) of Pd on the cheap metal Cu bulk or core layer with the slab model.

4.2 Computational Methods

4.2.1 Pd-Cu Bimetallic Overlayer Structure

The pseudomorphic layer model was used to illustrate the Pd-Cu bimetallic alloy by a thin overlayer of Pd on Cu(111). The vacuum region was up to 15Å and a 2×2 supercell was used in this slab method. For the thickness of overlayer, three models including single-layer Pd, double-layer Pd, and triple-layer Pd, were considered to be covered above the Cu substrate (three layers). We have used NL-Pd/Cu(111) to represent the models studied here, where N is the number of Pd overlayer. In order to

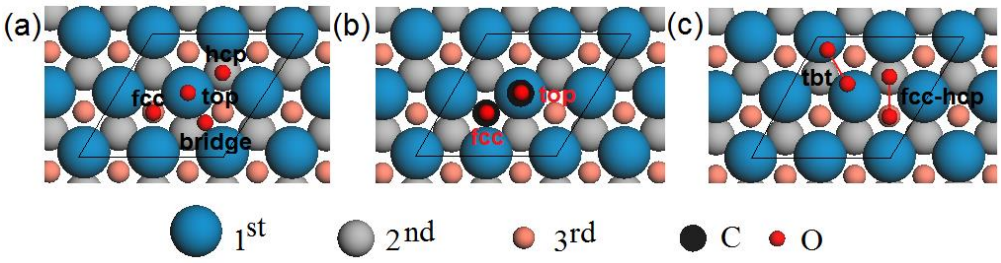

Figure 4-1. The configuration of top view of NL-Pd/Cu(111) with 2×2 supercell model, where N represents the number of Pd overlayer, ranging from (a) one layer, (b) two-layer and (c) three-layer. The atomic oxygen adsorption site, CO adsorption site and O_2 adsorption site are shown in Fig. 4-1a, 4-1b and 4-1c, respectively. The blue atom represents the first atomic layer for surface; the grey atom represents the second atomic layer; the orange atom represents in the third atomic layer. The carbon atom and oxygen atom are shown in black and red color, respectively.

verify the results that are uncorrelated with the thickness of Cu substrate and three-layer Cu as the substrate is enough and accurate, we have built the model of 7-layer Cu(111) slab and replaced the surface Cu by Pd atoms layer by layer which is denoted as 7-layer Pd_N/Cu(111), where N is the number of Pd overlayer. It is noted that Pd overlayer on top of Cu(111) has experienced compression strain due to lattice mismatch. A compressed five-layer Pd(111) was built and calculated to study the compression effect. The top view of NL-Pd/Cu(111) bimetallic system and the possible adsorption sites of atomic O, O_2 and CO are schematically illustrated in

Figure 4-1. The *k*-point mesh[164] of 5×5×1 and 6×6×1 were for NL-Pd/Cu(111) and Pd_N/Cu(111), respectively. The bottom two layers were fixed with the value of bulk Cu in the structural relaxation.

4.2.2 DFT Calculations

All the calculations were performed on the basis of spin-polarized DFT with projector augmented wave formalism, as implemented in the VASP code.[123, 165] The generalized gradient approximation with the parametrization of Predew-Burke-Ernzerhof was used for the exchange-correlation functional.[118, 166] A kinetic energy cutoff of 400eV for the plane wave expansion with proper k-point spacing using Monkhorst-Pack grid method[164] was found to be sufficient to ensure that the total energy was converged at 1meV/atom level. The convergence criterion for the self-consistence field energy was set to be 10^{-4}eV.

4.3 Discussions

4.3.1 Geometry of Pd-Cu Bimetallic Overalyer Structure

We have first studied the geometry and electronic properties of Pd-Cu bimetallic overlayer structure. After structural relaxation, the distances of Pd ovelayer are changed due to the compressive strain. The results are listed in Table 4-1. The compression effect due to lattice mismatch results in the increase of the distances between the surface two layers with 5.86% for compressed-Pd(111), 5.99% for 1L-Pd/Cu(111), 6.33% for 2L-Pd/Cu(111), and 6.42% for 3L-Pd/Cu(111), respectively.

The calculated partial density of states (PDOS) for surface Pd atoms of NL-Pd/Cu(111) are shown in Figure 4-2. It is found that the DOS of Cu near Fermi level is lower and that of Pd near Fermi level is higher due to the contribution of *d*-orbital. The high localized DOS near Fermi level in surface layer is considered to be related to the adsorption strength and catalytic activity of Pd. The PDOS of 2L-Pd/Cu(111) near Fermi level is the highest and that of 1L-Pd/Cu(111) near Fermi level is the lowest. The main contribution of substrate Cu is to induce the up-shift of the Fermi level of Pd due to the electron transfer from Cu to Pd. This charge transfer is estimated by calculating the difference of number of electrons for Pd overlayer with

Table 4-1. The calculated lateral spacing for slab model of 5L-Pd(111), compressed 5L-Pd(111), 5L-Cu(111) and NL-Pd/Cu(111). The bulk Cu and Pd lateral spacing values are 2.087Å and 2.246Å, respectively.

	Lateral spacing/Å			
		$1^{st} - 2^{nd}$	$2^{nd} - 3^{rd}$	$3^{rd} - 4^{th}$
Alloy				
	1L-Pd/Cu(111)	2.460	-	-
	2L-Pd/Cu(111)	2.468	2.244	-
	3L-Pd/Cu(111)	2.470	2.295	2.062
Metal			$1^{st} - 2^{nd}$	
	Pd(111)		2.321	
	Pd(111) (compressed)		2.457	
	Cu(111)		2.097	

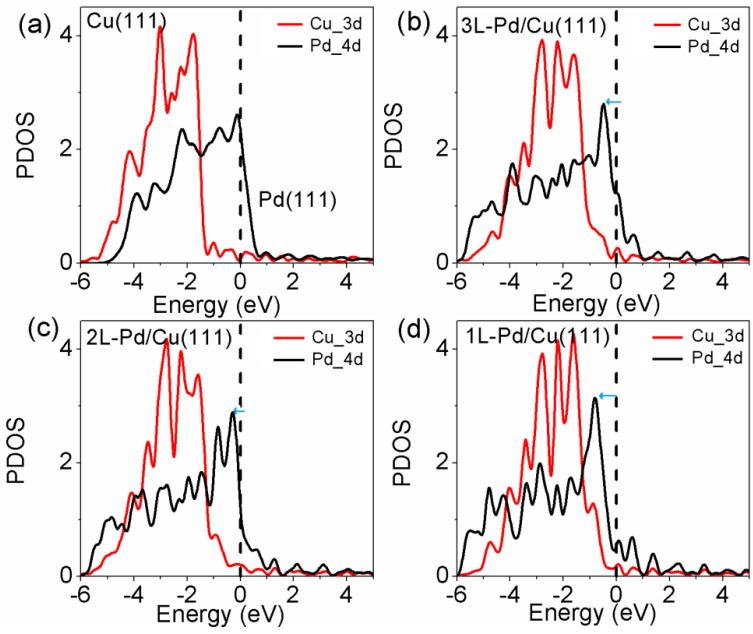

Figure 4-2. The calculated partial density of states for (a) pure 5L-Cu and 5L-Pd, (b) 3L-Pd/Cu(111), (c) 2L-Pd/Cu(111), and (d) 1L-Pd/Cu(111). It is found that the PDOS of Pd shifts downwards in the following order: Pd(111) > 2L-Pd/Cu(111) > 3L-Pd/Cu(111) > 1L-Pd/Cu(111).

and without Cu substrate, which is obtained by integrating the DOS of Pd overlayer. The results are summarized in Table 4-2. For NL-Pd/Cu(111) bimetallic system, the total charge transfer from substrate Cu to Pd overlayer is increasing as more Pd overlayer supported on Cu substrate. However, for Pd surface atoms of NL-Pd/Cu(111), the charge transfer decreases in the following order: 2L-Pd/Cu(111) > 3L-Pd/Cu(111) > 1L-Pd/Cu(111). This disorder phenomenon is consistent with the PDOS shift trend, which is modulated by the thickness of Pd overlayer. The calculated *d*-

band center of surface Pd atoms increases in the following order: 1L-Pd/Cu(111) (-2.55eV) < 3L-Pd/Cu(111) (-2.39eV) < 2L-Pd/Cu(111) (-2.28eV) < Pd(111) (-1.86eV). For 7-layer Pd_N/Cu(111) system, the same disorder trend is observed, which is shown as reference to prove that three-layer Cu substrate is enough and accurate to simulate Pd-Cu bimetal alloy. The calculated *d*-band center for 7-layer Pd_N/Cu(111) shift in the following order: Pd_1/Cu(111) (-2.53eV) < Pd_3/Cu(111) (-2.40eV) < Pd_2/Cu(111) (-2.31eV). It is noted that Pd overlayer has experienced compressive strain up to 8% due to lattice mismatch. In order to disentangle the effect of compression with the effect of substrate modulation effect, we have built a compressed Pd(111) structure with the same strain as NL-Pd/Cu(111). The compressive strain has shifted the *d*-band center downwards to -2.17eV. NL-Pd/Cu(111) (ranging from -2.28eV to -2.55eV) have more downward shifting *d*-band center compared with that of compressed Pd(111) (-2.17eV). This indicates that when forming bimetallic surface alloy, the shift of *d*-band center depends on both strain effect due to lattice mismatch and substrate modulation effect due to electron distribution and charge transfer between overlayer and substrate. We have then calculated the formation energies to test the stability for NL-Pd/Cu(111) by formula $E_{form} = E_{total} - E_{Cu(111)} - x(E_{Pd} - E_{Cu})$, where E_{total} represents the total energy of NL-Pd/Cu(111); $E_{Cu(111)}$ is pure Cu(111) slab; *x* denotes the relative amount of Cu atoms replaced by Pd atoms; E_{Pd} and E_{Cu} correspond to the bulk energy (per atom) of platinum and cooper, respectively. For the ovelayer structures studied here, 2L-

Pd/Cu(111) has a negative formation energy (-0.21eV), while that of 1L-Pd/Cu(111) (0.42eV) and 3L-Pd/Cu(111) (0.07eV) are positive. A negative formation energy corresponds to stable alloy.

Table 4-2. The calculated electron (charge) transfer per Pd (or Cu) atom of NL-Pd/Cu(111) bimetallic system. The surface Pd atom, subsurface Pd atom and third-layer Pd atom are presented by Pd^{1st}, Pd^{2nd} and Pd^{3rd}, respectively. The total electron (charge) changes of Pd overlayer are listed in the last row.

	Electron (charge) transfer			
	Pd^{1st} / per atom	Pd^{2nd} / per atom	Pd^{3rd} / per atom	Pd overlayer /total
1L-Pd/Cu(111)	0.049	-	-	0.196
2L-Pd/Cu(111)	0.015	0.085	-	0.400
3L-Pd/Cu(111)	0.024	0.048	0.072	0.576

4.3.2 Adsorption on Pd-Cu Bimetal Surface

Then we have investigated on the adsorption energies of atomic O, O_2 and CO on NL-Pd/Cu(111) surfaces as shown in Figure 4-3, where we have added some data from references. For the adsorption of molecules on the surface in the catalytic process, we need to estimate the change of free energies by considering the adsorption

energies with the contribution of entropy from the molecular vibration. However, compared to the effect of the electronic energy, the effect from the molecular vibration is small and can be ignored. The contribution of zero point energy is needed, since the internal stretch frequency has an obvious change in the process of adsorption. From the calculations, the contribution of zero point energy for CO adsorption at *fcc* site on Pd(111) is about 0.2eV. In this work, it is focused on the trend of adsorption energies on NL-Pd/Cu(111) surfaces. The contribution from zero-point energy will not change the calculated trend. Thus, the change of zero-point energy is not considered. For the adsorption on the surface, the adsorption energy is defined by the formula, $E_{ad} = E_{tot} - E_{slab} - E_A$, where E_{tot}, $E_{slab,}$ and E_A are the energies of the slab with adsorbate A, isolated slab for the clean metal surface, and isolated adsorbate A, respectively. The energy of atomic oxygen is defined as the half of that of O_2. Here, we have considered the most stable adsorption site for each species. Atomic O tends to bind on face-center cubic (*fcc*) site while O_2 binds on top-bridge-top (tbt) site (see Figure 4-1 for illustration). For the adsorption of CO, it is noted that traditional DFT method will overestimate the adsorption of CO due to the improper description for the CO-2π orbital.[167] From the previous reports, +U method can offer some improvement.[168] Here, we mostly focus on the trend of chemical reaction with the surface catalysis and the layer effect on catalysis. These results are not affected by the stronger adsorption of CO on *fcc* hollow site. Thus, for CO, we have calculated the adsorption energies on

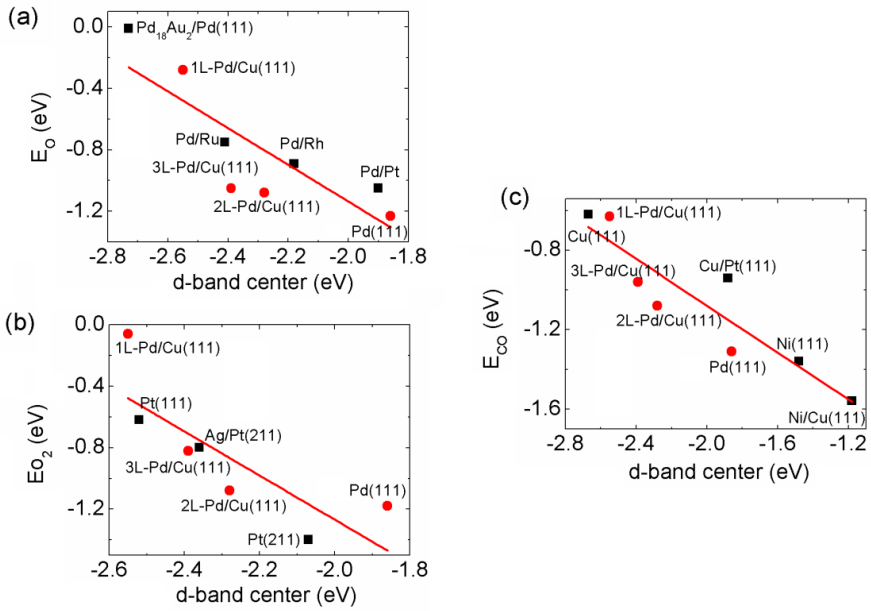

Figure 4-3. The calculated adsorption energies of (a) atomic O, (b) O_2 and (c) CO on NL-Pd/Cu(111) and Pd(111) as a function of the *d*-band center of surface Pd relative to the Fermi level (marked with red dot). The added data (marked in black square) are from Ref.[32, 44] for atomic O adsorption, Ref.[47, 169] for O_2 adsorption and Ref.[126] for CO adsorption, respectively. Noted that for CO adsorption, in order to be same with reference data, the adsorption energies are corresponding to *top* adsorption site.

both *fcc* and *top* sites. From Figure 4-3, there is a quasi-linear relationship between the adsorption energy and *d*-band center. This indicates that the energy of the *d* states (*d*-band center) relative to the Fermi level is a good indicator for the adsorption of O, O_2, and CO. It is noted that for CO adsorption, in order to be same with reference data, the adsorption energies are corresponding to *top* adsorption site. Again, we have shown

that the results are uncorrelated with the thickness of Cu substrate, we have listed the adsorption energies for NL-Pd/Cu(111) and 7-layer Pd_N/Cu(111) in Table 4-3.

Table 4-3. The calculated adsorption energies on NL-Pd/Cu(111) and 7-layer Pd_N/Cu(111). The adsorption sites (*fcc*, *top*, and *tbt*) can be viewed at Figure 4-1 for illustration.

Adsorption Energies/eV				
	O	O_2	CO	
	fcc	*tbt*	*fcc*	*top*
1L-Pd/Cu(111)	-0.28	-0.06	-1.11	-0.63
2L-Pd/Cu(111)	-1.08	-1.08	-1.76	-1.08
3L-Pd/Cu(111)	-1.05	-0.82	-1.72	-0.96
Pd_1/Cu(111)	-0.25	0.10	-1.04	-0.81
Pd_2/Cu(111)	-0.95	-1.17	-1.68	-1.15
Pd_3/Cu(111)	-1.09	-0.79	-1.53	-0.95

4.3.3 O_2 Dissociation and CO Oxidation on Pd-Cu Bimetal Surface

Next, we have focused on the O_2 dissociation mechanism and considered both direct O_2 dissociation and CO-assisted O_2 dissociation. The barriers are calculated by nudged elastic band (NEB) method.[170] The barrier is calculated by the difference between final state and transition state. The calculated energy barriers with respect to *d*-band center are shown in Figure 4-4 and Table 4-4. The reaction energy can be defined by the energy difference between dissociative adsorption of final state (FS)

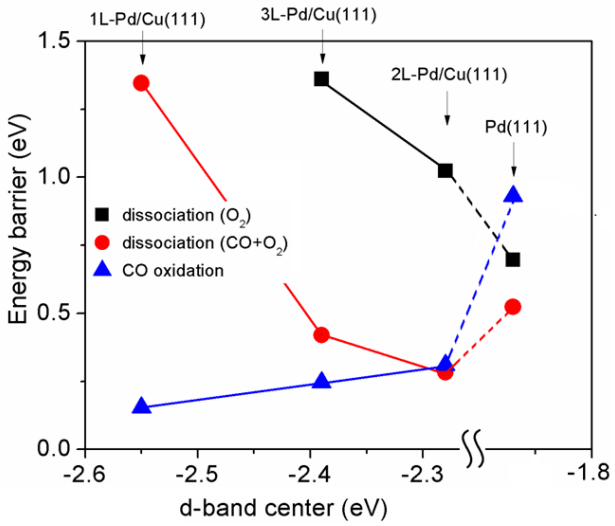

Figure 4-4. The calculated energy barriers for O_2 dissociation and CO oxidation with respect to *d*-band center. The black square represents O_2 direct dissociation; the red dot represents CO-assisted O_2 dissociation; the blue triangle represents CO oxidation. The added data for CO oxidation on Pd(111) is from Ref.[171] .

and molecular adsorption of initial state (IS) for O_2 by the formula, $\Delta E = E_{FS} - E_{IS}$. The calculated reaction energies (ΔE) for 1L-Pd/Cu(111), 2L-Pd/Cu(111), 3L-Pd/Cu(111), and Pd(111) are 0.35eV, -0.09eV, -0.25eV and -0.96eV, respectively. The dissociation of O_2 is not favored for 1L-Pd/Cu(111) with single-layer Pd due to endothermic reaction. O_2 can dissociate on Pd(111) surface easily with a low energy barrier (0.70eV). However the dissociation of O_2 adsorbed on NL-Pd/Cu(111) is relatively unfavorable at room temperature (1.02eV for 2L-Pd/Cu(111) and 1.36eV for 3L-Pd/Cu(111)). In order to figure out the CO + O_2 reaction on Pd overlayer, we have

considered the coadsorption case of CO and O_2 and analyzed the O_2 dissociation with the assistance of CO. Here, due to the competition of CO and O_2, the CO tends to bind on *top* site instead of *fcc* site in coadsorption case. For CO-assisted dissociation, the calculated reaction energies (ΔE) for 1L-Pd/Cu(111), 2L-Pd/Cu(111), 3L-Pd/Cu(111), and Pd(111) are -2.87eV, -3.34eV, -3.52eV and -2.21eV, respectively.

Table 4-4. The calculated reaction barriers for O_2 dissociation and CO oxidation on NL-Pd/Cu(111) and Pd(111) surfaces. It is noted that the direct dissociation of O_2 is not favored for 1L-Pd/Cu(111) with single-layer Pd due to endothermic reaction.

	Barrier/eV		
	O_2 dissociation		CO oxidation
	direct dissociation	CO-assisted dissociation	
1L-Pd/Cu(111)	-	1.35	0.15
2L-Pd/Cu(111)	1.02	0.28	0.31
3L-Pd/Cu(111)	1.36	0.42	0.25
Pd(111)	0.70	0.52	0.93 (Ref.[172])
Pt(111)	0.77(Ref.[47])	-	-
Au_{10}	-	0.31 (Ref.[27])	-
$Pd_{16}Au_4$	-	-	0.21 (Ref.[32])

The energy barriers obtained on 2L-Pd/Cu(111) and 3L-Pd/Cu(111) are greatly reduced to 0.28eV and 0.42eV, respectively. In addition, it is found that the barrier on

1L-Pd/Cu(111) is quite high (1.35eV) and this may be due to the weak coadsorption of CO and O_2 in single-layer Pd. The top view of selected states and the reaction path for CO-assisted O_2 dissociation are shown in Figure 4-5. It is clearly shown that the O_2 precursor will rotate from *tbt* site to *thb* (top-hcp-bridge) site to reach the transition states. The bond length will continue to be enlarged until reaching the final state.

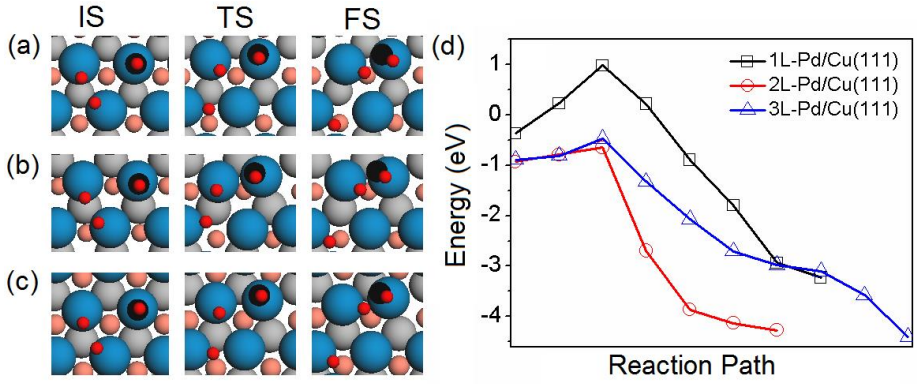

Figure 4-5. The top view of selected states along the path of CO-assisted O_2 dissociation for (a) 1L-Pd/Cu(111), (b) 2L-Pd/Cu(111) and (c) 3L-Pd/Cu(111) and (d) the corresponding reaction path.

After the dissociation of O_2, the CO oxidation with atomic O was investigated. The corresponding energy barriers are listed in Table 4-4 and the interpolated path and top view of selected states along the reaction path are shown in Figure 4-6. Along the CO oxidation path, the atomic O (represented by O*) try to move into the bridge site and CO moves closer to the lone O* atom. When CO_2 is formed on the surface of Pd, the C-O* distance is around 1.18Å. Our calculations show that the energy barriers for

1L-Pd/Cu(111), 2L-Pd/Cu(111), and 3L-Pd/Cu(111) are 0.15eV, 0.31eV, and 0,25eV, respectively. These barriers values are comparable to that of Pd-Au alloy[27] (0.31eV) and much smaller than that on Pd(111)[172] (0.93eV). This indicates that the series of Pd-overlayer systems NL-Pd/Cu(111) are very promising for low-temperature CO oxidation. After the formation of CO_2, the desorption of CO_2 on the surface is checked by calculating the energies of system along the desorption path. The results show that

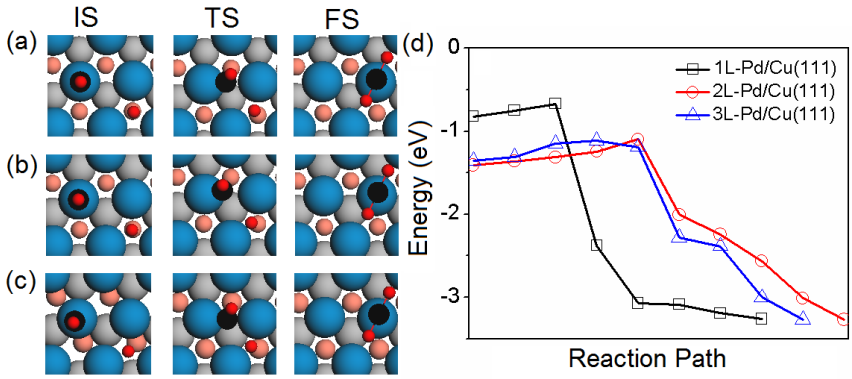

Figure 4-6. The top view of selected states along the path of CO oxidation for (a) 1L-Pd/Cu(111), (b) 2L-Pd/Cu(111) and (c) 3L-Pd/Cu(111) and (d) the corresponding reaction path.

CO_2 desorption on NL-Pd/Cu(111) surface is quite straightforward with a small barrier values around several meV which can be ignored. Additionally, some reference data is added into Table 4-4 to compare the calculated barriers with those from previous published papers. It is noted that the proposed 2L-Pd/Cu(111) can benefit from low CO-assisted O_2 dissociation barrier and low CO oxidation barrier.

4.3.4 Mechanism for Superior Catalytic Activity of Pd-overlayer

Next, we studied the mechanism for the catalytic activity of NL-Pd/Cu(111). From Figure 4-4, an obviously opposite trend is observed for the O_2 dissociation and CO oxidation. With the upshift of *d*-band center (closer to the Fermi level), the corresponding energy barriers decrease for the isolated O_2 dissociation (black line), while the corresponding energy barriers increase for CO oxidation (blue line). It is noted that the CO-assisted O_2 dissociation does not simply follow this rule. This phenomenon can be explained by the Sabatier principle.[95] It indicates that the best catalyst is a compromise that the interactions between adsorbate and surface (as a catalyst) should be neither too strong nor too weak during a catalytic reaction. We have then plotted the correlations between the energies of transition state and adsorption energies for O_2 dissociation and CO oxidation (known as Brønsted-Evans-Polanyi relations[173-174]). The BEP relations are shown in Figure 4-7. By fitting of these data, the BEP relations for O_2 direct dissociation and CO oxidation can be expressed by two simple formula, $E_{TS} = 1.535 \times Eo_2 + 1.367$ and $E_{TS} = 0.638 \times E_{CO+O} - 0.173$, respectively.

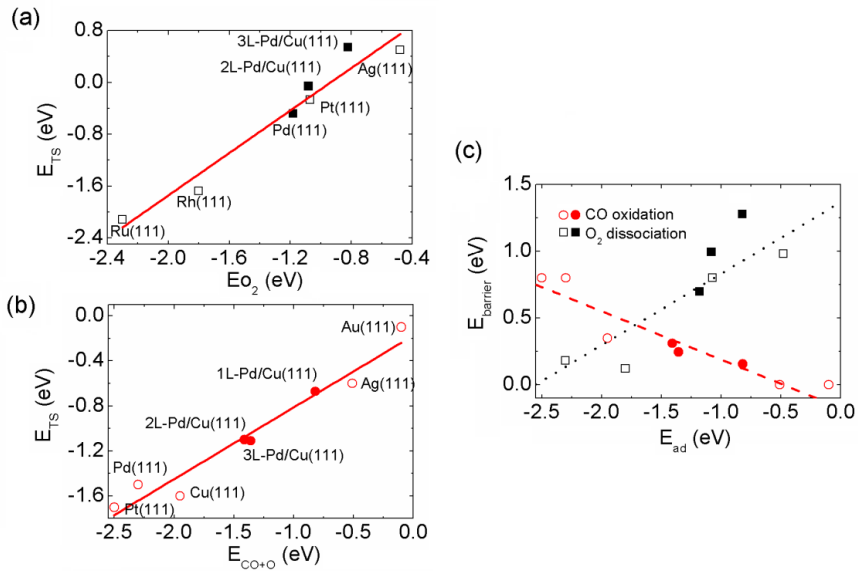

Figure 4-7. The plot of Brønsted-Evans-Polanyi relations for (a) O_2 dissociation (the red line is from the fitting formula $E_{TS} = 1.535 \times Eo_2 + 1.367$), (b) CO oxidation (the red line is from the fitting formula $E_{TS} = 0.638 \times E_{CO+O} - 0.173$) and (c) the derived energy barrier ($E_{barrier}$) with respect to the adsorption energy (E_{ad}) for both. Noted that in (a) and (b), the data with solid square/dot are from the calculation in this work and the data with hollow square/dot are from Ref.[173] for O_2 dissociation and CO oxidation; in (c), the red dash line represents CO oxidation and the black dot line represents O_2 dissociation.

The two linear relationships can verify the opposite trend for O_2 dissociation and CO oxidation with respect to *d*-band center as discussed below. Obviously, the barrier increases by following the decrease of the adsorption strength for the process of O_2 dissociation, while the barrier decreases by following the decrease of the adsorption

strength of O+CO for the process of CO oxidation. According to the *d*-band model, the interaction strength between the surface with transition metal and the adsorbate can be determined by the electronic structure of the surface metal atoms. The downshift of the *d* states away from the Fermi level usually corresponds to the decrease of the surface-adsorbate interaction. In our calculations, the downshifts of *d*-band centers of NL-Pd/Cu(111) and Pd(111) follow the order as, Pd(111) (-1.86eV) > 2L-Pd/Cu(111) (-2.28eV) > 3L-Pd/Cu(111) (-2.39eV) > 1L-Pd/Cu(111) (-2.55eV). For O_2 dissociation, the downshift trend of *d*-band center results in the decrease of the surface-adsorbate interaction and then the increase of energy barrier. However, for CO oxidation, the downshift trend results in the decrease of surface-adsorbate interaction and then the decrease of energy barriers. This is due to the fact that the strong interaction between O_2 and surface can help the breaking of O-O bond in O_2 dissociation and the weak interaction between O+CO and surface can enhance the diffusion of O and CO for the formation of CO_2 in CO oxidation with atomic O. Combining the two reactions for CO oxidation with O_2, the compromise for *d*-band center is needed. Experimentally, it presents as a volcano curve derived from Sabatier principle which describes the catalytic activity and catalytic performance corresponding to binding energies (or *d*-band center).[98] Interestingly, for the CO-assisted O_2 dissociation, it doesn't follow the simple linear relation with the *d*-band center. This is because there are the breaking of O-O bond and the diffusion of CO to help the breaking of O-O bond in the reaction.

This results in that 2L-Pd/Cu(111) has a proper *d*-band center and the lowest barrier. This also makes 2L-Pd/Cu(111) a good catalyst for CO oxidation from the Sabatier principle with the consideration of compromise.

4.4 Summary

The catalytic properties of NL-Pd/Cu(111) towards the reaction of CO oxidation are analyzed on the basis of fist-principle methods. With the Pd overlayer on Cu(111), the *d*-band center of surface Pd atoms is found to downshift away from the Fermi level. In addition, the *d*-band center is modulated by the thickness of overlayer and the shift of *d*-band center follows the order as 1L-Pd/Cu(111) (-2.55eV) < 3L-Pd/Cu(111) (-2.39eV) < 2L-Pd/Cu(111) (-2.28eV) < Pd(111) (-1.86eV). A quasi-linear relationship between adsorption energy and *d*-band center is observed. The more the *d*-band center shift downwards, the weaker the adsorption is for O, O_2, and CO. The disorder of *d*-band center shift for 2L-Pd/Cu(111) and 3L-Pd/Cu(111) is contributed to that the former has more localized electronic states near the Fermi level. With nudged elastic band (NEB) method, the energy barriers for O_2 dissociation and CO oxidation are explored. It is found that the energy barriers increase for the isolated O_2 dissociation and decrease for the CO oxidation by following the shift of *d*-band center of surface Pd. This opposite trend is proved using the derived relations about energy barrier and adsorption energy. This phenomenon is explained with the Sabatier principle and *d*-band theory. In addition, it is found that O_2 is easier to dissociate with

the assistant of nearby CO co-adsorbed on the surface. The corresponding energy barriers have been reduced from above 1eV to less than 0.5eV on 2L-Pd/Cu(111) and 3L-Pd/Cu(111) surface. It is predicted that the double-layer Pd as the overlayer on Cu substrate (2L-Pd/Cu(111)) has low CO-assisted O_2 dissociation barrier and low CO oxidation barrier. We hope our calculations can be useful for experimental works for designing oxidation catalyst.

Chapter 5 DFT Study on Pt-Cu Bimetal Alloy as Efficient Catalyst for H_2 Dissociation

In this chapter, we will present our work on bimetallic alloy Pt-Cu towards H_2 dissociation for the application of fuel cell anode materials. The overlayer model is used to simulate Pt-Cu bimetal alloy.

5.1 Overview

H_2 dissociation is the essential anode reaction in proton exchange membrane fuel cells (PEMFCs). It is well known that the performance and durability of PEMFCs are strongly influenced by impurities in the hydrogen fuel gas.[157, 175-176] Although platinum (Pt) shows high activity for the electro-oxidation of pure hydrogen, the poor CO-tolerance ability is one of the most known drawbacks for pure Pt as anode material.[177-178] This is due to the fact that the hydrogen supply is usually obtained by reforming hydrocarbons. The byproduct contains significant amounts of carbon monoxide (CO), which is impossible to remove completely. In recent years, the Pt-based metal alloys have been demonstrated to possess better CO-tolerance ability than pure Pt.[179-181] Binary alloys such as PtRu, PtSn and ternary alloys such as PtRuM, PtSnM have been extensively studied both experimentally[84, 182] and theoretically[183-184], where M represents transition metals. The enhanced catalytic activity are explained by ligand effect[182, 185] and bifunctional effect[186-187]. Pt ovelayers on top of various substrates including Pt alloys and non-Pt alloys are popular structures proposed to cut

Pt content down to realize the high utilization of Pt. These structures are experimentally favorable due to easy way of formation by phase segregations at elevated temperature.[188-189] In this work, a bimetallic overlayer structure with thin overlayers of Pt on supporting substrate Cu has been proposed. We have first checked the stability of Pt-Cu bimetallic alloy. Then the CO-tolerance ability and H_2 dissociation ability in combination with theoretical model are studied in detail.

5.2 Computational Methods

5.2.1 Pt-Cu Bimetallic Overlayer Structure

On the basis of the slab method, the pseudomorphic layer model was used to simulate the Pt overlayer structure, where the lateral lattice spacing is the same as bulk Cu. In order to study the effect of number of Pt overlayers, a (2×2) surface unit cell is built and calculated. Three models including single-layer, double-layer and triple-layer were considered to be covered on Cu substrate (three layers). We have used NL-Pt/Cu(111) to represent the structure with N-layer Pt as the overlayer on top of substrate Cu (three layers). It is noted that three-layer substrate is enough and accurate to simulate the overlayer structure. The *k*-point mesh[164] is set to be 5×5×1 during the calculations. After addressing the stability, we have focused on double-layer Pt model and built the following surface unit cells including (1×1), (1×2), (√3×√3), (2×2), (2√3×√3), (2×4) and (3×3) as shown in Figure 5-1 to study the adsorption energies as a function of surface coverage. When one H_2 molecule is adsorbed on the surface, the

respective coverages are 1ML, 1/2ML, 1/3ML, 1/4ML, 1/6ML, 1/8ML and 1/9ML. Additionally, $(2\sqrt{3}\times\sqrt{3})$ is used to calculate 2/3ML coverage with four H_2 molecules on the surface; and (2×2) is used to calculate 3/4ML coverage with three H_2 molecules. This description/definition apply to atomic H and CO surface adsorption coverage. The vacuum region is up to 15Å in order to avoid the spurious coupling effect in *z* direction for all structures. The corresponding *k*-point mesh[164] are 9×9×1, 10×5×1, 6×6×1, 5×5×1, 3×6×1, 4×2×1 and 3×3×1, respectively. The bottom two layers are fixed with the value of bulk Cu in the structural relaxation.

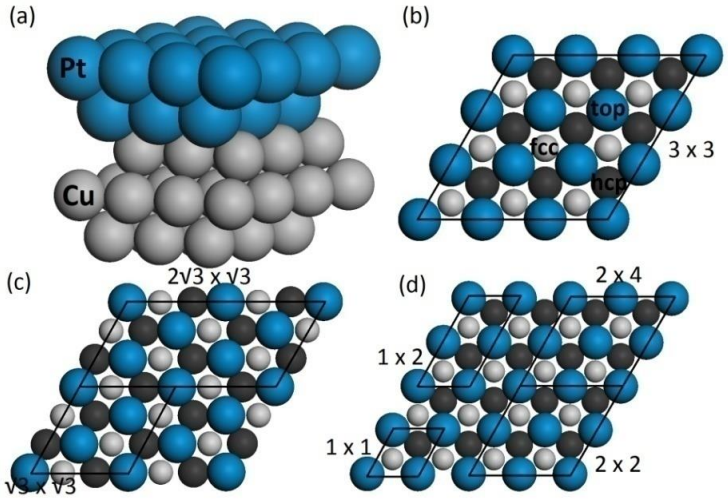

Figure 5-1. Schematic illustration of 2L-Pt/Cu(111)structure with (a) side view, and top view in (b) (3×3) surpercell, (c) √3×√3 and 2√3×√3 surpercell, and (d) 1×1, 1×2, 2×2 and 2×4 surpercell. The possible adsorption sites for H_2 and CO are highlighted with *top*, *fcc* and *hcp* bold symbols in Figure 5-1(b).

5.2.2 DFT Calculations

All the calculations were performed on the basis of spin-polarized DFT with projector augmented wave formalism, as implemented in the VASP code.[123, 165] The generalized gradient approximation with the parameterization of Predew-Burke-Ernzerhof was used for the exchange-correlation functional.[118, 166] A kinetic energy cutoff of 400eV for the plane wave expansion with proper k-point spacing using Monkhorst-Pack grid method[164] was found to be sufficient to ensure that the total energy was converged at 1meV/atom level. The convergence criterion for the self-consistence field energy was set to be 10^{-4}eV.

5.3 Discussions

5.3.1 Geometry of Pt-Cu Bimetallic Overlayer Structure

We have first studied the geometry and electronic properties of Pt-Cu bimetallic overlayer structure. After structural relaxation, the distance between the layers of Pt ovelayer and Cu substrate are changed due to the compressive strain. The results are listed in Table 5-1. The compression effect due to lattice mismatch results in the increase of the distances between the surface two layers with 5.22% for 1L-Pt/Cu(111), 7.48% for 2L-Pt/Cu(111), and 9.84% for 3L-Pt/Cu(111), respectively. For NL-Pt/Cu(111) studied here, the calculated *d*-band center shifts downwards (away from the Fermi level) in the following order Pt(111) (-2.44eV) > 2L-Pt//Cu(111) (-2.96eV) > 3L-Pt/Cu(111) (-3.01eV) > 1L-Pt/Cu(111) (-3.26eV). The calculated partial

densities of states of surface Pt atoms are shown in Figure 5-2. It can be found that the DOS of Cu near Fermi level is lower than that of Pt due to the contribution of *d*-orbital. By alloying, the Fermi level of surface Pt atoms is shifted upwards. In addition, the coupling between substrate Cu and overlayer Pt also results in the broadening of PDOS from the *d*-orbital of Pt. Therefore, the modulation of surface *d*-band center position for different thicknesses of Pt overlayer may be ascribed to the coupling with substrate Cu and charge transfer. We have estimated the charge transfer by calculating the difference of number of electrons for Pt overlayer with and without Cu substrate, which is obtained by integrating the DOS of Pt overlayer. We have summarized the results in Table 5-2. 2L-Pt/Cu(111) has the least electron transfer, while 1L-Pt/Cu(111) has the most electron transfer. We have then calculated the formation energies to test the stability for NL-Pt/Cu(111) by formula $E_{form} = E_{total} - E_{Cu(111)} - x(E_{Pt} - E_{Cu})$, where E_{total} represents the total energy of NL-Pt/Cu(111); $E_{Cu(111)}$ is pure Cu(111) slab; x denotes the relative amount of Cu atoms replaced by Pt atoms; E_{Pt} and E_{Cu} correspond to the bulk energy (per atom) of platinum and cooper, respectively. For the ovelayer structures studied here, 2L-Pt/Cu(111) has a negative formation energy (-0.36eV), while that of 1L-Pt/Cu(111) (0.62eV) and 3L-Pt/Cu(111) (0.10eV) are positive. A negative formation energy corresponds to stable alloy. Thus 2L-Pt/Cu(111) is chosen to perform the rest calculation and discussion.

Table 5-1. The calculated lateral spacing for slab model of 5L-Pt(111), compressed 5L-Pt(111), 5L-Cu(111) and NL-Pt/Cu(111). The bulk Cu and Pt lateral spacing values are 2.087 Å and 2.265 Å, respectively.

		Lateral spacing/Å		
		$1^{st} - 2^{nd}$	$2^{nd} - 3^{rd}$	$3^{rd} - 4^{th}$
Alloy				
	1L-Pt/Cu(111)	2.460	-	-
	2L-Pt/Cu(111)	2.513	2.261	-
	3L-Pt/Cu(111)	2.568	2.457	2.213
Metal		$1^{st} - 2^{nd}$		
	5L-Pt(111)	2.338		
	5L-Pt(111) (compressed)	2.574		
	5L-Cu(111)	2.097		

Table 5-2. The calculated electron (charge) transfer per Pt atom of NL-Pt/Cu(111). The surface Pt atom, subsurface Pt atom and third-layer Pt atom are presented by Pt^{1st}, Pt^{2nd} and Pt^{3rd}, respectively. The total electron (charge) changes of Pt overlayer are listed in the last row.

	Pt^{1st} / per atom	Pt^{2nd} / per atom	Pt^{3rd} / per atom	Pt overlayer /total
1L-Pt/Cu(111)	0.178	-	-	0.712
2L-Pt/Cu(111)	-0.091	0.143	-	0.208
3L-Pt/Cu(111)	-0.018	-0.036	0.164	0.440

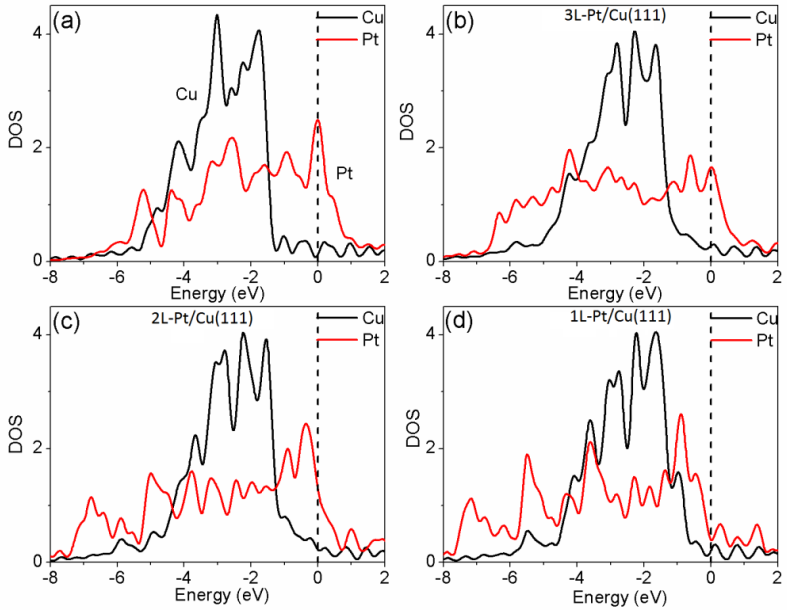

Figure 5-2. The calculated partial density of states of (a) 5L-Cu(111) and 5L-Pt(111), (b) 3L-Pt/Cu(111), (c) 2L-Pt/Cu(111), and (d) 1L-Pt/Cu(111). The black dash line represents the Fermi level.

5.3.2 CO Saturation Coverage on 2L-Pt/Cu(111) Surface

We have then studied the CO saturation coverage on Pt(111) and 2L-Pt/Cu(111) by calculating the differential adsorption energy (E_{diff}) to represent the repulsive interaction between CO molecules. This is calculated by considering the change of total energy for the reaction nCO*surface + CO(g) → (n+1)CO*surface, which can be regarded as a key reactivity descriptor for CO poisoning. It is noted that CO adsorption sites on Pt surface are inappropriately predicted by first principle calculation.[91, 190] Recently, methods such as random phase approximation (RPA) can predict good

adsorption energies and correct CO adsorption site.[191] In this work, our focus is on the competition effect of CO and H_2 with respect to the surface adsorption coverage to solve the CO poison issue. So the actual adsorption energy is not that important. On the contrary, the relative chemical trend as a function of the surface coverage is more of our concern. Thus, we have initially forced CO to remain on top site of Pt facets as observed experimentally and fully relax during the calculation with traditional PBE calculations. The results should be reliable in terms of relative chemical trend and this PBE calculation consumes much fewer computing resources compared with GW-RPA approximation. To calculate the adsorption energy (E_{ad}) as a function of surface CO coverage on pure Pt and 2L-Pt/Cu(111), we have built various surface models with the surface coverage ranging from 1/9ML (3×3 unit cell) to 1ML (1×1 unit cell) (see Figure 5-1 for illustration). For the adsorption on the surface, the adsorption energy is defined by the formula, $E_{ad} = E_{tot} - E_{slab} - E_A$, where E_{tot}, $E_{slab,}$ and E_A are the energies of the slab with adsorbate A, isolated slab for the clean metal surface, and isolated adsorbate A, respectively. The adsorption energies of H_2 and atomic H are referenced to H_2 (g) and half of H_2(g), respectively. The results are shown in Figure 5-3. It is clearly shown that pure Pt is suffered from CO poisoning with the high saturation coverage (more than 2/3ML). However, the saturation coverage on 2L-Pt/Cu(111) is greatly reduced to the value between 1/3ML and 1/2ML. Due to lattice mismatch, Pt overlayers are compressed with up to 7.88% to fit bulk Cu lattice. A compressed five-

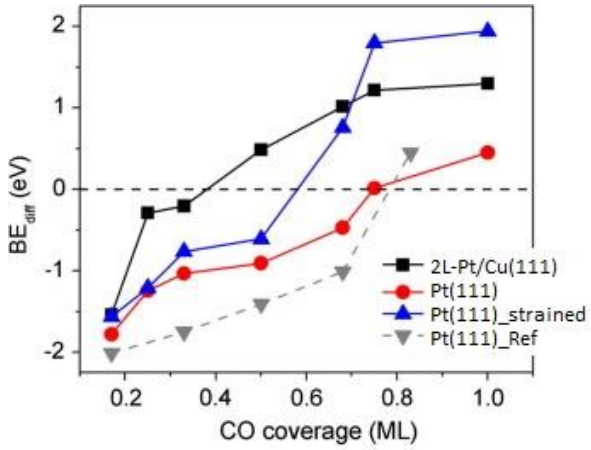

Figure 5-3. The calculated differential binding energy (BE_{diff}) for CO as a function of CO coverage on 2L-Pt/Cu(111), strained Pt(111) and pure Pt(111). The solid lines are from our calculations and the dash line is from Ref.[192] for pure Pt. The differential adsorption energy BE_{diff} is defined as the change of total energy for the reaction nCO*surface + CO(g) $\rightarrow$ (n+1)CO*surface, where nCO*surface means n CO molecules adsorbed on surface. A positive differential binding energy indicates that the respective state is not stable on the surface.

layer Pt slab along [111] direction denoted as compressed Pt(111) was built to disentangle the compression effect with the effect of charge transfer. The saturation coverage on compressed Pt(111) is reduced to 1/2ML, which has the same lattice constant as 2L-Pt/Cu(111). This indicates that the adsorption strength is affected by both strain effect due to lattice mismatch and electronic effect due to charge transfer.

The reduced CO saturation coverage can offer more free surface sites for the catalytic reaction of H_2 to H.

We have then studied the competition effect between CO and H_2 upon the coadsorption by calculating the isolated adsorption energies of CO and H_2 molecules for coverage ranging from 1/9ML (3×3 unit cell) to 1/2ML (1×2 unit cell). The calculated adsorption energies are shown in Figure 5-4. It is found that CO tends to bind stronger than H_2 molecule. In addition, the adsorption strengths of CO and H_2 on both surfaces (pure Pt and 2L-Pt/Cu(111)) are decreased as the increase of surface coverage. This trend may be due to the decreasing of available adsorption sites on surface and the coupling between adsorbed CO molecules. The coupling results in decrease of adsorption strength with the repulsion effect between CO molecules. These results on pure Pt is in accordance with other experimental data and theoretical simulations.[193-194] For reference, we have also shown the adsorption energies of CO on compressed Pt(111) in Figure 5-5. The adsorption energy is decreasing with increasing CO coverage, which is the same as the trend on Pt(111) and 2L-Pt/Cu(111). In addition, the adsorption strength of CO on the surface of compressed Pt(111) is weaker than on Pt(111) but stronger than on 2L-Pt/Cu(111). This is consistent with the trend of differential adsorption energy for these cases.

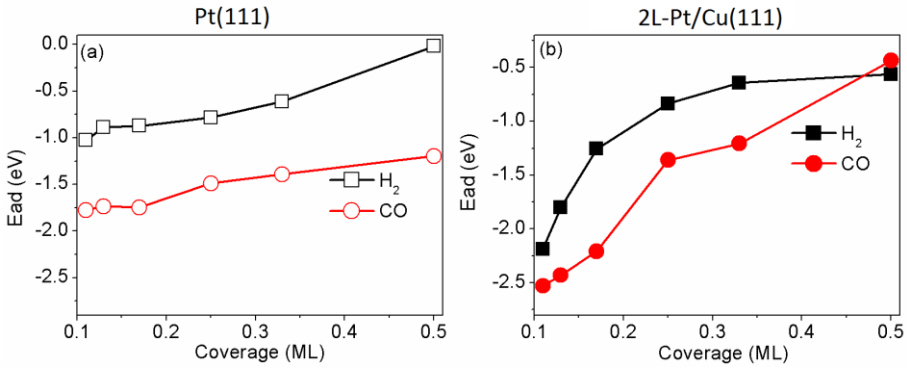

Figure 5-4. The calculated adsorption energies of isolated CO, H_2 with different coverage on (a) Pt surface and (b) 2L-Pt/Cu(111) surface. The various coverage are obtained with surface unit cells including (1×1), (1×2), (√3×√3), (2×2), (2√3×√3), (2×4) and (3×3).

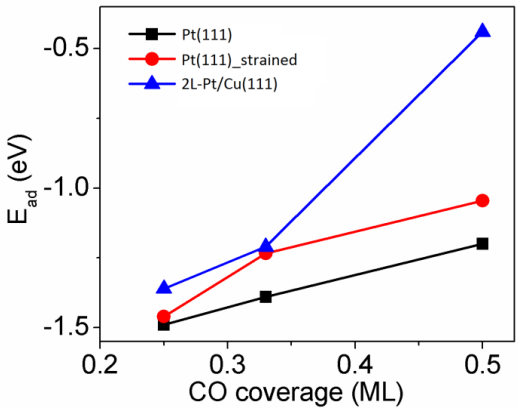

Figure 5-5. The calculated adsorption energies of CO on Pt(111), compressed Pt(111) and 2L-Pt/Cu(111) surface. It is noted that the adsorption strength of CO on the surface of compressed Pt(111) is weaker than on Pt(111) but stronger than on 2L-Pt/Cu(111).

5.3.3 Reactivity of CO-covered 2L-Pt/Cu(111)

After investigation on the CO saturation coverage, we have then studied the reactivity of 2L-Pt/Cu(111) by calculating the H_2 dissociation barrier as a function of CO coverage and H_2 coverage, which can represent the anode catalytic activity to some degree. The nudged elastic band (NEB) method[170] was used to search the minimum energy path and determine the transition state (TS) for H_2 dissociation. The results are listed in Table 5-3. For isolated H_2 adsorption (zero CO coverage), it is found that H_2 can dissociate freely on pure Pt and 2L-Pt/Cu(111) surfaces for all coverage. The result on pure Pt is consistent with the previous reports.[192] For the coadsorption of CO and H_2 with low coverage (less than 1/6ML), the H_2 molecules also dissociate freely on the surface. The dissociation barrier increases with increased CO or H_2 coverage. For high coverage (larger than 1/2ML), H_2 molecule is difficult to dissociate due to weak adsorption strength. We have compared the barrier values of 2L-Pt/Cu(111) structure with those of pure Pt and Pt/Ru as shown in Figure 5-6, where the data for pure Pt and Pt/Ru are from Ref.[192]. It can be found that pure Pt has higher CO saturation coverage and the energy barrier of H_2 dissociation increases greatly (around 1.5eV) as the increase of CO coverage on the surface, though the energy barrier is much lower when the CO coverage rate is lower. The CO saturation coverage of 2L-Pt/Cu(111) and Pt/Ru is much smaller than that of pure Pt. When the coverage rate of CO is lower, 2L-Pt/Cu(111) has lower energy barrier of H_2 dissociation than that of Pt/Ru (see Figure 5-6 for illustration). This can be explained

by *d*-band center theory. With the compression effect due to lattice mismatch and the effect of charge transfer, the electronic structures of both structures (2L-Pt/Cu(111) and Pt/Ru) are modulated and the *d*-band center is shifted downwards with the change of quasi-localized density of states. The downwards shifting of *d*-band center of 2L-Pt/Cu(111) (-2.96eV) is more than that of Pt/Ru (*d*-band center is at -2.76eV[195]). The adsorption strength is related to *d*-band center and CO molecule can bind stronger on Pt/Ru surface than on 2L-Pt/Cu(111) surface which leads to higher CO saturation coverage for Pt/Ru. In terms of the lower dissociation barrier, we can conclude that 2L-Pt/Cu(111) structure is very promising to serve as an alternate anode material.

Table 5-3. The calculated H_2 dissociation barriers with respect to different H_2 and CO coverage for (1×2), (√3×√3), (2×2) and (2√3×√3) on 2L-Pt/Cu(111) surface. The dissociation of H_2 becomes difficult on the surface under high CO and/or H_2 coverage.

Barrier (eV)				
H_2/ML / CO/ML	1/6	1/4	1/3	1/2
0	0	0	0	0
1/6	0	-	0.022	0.237
1/4	-	0.068	-	0.472
1/3	0.101	-	0.335	-
1/2	0.552	0.728	-	-

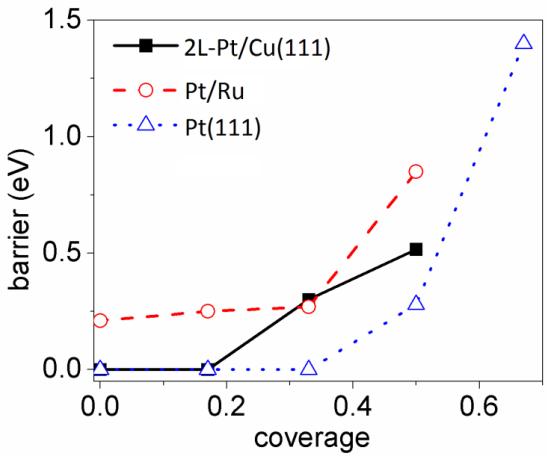

Figure 5-6. The calculated H_2 dissociation barrier with respect to different CO coverage on 2L-Pt/Cu(111) surface, compared with that on Pt(111) and Pt/Ru surface. The solid lines are from our calculations and the dash line is from Ref.[192]. The various coverages are obtained with surface unit cells including (1×2), (√3×√3), (2×2), (2√3×√3).

5.3.4 Modeling of CO Poisoning on 2L-Pt/Cu(111) Surface

In order to show the competition effect between CO and H_2 adsorption on Pt overlayer surface, we have built a theoretical model to illustrate the coadsorption case. The hydrogen coverage[195] can be expressed as,

$$\theta_H = \frac{\sqrt{K_H P_{H_2}}}{1 + K_{CO} P_{CO} + \sqrt{K_H P_{H_2}}} \qquad (5.1)$$

where K_H and K_{CO} represent the equilibrium constants and P_{H2} and P_{CO} represent the pressures of H_2 and CO. The equilibrium constants ($Ki, i = H, CO$) can be derived from the basic thermodynamic equation and the results are expresses as $K_i =$

$\exp\left(-\frac{\Delta E_i - T\Delta S_i}{kT}\right)$, where ΔE_i and ΔS_i are the changes of energy (enthalpy) and entropy upon the adsorption of molecules, respectively. For the change entropy due to the adsorption, the results on different metal surfaces can vary. But the differences on the surfaces of different Pt-based alloys are small and can be ignored. In this work, we have adopted the following values for H and CO: $\Delta S_H = 136\ {}^{J}/_{(mol \cdot K)}$ and $\Delta S_H = 202\ {}^{J}/_{(mol \cdot K)}$ as listed in previous report[195]. For the enthalpy, the results can be obtained by either experimental measurement or theoretical calculations. We have shown that the adsorption energies of CO and H_2 vary with different surface coverage. This is in accordance with various experimental measurement values.[179, 194] Here, we have chosen the corresponding adsorption energy for 1/4ML surface coverage to be substituted in the above equations and the results are shown in Figure 5-7. We have considered three different typical operation temperatures for PEMFCs including 300K, 323K and 353K. For comparison, we have shown the equilibrium CO coverage on Pt surface from literature in Figure 5-8.[179] From both figures, it is clearly seen that increasing operation temperature can greatly improve the CO-tolerance ability. When operating at the same temperature, the proposed 2L-Pt/Cu(111) structure has better CO-tolerance ability than pure Pt. For example, at 300 K, surface H coverage is greatly increased than that on pure Pt; at 353K, as shown in Figure 5-7(b), the CO surface coverage on 2L-Pt/Cu(111) is obviously lower than that of Pt.

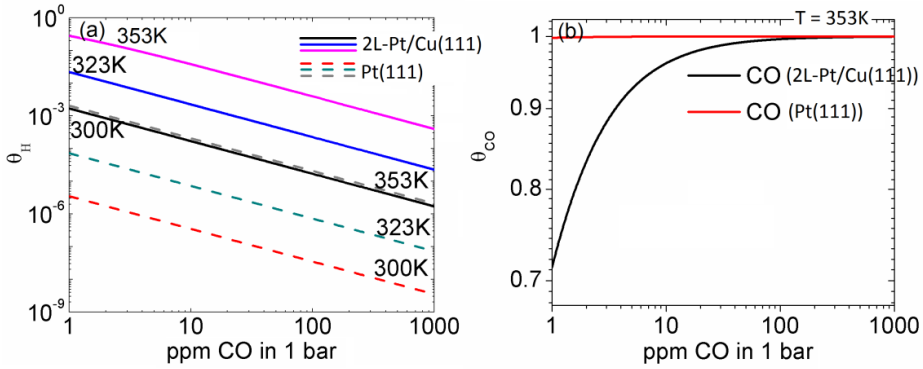

Figure 5-7. The calculated (a) variations in the hydrogen coverage as a function of the CO partial pressure with various operation temperatures. The H_2 partial pressure is 1 atm. The solid lines represent results for 2L-Pt/Cu(111) and the dash lines represent results for Pt. The CO coverage for operating temperature at 353K is shown in (b) to illustrate the alleviated CO poison issue on 2L-Pt/Cu(111) surface.

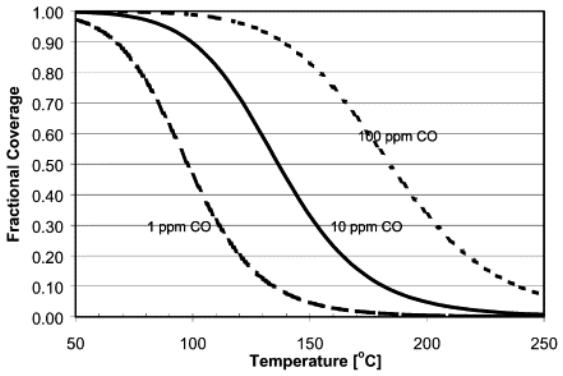

Figure 5-8. CO coverage on a platinum surface as a function of temperature and CO concentration. H_2 partial pressure is 0.5 bar. (Reprinted with permission from Ref. [179])

5.4 Summary

The catalytic reactions on thin Pt overlayer (NL-Pt/Cu(111)) on substrate Cu have been investigated by the combination of first principle methods and analysis of theoretical model. The layer effect has been checked with the supporting of *d*-band center model. In terms of stability, the double-layer Pt on substrate Cu (2L-Pt/Cu(111)) is found to have negative formation energy (-0.36eV) while that of 1L-Pt/Cu(111) and 3L-Pt/Cu(111) is positive. The CO-tolerance ability is studied with the double-layer model 2L-Pt/Cu(111). It is found that 2L-Pt/Cu(111) has much lower CO saturation coverage (40%) compared with that of pure Pt (75%). This reduced saturation coverage is related to weaker adsorption strength of CO. This implies CO in 2L-Pt/Cu(111) is removed more easily via oxidation. The H_2 dissociation barrier with various CO and H_2 coverage are calculated by NEB methods. The results show that the dissociation barrier from H_2 to H becomes higher with increased CO and/or H_2 coverage. Under the saturation coverage (40%), the dissociation barrier for 2L-Pt/Cu(111) is less than 0.4eV. Especially, under the low coverage of CO, the dissociation barrier can be ignored. With the theoretical analysis model, it is found that the CO-tolerance ability on 2L-Pt/Cu(111) is improved dramatically than that on Pt. By comparison with Pt/Ru alloy, it is found that 2L-Pt/Cu(111) has lower CO saturation coverage. This indicates that 2L-Pt/Cu(111) can serve as alternate anode material. We hope our calculation can stimulate the exploration of catalysis of Pt/Cu bimetallic alloy.

Chapter 6 DFT Study on Pd-based Intermetallic Alloy as Efficient Catalyst for Oxygen Reduction Reaction

In this chapter, we will present our work on Pd-based intermetallic alloy as oxygen reduction reaction catalyst. The proposed structure consists of Pd-monolayer on top of Pd-M (M=Cu, Ni, Fe) intermetallic alloy.

6.1 Overview

Low-temperature polymer electrolyte membrane fuel cells are widely researched for years due to their low environmental impact, high power density and high energy conversion efficiency. However, the sluggish kinetics of cathode oxygen reduction reaction is one of the major obstacles to hinder the large-scale application for PEMFCs.[196-198] Pt and its alloy have been extensively studied for decades in order to improve the performance and enhance the durability by minimizing Pt content.[199] In recent years, Pt-monolayer electrocatalysts on top of various substrates including Pt-M alloy (M represents transition metals) and non-Pt-M alloy are designed and synthesized.[200-202] These Pt-monolayer structures are promising cathode materials due to low Pt content and tunable activity through the choice of various cores. In order to further limit the usage of Pt, the idea of Pt-free cathode materials has been proposed.[143, 203-204] However, it is not easy to search for suitable Pt-free electrocatalysts considering that only a few materials are stable in the acidic environment. Among the possible candidates, palladium (Pd) and its alloy have

attracted much attention due to remarkable ORR efficiency.[159, 205-206] Previous studies have indicated that Pd-M catalysts can undergo phase segregations upon annealing at elevated temperatures, resulting in Pd-monolayer on top of Pd-M substrates.[44] However, compared with state-of-art carbon supported Pt or Pt-monolayer electrocatalyts, these Pd-monolayer structures have limited activity due to poor stability under practical operating conditions.[207-208] Much efforts have been dedicated to address this problem.[209] Very recently, Pd-based ordered intermetallic nanoparticles have been successfully synthesized and characterized.[143, 210-211] Experimentally, Pd skin do not always adopt the lattice constant of the bulk material.[212] Pd skin on top of Pd-based intermetallic alloy shows unusual adsorption behavior partly as a result of strain effect. Jiang *et al.*[213] argues that by controlling the Pd shell thickness, the core/shell face-centered tetragonal *fct*-FePd/Pd nanoparticles show different ORR activity and durability. Among the thickness studied in their work, 0.65nm Pd shell are more active and durable for ORR compared with Pd shell with 0.27nm or 0.81nm. They have attributed this enhancement to the desired compressive strain induced by *fct*-FePd core. Wang *et al.*[210] have developed possible synthesis method to transform PdCu nanoparticle from disorder face-centered cubic *fcc* structure to ordered body-centered cubic *bcc* structure. They have found that Pd skin on top of *bcc*-PdCu intermetallic alloy have better thermodynamic stability and moderate binding energy to oxygen-containing intermediates. In this work, we have proposed Pd monolayer

structure as efficient oxygen reduction reaction catalyst. Based on experimental results, we have adopted *bcc*-PdCu and *fct*-PdFe (or PdNi) as supporting core.

6.2 Computational Methods

6.2.1 Pd-based Intermetallic Alloy Structure

In order to investigate the surface reactivity of Pd monolayer structure, we have adopted the slab model by building pseudomorphic layer. Pd monolayer is placed on top of four-layer *bcc*-PdCu(110) and *fct*-PdM(111) (M=Ni, Fe), where the lateral lattice spacing is the same as the substrate. Due to lattice mismatch, the Pd monolayer have experienced compression strain up to 4.56% on PdNi(111) and 3.04% on PdFe(111), respectively. For Pd/PdCu(110) system, the compression strain is not addressed due to the phase transformation. The proposed Pd monolayer structure is shown in Figure 6-1 and the calculated lattice constant for intermetallic alloy unit cell is listed in Table 6-1. We have built (2×4) surface unit cells to represent the sample surface, with minimum adsorption coverage up to 1/8 ML. The vacuum region is up to 15Å to avoid the spurious coupling effect along *z* direction for all slab structures. The bottom two layers are fixed with the value of bulk alloy in the structure relaxation. During the calculations, we have used 5×2×1 *k*-point mesh[164] for *fct*-PdM(111) (M=Fe, Ni) structures and 4×3×1 *k*-point mesh[164] for *bcc*-PdCu(110) structures.

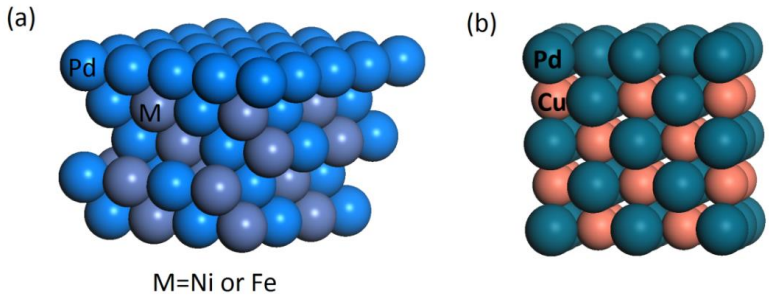

Figure 6-1. The configurations of (a) side view of *fct*-Pd/PdM(111) and (b) *bcc*-Pd/PdCu(110). M represents Ni or Fe atoms.

Table 6-1. The calculated lattice constant for intermetallic alloy *fct*-PdM and *bcc*-PdCu unit cell. M represents Ni or Fe.

	Structure	Lattice constant	
		a /Å	c /Å
Pd	*fcc*	3.95	3.95
Cu	*fcc*	3.63	3.63
PdCu	*bcc*	3.02	3.02
PdNi	*fct*	3.83	3.79
PdFe	*fct*	3.77	3.70

6.2.2 DFT Calculations

All the calculations were performed on the basis of spin-polarized DFT with projector augmented wave formalism, as implemented in the VASP 5.3.3 code. [123, 165] The generalized gradient approximation with the parameterization of Predew-Burke-Ernzerhof was used for the exchange-correlation functional.[118, 166] A kinetic energy cutoff of 400eV for the plane wave expansion with proper k-point spacing using

Monkhorst-Pack grid method[164] was found to be sufficient to ensure that the total energy was converged at 1meV/atom level. The convergence criterion for the self-consistence field energy was set to be 10^{-4}eV.

6.3 Discussions

6.3.1 Geometry of Pd Monolayer Supported on Pd-based Intermetallic Alloy

We have first investigated the geometry of proposed Pd-monolayer structure. The proposed structure consists of monolayer Pd on top of four-layer *fct*-PdM(111) or *bcc*-PdCu(110). We have calculated the *d*-band center (ε_d) for surface Pd atom and the results are listed in Table 6-2. The *d*-band center is found to shift upwards in the following order Pd/PdFe(111) (-2.38eV) < Pd/PdNi(111) (-2.24eV) < Pd/PdCu(110) (-1.93eV) < Pd(111) (-1.86eV). In order to understand this shifting trend, we have calculated the partial density of states of surface Pd atom for various structures are shown in Figure 6-2. The localized PDOS of Pd atom for various structures near the Fermi level have the same shift trend as that of *d*-band center position. Especially, the localized PDOS of Pd/PdFe(111) has shifted more along negative direction than that of Pd/PdNi(111) and Pd/PdCu(110). In order to study the strain effect, we have calculated the *d*-band center of strained Pd(111) with the compression strain the same as Pd/PdFe(111) and Pd/PdNi(111) and the results are listed in Table 6-2. It is noted that under the same strain condition, the *d*-band center of compressed Pd(111) and

Table 6-2. The calculated *d*-band center (ε_d) and estimated electron transfer for surface Pd atoms. For the two compressed_Pd models, the compression strain are set to be the same with Pd/PdNi(111) and Pd/PdFe(111), respectively.

	d-band center /eV	Electron transfer /eV	Pd-Pd distance /Å
Pd/PdFe(111)	-2.38	-0.73	2.67
Pd/PdNi(111)	-2.24	1.60	2.63
compressed_Pd (PdNi)	-2.16	-0.17	2.64
compressed_Pd (PdFe)	-2.05	-0.22	2.69
Pd/PdCu(110)	-1.93	2.66	-
Pd(111)	-1.86	-	2.75

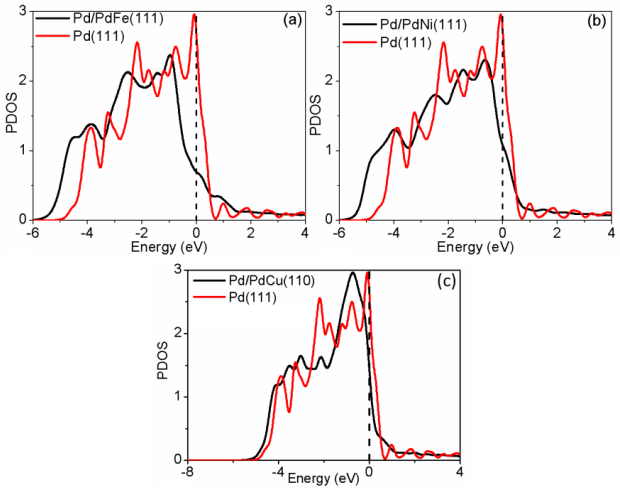

Figure 6-2. The calculated partial density of states for Pd atom on (a) Pd/PdFe(111), (b) Pd/PdNi(111), and (c) Pd/PdCu(110) surfaces. The black dash line represents the Fermi level.

Pd/PdM(111) differ from each other. This is due to the fact that the position of *d*-band center is modulated by both strain effect due to lattice mismatch and electron distribution due to charge transfer. We have estimated the charge transfer by calculating the difference of number of electrons for Pd monolayer with and without the substrate for Pd/PdCu(110), Pd/PdM(111) and compressed Pd(111). This is obtained by integrating the DOS of Pd monolayer and the results are shown in Table 6-2. The negative value represents that the electron transfer is from Pd monolayer to substrate and positive value represents that the electron transfer is from substrate to Pd monolayer. It is expected that the manipulating of surface activity of Pd-monolayer can be ascribed to both compression strain and charge/electron transfer. In order to gain further insight of the strain effect, we have built five-layer Pd(111) with compression strain ranging from 1% to 5%. It is found that the more the compression strain, the further the *d*-band center shift away. Pd(111) with 1% strain has a *d*-band center value up to -1.91eV, while Pd(111) with 5% strain has a *d*-band center value up to -2.01eV. We have tested the effect of strain by calculating the adsorption energies of atomic oxygen. The results are shown in Figure 6-3. It is found that strain can relieve the strong adsorption strength.

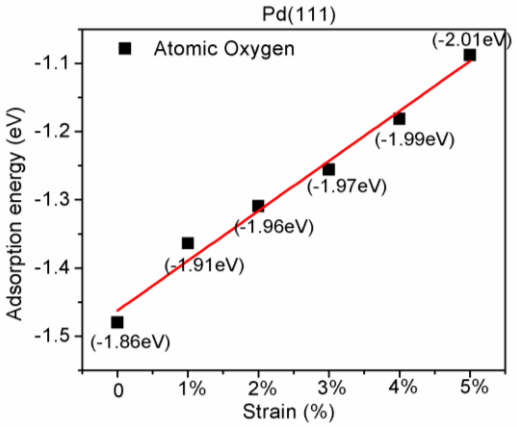

Figure 6-3. The calculated atomic oxygen adsorption energies as function of compressive train on Pd(111) surface. The inserted values are *d*-band center values. The more the compression strain, the further the *d*-band center shift away.

6.3.2 Adsorption of O_2 on Pd Monolayer Supported on Pd-based Intermetallic Alloy

We have then investigated the O_2 adsorption on various Pd monolayer surfaces. For the adsorption on the surface, the adsorption energy (E_{ad}) is defined by the formula, $E_{ad} = E_{tot} - E_{slab} - E_A$, where E_{tot}, E_{slab}, and E_A are the energies of the slab with adsorbate A, isolated slab for the clean metal surface, and isolated adsorbate A, respectively. From the definition, a negative value of E_{ad} corresponds to exothermic adsorption. The energy of atomic oxygen (hydrogen) is defined as the half of that of O_2 (H_2). The possible adsorption sites are shown in Figure 6-4. The results show that O_2 is more stable on *tbt* site on Pd/PdNi(111) and Pd/PdCu(110) surfaces, while it tends to bind on *top* site on Pd/PdFe(111) surface. In order to study the potential pathway of ORR, we have calculated the adsorption energies of ORR species including atomic O, OH, OOH and H_2O. The results are listed in Table 6-3. For

comparison, we have calculated the adsorption energies of ORR species on five-layer Pd(111) surface. O_2 tends to bind on *tbt* site on Pd(111) surface. ORR species are found to bind stronger on Pd(111) surface than on Pd monolayer. We have drawn the relationship between adsorption energy and *d*-band center as shown in Figure 6-5. Compared with pure Pd, Pd monolayer on top of Pd-based intermetallic alloy has moderate adsorption strength. This follows the linear relationship derived from *d*-band center theory.[98] We can see that the final product H_2O can be easily removed from the catalyst surface due to weak interaction with the surface.

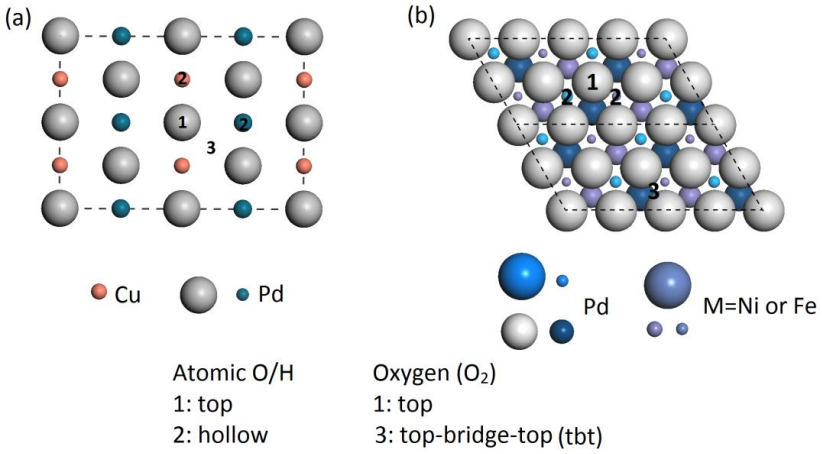

Figure 6-4. The configurations of top view of (a) Pd/PdCu(110) and (b) Pd/PdM(111) (M=Ni, Fe). The possible adsorption sites in bold number 1, 2, and 3 represent top site, hollow site and top-bridge-top (tbt) site, respectively.

Table 6-3. The calculated adsorption energies (E_{ad}) of ORR species (O_2, atomic O, OH, OOH, and H_2O) on Pd/PdFe(111), PdNi(111), Pd/PdCu(110) and Pd(111) surfaces.

	E_{ad} / eV			
	Pd/PdFe(111)	Pd/PdNi(111)	Pd/PdCu(110)	Pd(111)
O_2	-0.11	-0.44	-0.73	-0.91
O	-0.67	-0.79	-1.18	-1.48
OH	-1.58	-1.54	-1.86	-2.04
OOH	-0.78	-0.93	-1.01	-1.52
H_2O	-0.08	-0.03	-0.13	-0.34

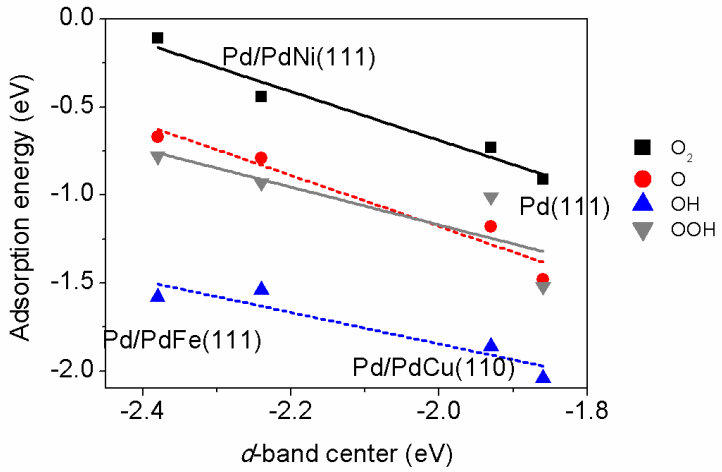

Figure 6-5. The calculated adsorption energies for O_2, atomic O, OH and OOH as a function of the *d*-band centerfrelative to Fermi level.

Following the adsorption on the surface, O_2 will undergo two possible reactions including direct dissociation into atomic O and hydrogenation into OOH. Our calculations have indicated that O_2 will undergo direct dissociation on Pd/PdCu(110)

surface while it tends to go through hydrogenation into OOH on Pd/PdNi(111) and Pd/PdFe(111) surfaces. The calculated energy barriers are listed in Table 6-4. For Pd/PdCu(110), the calculated direct dissociation barrier is as low as 0.60eV. This barrier value is easy to overcome under normal operating temperature. The top view of selected states along the dissociation path are shown in Figure 6-6. It is clearly seen that the O_2 precursor will rotate from *tbt* site at the beginning to reach the transition state, where the two oxygen atoms are stretched to opposite direction gradually. The distance will continue to be enlarged until reaching the final state. For the case of hydrogenation into OOH, the process is thermodynamically unfavorable ($O_2^* + (H^+ + e^-) \rightarrow OOH^*$) due to endothermic reaction. However, the situation for Pd/PdNi(111) and Pd/PdFe(111) show the opposite trend. The direct dissociation is not favorable due to high barrier values, which are up to 0.93eV for Pd/PdNi(111) and 1.14eV for Pd/PdFe(111), respectively. For the hydrogenation into OOH process, the adsorption of OOH species are quite strong on both surfaces with the value of -0.78eV and -0.93eV for Pd/PdFe(111) and Pd/PdNi(111), respectively. The reaction is quite energetically favorable on both surfaces. The calculated energy barriers are quite acceptable for room temperature reaction (0.25eV for Pd/PdNi(111) and 0.41eV for Pd/PdFe(111)). The O-O distances for adsorbed O_2 and OOH species are listed in Table 6-5. The enlarged O-O distances for OOH are beneficial for the following ORR

steps to perform the breakdown of O-O bond, which is the symbol of direct-four electron transfer pathway.

Table 6-4. The calculated reaction barriers for direct O_2 dissociation and hydrogenation into OOH on Pd/PdFe(111), Pd/PdNi(111), Pd/PdCu(110) and Pd(111) surfaces.

	Barriers/eV			
	Pd/PdFe(111)	Pd/PdNi(111)	Pd/PdCu(110)	Pd(111)
O_2 direct dissociation	1.14	0.93	0.60	0.52 (Ref.[214])
Hydrogenation into OOH	0.41	0.25	-	-

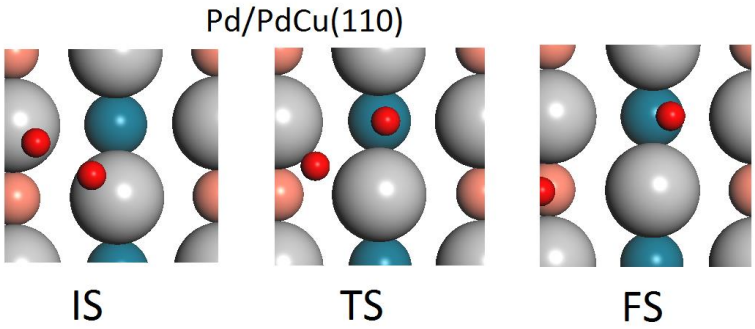

Figure 6-6. The top view of selected states along the path of O_2 dissociation for intermetallic Pd-Cu Pd/PdCu(110).

Table 6-5. The calculated O-O distance ($d_{O\text{-}O}$) on Pd/PdFe(111), Pd/PdNi(111), Pd/PdCu(110) and Pd(111) surfaces.

	$d_{O\text{-}O}$ / Å			
	Pd/PdFe(111)	Pd/PdNi(111)	Pd/PdCu(110)	Pd(111)
O_2	1.27	1.34	1.34	0.91
OOH	1.46	1.44	1.43	1.52

6.3.3 Pathways of ORR on Pd Monolayer on Pd-based Intermetallic Alloy

Next, the possible pathways of ORR are studied in detail. Generally, the desired cathode reaction is processed as follows: the adsorbed oxygen will react with H^+ species into H_2O.[215]

$$\frac{1}{2}O_2 + 2(H^+ + e^-) \rightarrow H_2O \qquad (6.1)$$

For reaction on Pd/PdCu(110) surfaces, the possible reaction pathways are shown below:

$$O_2 + * \rightarrow 2O^* \qquad (6.2)$$

$$2O^* + (H^+ + e^-) \rightarrow OH^* + O^* \qquad (6.3)$$

$$OH^* + O^* + (H^+ + e^-) \rightarrow 2OH^* \qquad (6.4a)$$

$$OH^* + O^* + (H^+ + e^-) \rightarrow O^* + H_2O \qquad (6.4b)$$

$$2OH^* + (H^+ + e^-) \rightarrow OH^* + H_2O \qquad (6.5a)$$

$$O^* + H_2O + (H^+ + e^-) \rightarrow OH^* + H_2O \qquad (6.5b)$$

$$OH^* + H_2O + (H^+ + e^-) \rightarrow 2H_2O \qquad (6.6)$$

where * denotes a surface vacant site, pathway *6.4a* and *6.4b* correspond to two possible reactions, the following reaction is *6.5a* and *6.5b,* respectively. For reaction on Pd/PdFe(111) and Pd/PdNi(111) surfaces, the possible reaction pathways are shown below:

$$O_2 + * \rightarrow O_2^* \quad (6.7)$$

$$O_2^* + (H^+ + e^-) \rightarrow OOH^* \quad (6.8)$$

$$OOH^* + (H^+ + e^-) \rightarrow 2OH^* \quad (6.9a)$$

$$OOH^* + (H^+ + e^-) \rightarrow O^* + H_2O \quad (6.9b)$$

$$2OH^* + (H^+ + e^-) \rightarrow OH^* + H_2O \quad (6.10a)$$

$$O^* + H_2O + (H^+ + e^-) \rightarrow OH^* + H_2O \quad (6.10b)$$

$$OH^* + H_2O + (H^+ + e^-) \rightarrow 2H_2O \quad (6.11)$$

where * denotes a surface vacant site, pathway *6.9a* and *6.9b* correspond to two possible reactions, the following reaction is *6.10a* and *6.10b,* respectively. We have calculated the reaction energy for all possible steps and plotted the reaction diagram shown in Figure 6-7. From the reaction energy, we can see that for Pd/PdNi(111), O^* + H_2O (-3.49eV) is more favorable than OH + OH formation (-3.28eV); while for Pd/PdFe(111), OH + OH formation (-3.24eV) is more favorable than O^* + H_2O (-2.79eV). For Pd/PdCu(110), the reaction energy for OH + OH formation has the same value as that of O + H_2O.

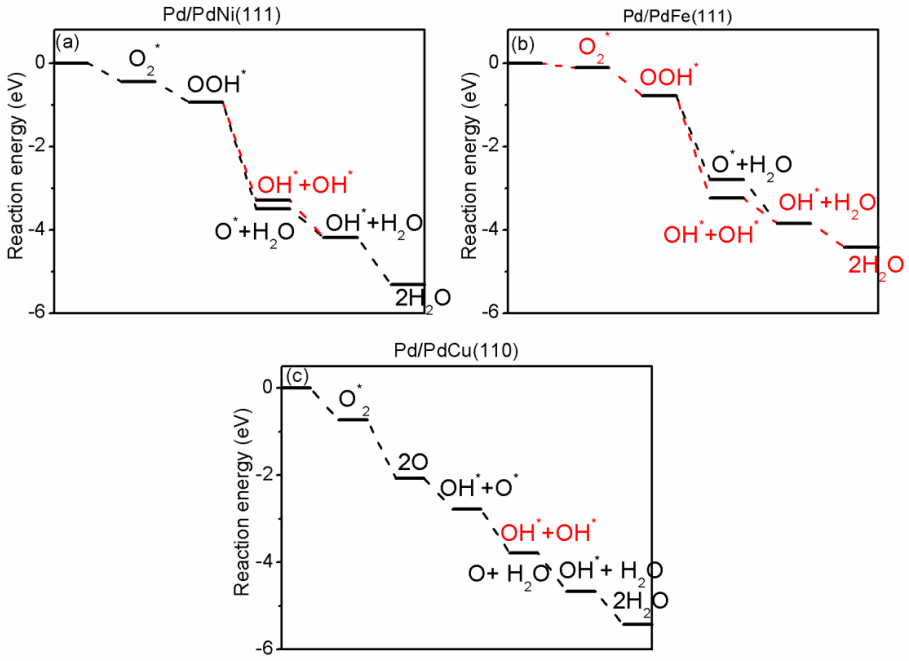

Figure 6-7. The calculated energy diagram for (a) Pd/PdNi(111), (b) Pd/PdFe(111), and (c) Pd/PdCu(110). The reaction for OOH and H can lead to two possible pathways as highlighted in red and black color.

We have then calculated the free energies of the intermediates (ΔG)[215] on both surfaces by the formula $\Delta G = \Delta E + \Delta G_U + \Delta ZPE - T\Delta S$, where ΔE is the reaction energies from DFT calculations of adsorbed reactants or intermediates, ΔG_U (equal to -eU, U represents electrode potential) is the relevant bias effect due to electron and proton transfer, ΔZPE and ΔS are the zero point energy difference and the entropy difference between the adsorbed state and the gas phase, respectively, and T is the system temperature (T = 298.15K for this work). We have set the *pH* value to be zero. At a *pH* different from zero, we can correct the free energy by adding the free energy contributions due to variations in H^+ concentration ΔG_{pH}. The chemical potential of a

proton/electron ($H^+ + e^-$) is equal to half of that of a gas-phase H_2. The Gibbs free energy diagram is shown in Figure 6-8. Here, for Pd/PdCu(110), we have simplified the ORR as $\frac{1}{2}O_2 + 2(H^+ + e^-) \rightarrow H_2O$.

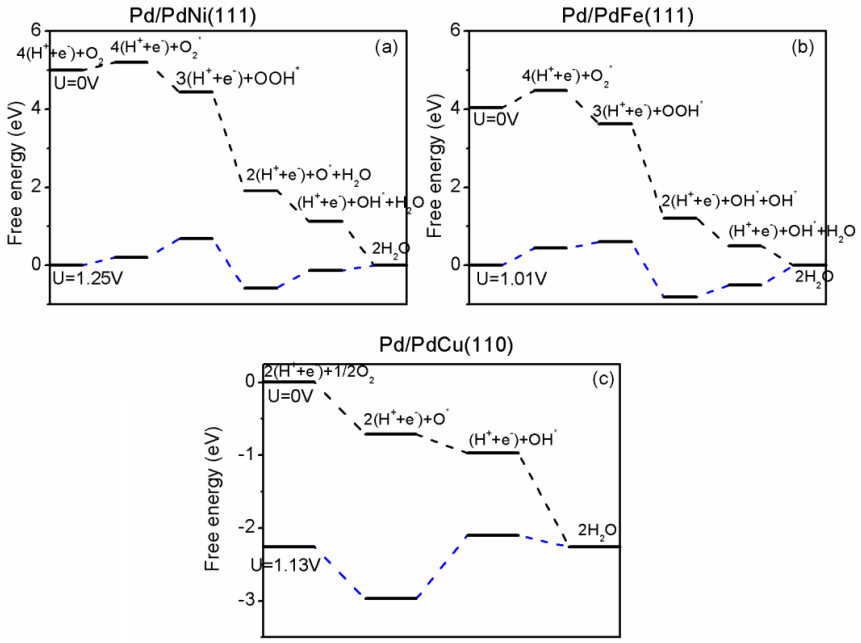

Figure 6-8. The calculated free energy diagram for (a) Pd/PdNi(111), (b) Pd/PdFe(111), and (c) Pd/PdCu(110).

Next, we will check stability of intermetallic alloy by estimating the dissolution potential[205, 216] using the following equation:

$$ne(U - U_{Pd}^0) = E_{Pd,bulk} - \frac{E_{skin} - E_{noskin}}{N_{surf}} \qquad (2)$$

where $U_{Pd}^0$is the dissolution potential for bulk Pd (equal to 0.95eV), $E_{Pd,bulk}$ equals to the total energy per atom for bulk Pd, E_{skin} and E_{noskin} are the total energy of

intermetallic alloy with and without Pd monolayer, N_{surf} is the number of the surface Pd atoms per supercell (equal to 8 in this work), and ne has the value of 2 for Pd. The calculated dissolution potential for Pd/PdNi(111), Pd/PdFe(111) and Pd/PdCu(110) are 0.98eV, 1.09eV, and 0.92eV, respectively. These calculated dissolution potentials are compatible with that of Pd. This indicates that the proposed Pd monolayer structures are stable under operating conditions. For reference, we have shown the calculated dissolution potential of Pt and Pt alloy from previous papers in Figure 6-9. Pure Pt has the dissolution potential in the range of 0.64eV to slightly below 1eV for the nanoparticle size ranging from 1nm to bulk Pt. Since we know that the surface activity can be modulated by both compression strain and substrate electron transfer, it is essential to understand the origin behind the difference among the Pd monolayer structure studied here. We can see that the ORR species and intermediates have increasing binding strength in the following order: Pd/PdFe(111) < Pd/PdNi(111) < Pd/PdCu(110) < Pd(111). However, according to the Sabatier principle[95], the best catalyst is a compromise having adsorbate-surface interactions of intermediate strength. Thus the enhanced activity can be explained by that pure Pd has experienced strong adsorption strength and these monolayer Pd structures with intermetallic alloy core have moderate adsorption energies. Additionally, Pd/PdFe(111) has the least binding strength and Pd/PdCu(110) has the strongest binding strength.

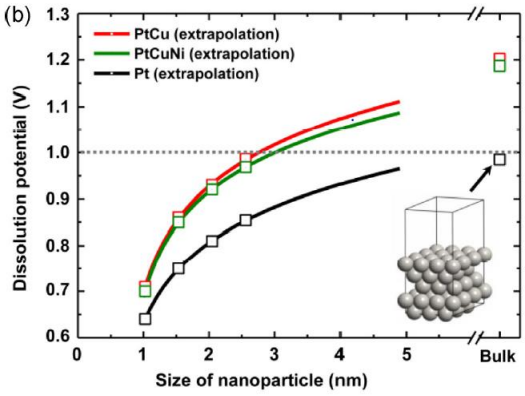

Figure 6-9. The dissolution potentials as a function of the size of nanoparticle of Pt, PtCu and PtCuNi and their extrapolations into larger particles. (Reprinted with permission from Ref.[217])

6.4 Summary

With first principle calculations, we have investigated the possibility of Pd monolayer structure on top of intermetallic alloy *bcc*-PdCu(110) and *fct*-PdM(111) (M=Fe, Ni) for the application of cathode materials. Pd-monolayer on top of *fct*-PdM(111) substrate is found to have shorter Pd-Pd bond length than that of bulk Pd. The DOS analysis confirms the negative shift of *d*-band center for various Pd monolayer structures compared with that of Pd(111). The charge analysis reveals that Pd-monolayer can obtain electron from PdNi(111) substrate and PdCu(110) but donate electron to PdFe(111) substrate. After adsorbed on surfaces, O_2 is found to undergo hydrogenation process into OOH species instead of direct dissociation on Pd/PdM(111) surfaces while it shows different trend on Pd/PdCu(110) surface, which

prefers direct dissociation mechanism. For all these structures, the breakdown of O-O bond indicates that four-electron pathway is performed, which is a desired pathway to ensure high efficiency. The enhanced activity for Pd monolayer structures is ascribed to moderate adsorption strength for ORR intermediates due to compression strain and substrate electron transfer. When considering the operating condition, the dissolution potential analysis indicates that Pd/PdCu(110), Pd/PdNi(111) and Pd/PdFe(111) are stable. We hope our calculations can boost the exploration of intermetallic alloy catalyst.

Chapter 7 DFT Study on Pt-Cu Single Atom Alloy for Hydrogenation

In this Chapter, we will present our work on Pt-Cu single atom alloy for the application of hydrogenation catalyst. Single atom alloy has been proposed and researched enormously in the last ten years. The stability, durability, and activity are three major concerns. The atomic structure of Pt atoms doped on Cu is studied in detail. The following H_2 activation ability is discussed to evaluate the performance.

7.1 Overview

The idea of single-atom catalyst has been proposed for years.[54, 218-219] However, due to experimental techniques, the preparation and characterization of stable and functional single-atom catalyst are full of challenge.[220-226] Single-atom catalyst has attracted much attention due to the high utilization of active site. Meanwhile, the selectivity can be enhanced due to the dispersion of active site.[64] One representative form of single-atom catalyst is the single atom alloy (SAA), which usually involves two different metal elements.[227-229] For bimetallic alloy, the ensemble effect and ligand effect govern the catalytic performance.[91] The ensemble of atoms forming the active sites varies for different reactions. For example, two adjacent Pd atoms are needed for CO oxidation on PdAu(100) surface[230]; while isolated Pt atom on $Cu_3Pt(111)$ is required for facile H_2 dissociation[231]. Another benefit for single atom alloy is that some bimetallic catalysts with multiple binding sites can overcome the Brønsted-Evans-Polanyi relationship. Thus, these bimetallic catalysts can exhibit weak

adsorption energy and low activation energy at the same time. Pt-Cu bimetallic alloy are widely used in heterogeneous catalysis as hydrogenation catalyst.[74, 232-233] Experimental evidences have indicated that Pt atoms prefer to form isolated active site on Cu(111) surface.[234-235] These highly dispersive atomic structure show facile H_2 dissociation ability and atomic H is easy to migrate to nearby Cu site. In this work, the possible atomic structure of Pt-Cu single atom alloy is built and calculated. The stability and corresponding H_2 dissociation ability are two representative criterions for the evaluation of proposed Pt-Cu single atom alloy. Both slab model and nanocluster model are used for the calculations.

7.2 Computational Methods

7.2.1 Pt-Cu Single Atom Alloy Structure

Two models including slab model and nanocluster model are used to simulate Pt-Cu single atom alloy. For the slab model, a five-layer (3×3) supercell was used. The vacuum region was up to 15Å for all structures. In order to study the atomic surface structure of Pt-Cu, we have substituted one to four copper atoms with platinum atoms. Within the same Pt dopant concentration, the effect of dopant sites is studied to analyze the possibility of forming Pt island or isolated Pt atoms. In addition, both surface alloy and subsurface alloy are considered. The *k*-point mesh[164] of 3×3×1 was for these models and the bottom two layers were fixed with the value of bulk Cu in the structural relaxation. We use Pt_N/Cu(111) to represent the slab model, where N is the

number of Cu atoms substituted by Pt. For the nanocluster model, we have built icosahedral clusters with 55-atom and 147-atom. It is known that the surface of icosahedral cluster is enclosed by {111} facet, which is comparable with slab model along [111] direction. A three-dimensional periodic cube supercell with dimension to be 25Å for 55-atom cluster (30Å for 147-atom cluster) was used in the calculation. We use Pt_N/Cu_{55} to represent 55-atom cluster model and Pt_N/Cu_{147} to represent 147-atom cluster model, where N is the number of Cu atoms substituted by Pt. The *k*-point mesh of 1×1×1 was used for all cluster models.

7.2.2 DFT Calculations

All the calculations were performed on the basis of spin-polarized DFT with projector augmented wave formalism, as implemented in the VASP 5.3.3 code. [123, 165] The generalized gradient approximation with the parameterization of Predew-Burke-Ernzerhof was used for the exchange-correlation functional.[118, 166] A kinetic energy cutoff of 400eV for the plane wave expansion with proper k-point spacing using Monkhorst-Pack grid method[164] was found to be sufficient to ensure that the total energy was converged at 1meV/atom level. The convergence criterion for the self-consistence field energy was set to be 10^{-4}eV.

7.3 Discussions

7.3.1 Geometry of Pt-Cu Single Atom Alloy

We have first studied the geometry of Pt-Cu single atom alloy using slab model. For single Pt atom, two possible sites including surface substitution and subsurface substitution are considered. Then we added the Pt atom one by one with up to at most three Pt atoms in the system. The additional Pt atom can occupy surface or subsurface sites. The configurations of these possible structures are shown in Figure 7-1. The surface site can form island or be isolated. The stability of all possible structures are listed in Table 7-1, which is calculated by the formula shown below:

$$E_{stability} = E_{Pt_N/Cu(111)} - E_{Cu(111)} - N(E_{Pt} - E_{Cu}) \qquad (7.1)$$

where $E_{Pt_N/Cu(111)}$ and $E_{Cu(111)}$ represents the total energy for Pt_N/Cu(111) and pure Cu(111), respectively. E_{Pt} (or E_{Cu}) is the bulk energy per atom of Pt (or Cu). A negative value corresponds to stable alloy. From Table 7-1, it is clear to see that for single Pt dopant, Pt surface substitution (-0.70eV) is more stable than subsurface substitution (-0.50eV). After adding Pt atoms one by one, the stability of possible structures are studied in detail. Especially, for Pt_2/Cu(111), isolated structure (-0.70eV) is more stable than dimmer structure (-0.65eV); and for Pt_3/Cu(111), isolated structure (-0.67eV) is more stable than trimmer structure (-0.59eV). This indicates that Pt atoms tend to form isolated structure on surface, which is also witnessed experimentally.[232] The STM images of Pt-Cu alloys formed by deposition of Pt at Cu(111) surface is shown in Figure 7-2.

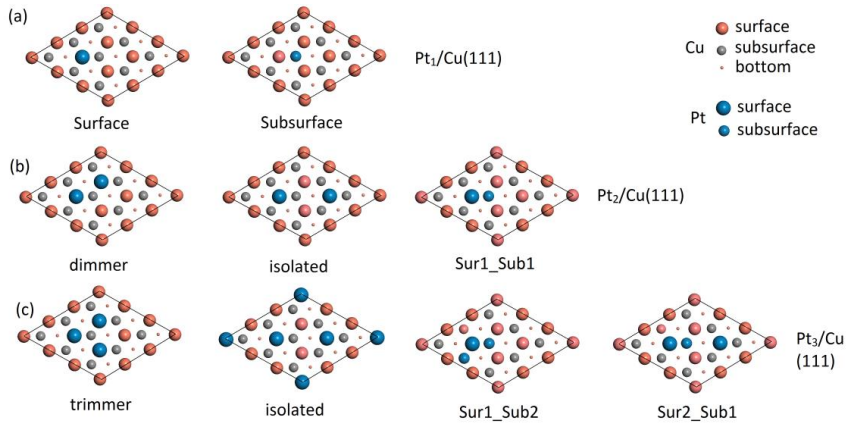

Figure 7-1. The configurations of top view of various $Pt_N/Cu(111)$ structures including (a) $Pt_1/Cu(111)$, (b) $Pt_2/Cu(111)$, and (c) $Pt_3/Cu(111)$. The doped Pt can be located at surface site or subsurface site or both sites.

Table 7-1. The calculated stability of proposed Pt-Cu single atom alloy. sur1_sub1 is for the structure with one Pt atom occupies surface site and one Pt atom occupies subsurface site. This definition also applies to sur1_sub2 and sur2_sub1. Isolated is for the structure with Pt atoms dispersedly located on surface; dimmer and trimmer are for the structures with Pt atoms forming island structure. See Figure 7-1 for illustration.

Stability/eV					
Pt_1/Cu			Pt_3/Cu		
	surface	-0.70		trimmer	-0.59
	subsurface	-0.50		isolated	-0.67
Pt_2/Cu				sur1_sub2	-0.42
	dimmer	-0.65		sur2_sub1	-0.58
	isolated	-0.70			
	sur1_sub1	-0.52			

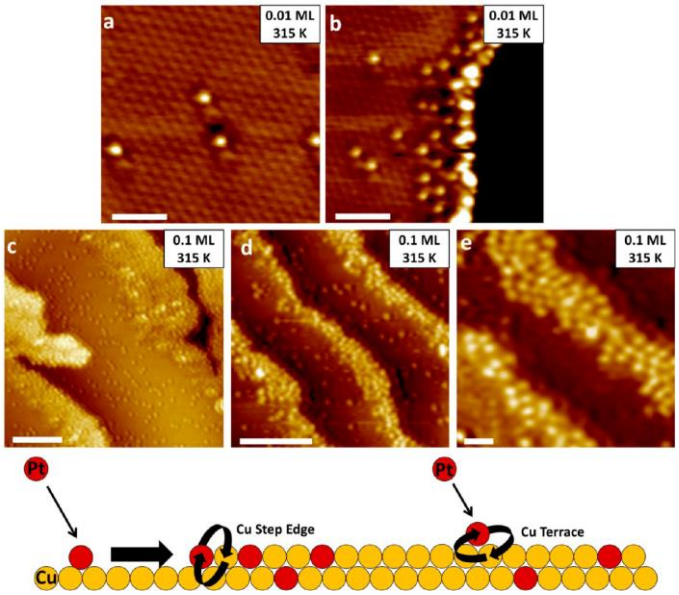

Figure 7-2. The STM images of Pt-Cu alloys formed by deposition of Pt on Cu(111) at 315K. (Reprinted with permission from Ref. [232])

Then we have studied the stability of icosahedral nanocluster model. For surface substitution, two types of Cu atoms including Cu_top and Cu_edge are considered. We have added the Pt atom one by one with up to at most two Pt atoms. The configurations of these models of Pt_N/Cu_{55} icosahedral nanoclsuter (diameter of 1nm) and Pt_N/Cu_{147} icosahedral nanocluster (diameter of 1.5nm) are shown in Figure 7-3. The stability of all possible structures is listed in Table 7-2, which is calculated by the formula shown below:

$$E_{stability} = E_{Pt_N/Cu_{55}} - N \times \frac{E_{Pt_{55}}}{55} - (55 - N) \times \frac{E_{Cu_{55}}}{55} \qquad (7.2)$$

$$E_{stability} = E_{Pt_N/Cu_{147}} - N \times \frac{E_{Pt_{147}}}{147} - (147 - N) \times \frac{E_{Cu_{147}}}{147} \qquad (7.3)$$

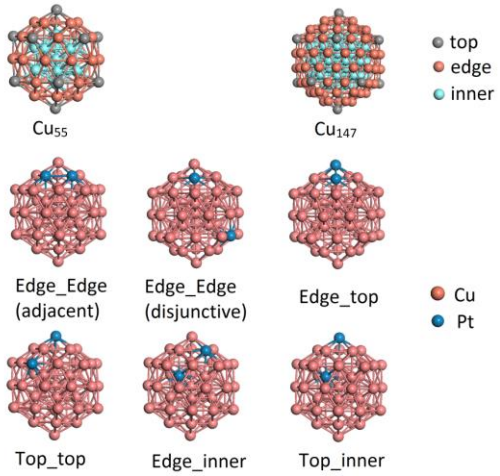

Figure 7-3. The configurations various Pt_N/Cu_{55} and Cu_{147} nanocluster. The doped Pt can be either located at outmost shell site or inner site or both.

where $E_{Pt_N/Cu_{55}}$, $E_{Pt_{55}}$ and $E_{Cu_{55}}$ are the calculated total energy for Pt doped Cu icosahedral nanocluster, Pt icosahedral nanocluster and Cu icosahedral nanocluster, respectively. Again, it is clear to see that Pt tends to occupy outmost shell site (surface) instead of core site (inner). For the outmost shell site, the edge site is more stable than top site. And this is not affected by increasing the size of nanocluster. Especially, for icosahedral Pt_1/Cu_{55}, the calculated stability is -0.68eV for edge site substitution and -0.62eV for top site substitution, respectively; For 147-atom nanocluster, the calculated stability are -0.89eV for edge site substitution and -0.76eV for top site substitution, respectively. When adding an additional Pt atom into the nanocluster, the added Pt atom tends to occupy the surface disjunctive edge site (-

1.42eV for Pt_2/Cu_{55} and -1.69eV for Pt_2/Cu_{147}, see Figure 7-3 for illustration) instead of surface adjacent edge site (-1.15eV for Pt_2/Cu_{55} and -1.52 for Pt_2/Cu_{147}, see Figure 7-3 for illustration). This is similar to the slab model that Pt atoms prefer to occupy surface isolated sites rather than form dimmer or trimmer.

Table 7-2 The calculated stability of proposed Pt-Cu icosahedral nanocluster. For single Pt substitution, edge, top and inner sites represent surface edge site, surface top site and core inner site, respectively (see Figure 7-3 for illustration). After adding one more Pt atoms, the new Pt atom can be located at surface (edge/top) or core (inner) sites. Adjacent and disjunctive in the bracket means two Pt atoms are connected or separated each other. See Figure 7-3 for illustration.

Stability/eV			
	Pt_1/Cu_{55}		Pt_1/Cu_{147}
Edge	-0.68		-0.89
Top	-0.62		-0.76
Inner	-0.21		-0.53
	Pt_2/Cu_{55}		Pt_2/Cu_{147}
Edge_Edge (adjacent)	-1.15		-1.52
Edge_Edge (disjunctive)	-1.42		-1.69
Edge_Top	-1.16		-1.52
Top_Top	-1.30		-1.46
Edge_Inner	-0.83		-1.49
Top_Inner	-0.71		-1.27

7.3.2 H_2 Dissociation on Pt-Cu Single Atom Alloy with Surface (or Outmost Shell) Substitution

Since Pt atoms tend to occupy surface (or outmost shell) site instead of subsurface (or inner) site, we have first studied H_2 dissociation on Pt-Cu single atom alloy with surface substitution. It is known that H_2 can dissociate freely upon adsorbed on Pt surface.[192] This facile H_2 dissociation is a desirable process for the following hydrogenation process. For slab model, we have calculated the adsorption energies of H_2 adsorbed on various Pt_N/Cu(111) surfaces and listed the results in Table 7-3. Noted that the active site is Pt, so H_2 molecular is initially placed at *top* site of Pt atom and fully relaxed during the calculations. For single Pt atom, H_2 is found to be dissociated after relaxing. This indicates that H_2 can be easily activated on Pt_1/Cu(111) with surface substitution. After adding additional Pt atom on surface, for dimmer structure, H_2 is found to dissociate easily to two atomic H with distance to be 2.71Å; while for isolated structure, H_2 is found to be adsorbed on Pt *top* site with enlarged H-H distance (0.94Å). The top view of Pt_2/Cu(111) with H_2 adsorption (surface isolated or dimmer) is shown in Figure 7-4. Initially, the H-H bond length for molecular H_2 is 0.75Å. For isolated Pt sites, after adsorbed on Pt sites, these enlarged H-H distance (0.94Å) indicates that H_2 is partially activated. For Pt_3/Cu(111) case, for both trimmer and isolated structure, H_2 is found to be adsorbed on Pt *top* site with enlarged H-H distance (0.92Å for isolated structure and 0.90Å for trimmer structure). The results show that

H_2 cannot be fully activated on most of Pt_N/Cu(111) surfaces. We have also studied the effect of surface H_2 coverage on adsorption energies. It is found that the adsorption energies (per H_2) show dramatically decrease when increasing H_2 concentration. This indicates that H_2 dissociation process on the proposed Pt_N/Cu(111) structures with Pt located at surface cannot achieve facile H_2 dissociation.

Table 7-3 The calculated adsorption energies of H_2 with respect to different Pt dopant sites and surface H_2 coverage. Noted that all possible Pt sites are located in surface sites (see Figure 7-1 for illustration).

Adsorption energy (per H_2) E_{ad}/eV					
		H_2 surface coverage			
		1/9 ML	2/9 ML	3/9 ML	4/9 ML
Pt_1/Cu(111)					
	Isolated	-0.70	-0.30	-0.17	-0.15
Pt_2/Cu(111)					
	Isolated	-0.15	-0.46	-0.20	-0.16
	Dimmer	-0.64	-0.21	-0.23	-0.20
Pt_3/Cu(111)					
	Isolated	-0.06	-0.09	-0.05	-0.03
	Trimmer	-0.02	0.075	0.11	0.001

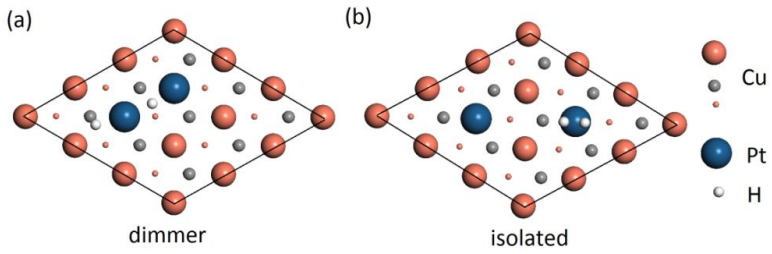

Figure 7-4. The top view of H_2 adsorption on Pt_2/Cu(111) with (a) dimmer structure, and (b) isolated structure.

We have then investigated the H_2 dissociation ability for nanocluster case. Noted that all the H_2 adsorption calculations are done with 55-atom icosahedral cluster model. Since Pt atoms tend to occupy outmost shell site instead of inner site, we have first studied H_2 dissociation on nanocluster with all possible Pt sites in outmost shell. For single Pt atom dopant, H_2 is found to be dissociated on surface *edge* site after relaxing, while adsorbed on surface *top* site with enlarged H-H bond distance (0.90Å). This indicates that surface *edge* site is more effective for H_2 dissociation than surface *top* site. When adding an additional Pt atom, two Pt atoms occupy adjacent edge site (-1.29eV, H-H distance 2.84Å) has stronger adsorption strength than that of two Pt atoms occupy disjunctive edge site (-0.74eV, H-H distance 2.20Å). This is similar to the case with slab model that dimmer structure is more effective for H_2 dissociation than isolated structure. It is interesting to see that for both slab model and nanocluster model, the most stable configurations do not always correspond to the most effective for H_2 dissociation. This is also witnessed by previous calculations on Pd-doped

Cu(111) single atom alloy that the most stable configurations may not be the structure with the lowest dissociation barrier values.[236]

Table 7-4 The calculated adsorption energies of H_2 with respect to different Pt dopant sites and surface H_2 coverage. Noted that all possible Pt sites are in outmost shell (see Figure 7-3 for illustration).

Adsorption energy (per H_2) E_{ad}/eV			
		H_2 surface coverage	
		1/9 ML	2/9 ML
Pt_1/Cu_{55}			
	Edge	-0.80	-0.47
	Top	-0.39	-0.18
Pt_2/Cu_{55}			
	Edge_Edge (adjacent)	-1.29	-0.85
	Edge_Edge (disjunct)	-0.74	-0.60
	Edge_Top	-0.84 (edge site) -0.65 (top site)	-0.75
	Top_Top	-0.39	-0.38

7.3.3 Effect of Subsurface (or Inner) Pt Dopant on H_2 Dissociation

Fu *et al.*[55] have indicated that the catalytic activity of surface Pd atoms can be improved with subsurface Pd atoms dopant. Thus the effect of Pt subsurface (or inner) doping on H_2 dissociation is studied to see whether this is the case for Pt alloy. For

surface substitution, most of the structures of Pt_2/Cu(111) and Pt_3/Cu(111) cannot perform facile H_2 dissociation. We have added additional Pt atoms located at subsurface (see Figure 7-1 for illustration) and calculated the corresponding H_2 adoption energies. The results are listed in Table 7-5. It is noted that subsurface Pt

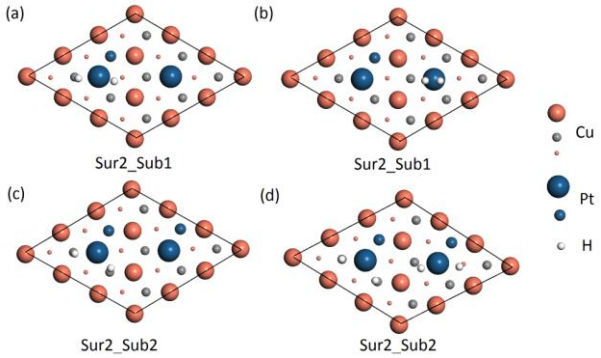

Figure 7-5. The top view of H_2 adsorption on Pt_3/Cu(111) and Pt_4/Cu(111) for adsorption site on (a) Sur2_Sub1 (with subsurface dopant), and (b) Sur2_Sub1 (without subsurface dopant); H_2 adsorption coverage with (c) 1/9ML, and (d) 1/9 ML on Sur2_Sub2.

atom alone is not effective for H_2 dissociation due to weak adsorption energy (0.07eV). For isolated structure (Pt_2/Cu(111) isolated, see Figure 7-4(b) for illustration), after adding one subsurface Pt atom (Pt_3/Cu(111) Sur2_Sub1, see Figure 7-5(a) for illustration), the adsorption energy has been increased from -0.15eV to -0.49eV if H_2 is adsorbed on Pt site with subsurface dopant. The H-H distance has been increased from 0.90Å to 2.24Å. This indicates that with the help of subsurface Pt atom, H_2 can be easily activated upon adsorbed on Pt site. However, if H_2 is adsorbed

on Pt site without subsurface dopant (see Figure 7-5(b) for illustration), the calculated adsorption energy is only -0.08eV with H-H distance 0.93Å. If we continue adding one more Pt atom, the resulting structure is Pt_4/Cu(111) Sur2_Sub2. This structure is found to be effective for H_2 dissociation with increasing H_2 coverage as shown in Figure 7-5(c)-(d). This indicates that surface depressively distributed single Pt atom with subsurface dopant can serve as multi-active sites.

Table 7-5 The calculated adsorption energies of H_2 with respect to different Pt dopant sites and surface H_2 coverage with the effect of subsurface Pt dopant. For case Sub2_Sub1, "with subsurface" stands for H_2 adsorbed on Pt atom with subsurface Pt substitution, "without subsurface" is for H_2 adsorbed on Pt atom without subsurface Pt substitution. See Figure 7-5(a)-(b) for illustration.

Adsorption energy (per H_2) E_{ad}/eV					
		H_2 surface coverage			
		1/9 ML	2/9 ML	3/9 ML	4/9 ML
Pt_1/Cu(111)					
	Subsurface	0.07	-	-	-
Pt_3/Cu(111)					
	Sur1_Sub2	-0.64	-0.31	-0.22	-0.12
	Sur2_Sub1	-0.49(with subsurface)	-0.53	-0.18	-0.15
		-0.08(without subsurface)	-	-	-
Pt_4/Cu(111)					
	Sur1_Sub3	-0.69	-0.30	-0.19	-0.15
	Sur2_Sub2	-0.58	-0.61	-0.35	-0.23

Next, we have considered the cluster model with an additional Pt atom located at inner site. The results are shown in Table 7-6. It is noted that for top site, the additional inner atom can significantly change the adsorption energies and H_2 is found to be dissociated on these top sites. For example, for top_inner structure, the adsorption energy has been increased from -0.39eV to -0.66eV. The H-H distance has been increased from 0.90Å to 1.95Å. It is found that with subsurface (or inner) substitution, the catalytic for H_2 dissociation can be improved for both slab model and nanocluster model

.

Table 7-6 The calculated adsorption energies of H_2 with respect to different Pt dopant sites and surface H_2 coverage with Pt inner site with the effect of inner Pt dopant.

Adsorption energy (per H_2) E_{ad}/eV			
		H_2 surface coverage	
		1/9 ML	2/9 ML
Pt_2/Cu_{55}			
	Edge_Inner	-0.94	-0.55
	Top_Inner	-0.66	-0.37
Pt_3/Cu_{55}			
	Edge_Edge_Inner (adjacent)	-1.01	-1.09
	Edge_Edge_Inner (disjunct)	-0.84	-0.83
	Edge_Top_Inner	-0.94(edge site) -0.58(top site)	-0.93
	Top_Top_Inner	-0.66	-0.49

7.4 Summary

The possible structures of Pt-Cu single atom alloy are studied in detail with both slab model and nanocluster model. It is found that single Pt atom prefers surface (slab model) or outmost shell (nanocluster) sites instead of subsurface or core sites. When adding Pt atoms one by one, the additional Pt atoms tends to occupy surface sites to form isolated structure or outmost shell sites to form adjunctive structure. For nanocluster model, outmost shell has two possible sites: edge site and top site. Pt substitution edge site is more stable than top site substitution. The H_2 adsorption energies is selected as a criterion for evaluating the catalytic ability of facile H_2 dissociation. For both slab model and nanocluster model, it is noted that the most stable configurations do not always correspond to the most effective structure for H_2 dissociation. Additionally, with the help of subsurface Pt substitution (slab model) or inner Pt substitution (nanocluster), the ability for dissociation of H_2 is improved and surface isolated Pt atoms can serve as multi-active sites for H_2 dissociation.

Chapter 8 Conclusion and Recommendations

In this Chapter, we will summarize our work and list the suggestions for future work. This thesis is focused on the manipulation of catalytic activity of noble metals (palladium and platinum) by alloying with non-precious metals. This thesis contains three parts: firstly, we have studied the overlayer model of Pd-Cu and Pt-Cu bimetal alloy and investigated on the catalytic activity for CO oxidation and H_2 dissociation, respectively; secondly, we have studied the Pd monolayer model of Pd monolayer supported on Pd-M (M=Cu, Fe, Ni) intermetallic alloy and investigated the catalytic activity for oxygen reduction reaction; thirdly, we have studied the single atom alloy model of dispersedly distributed Pt atoms doped on Cu and investigated the catalytic activity for hydrogenation.

The major contributions are summarized as (1) the discovery of the scaling relations for predicting catalytic activity of CO oxidation catalyst, and (2) the computational study of the catalytic mechanism for CO oxidation, H_2 dissociation, and ORR.

8.1 Conclusion

8.1.1 Overlayer Model of Pd-Cu and Pt-Cu Bimetal Alloy

The proposed overlayer model consists of noble metal overlayer (up to three-layer at most) and substrate (fixed three-layer). We have verified that three-layer Cu layer is enough and accurate to simulate the Pd-Cu (or Pt-Cu) bimetal alloy by comparing the results with those of 7-layer Cu(111) slab model where the surface Cu atoms are

replaced by Pd (or Pt) atoms layer by layer. By alloying, the *d*-band center of surface Pd (or Pt) atom is found to shift away from the Fermi level, resulting weaker adsorption strength. This shift trend is found to be modulated by both the number of noble metal overlayer (single, double or triple) and substrate Cu charge transfer, which increases in the following order: 2L-Pd/Cu(111) < 3L-Pd/Cu(111) < 1L-Pd/Cu(111) < Pd(111) (Pt-Cu shares the same trend). This disorder phenomenon is explained by the contribution of localized electronic states near the Fermi level. The stability is estimated by calculating the formation energy, where negative formation energy corresponds to stable structure. 2L-Pd/Cu(111) has a negative formation energy (-0.21eV), while that of 1L-Pd/Cu(111) (0.42eV) and 3L-Pd/Cu(111) (0.07eV) are positive. Similar results are found for NL-Pt/Cu(111). 2L-Pt/Cu(111) has a negative formation energy (-0.36eV), while that of 1L-Pt/Cu(111) (0.62eV) and 3L-Pt/Cu(111) (0.10eV) are positive.

Pd-Cu bimetal alloy is found to be effective for CO oxidation with low energy barriers. The adsorbed oxygen is found to go through CO-assisted dissociation on NL-Pd/Cu(111) surfaces by considering the coadsorption case of CO and O_2. The calculated barriers are found to show increasing trend with respect to *d*-band center for direct O_2 dissociation and decreasing trend with respect to *d*-band center for CO oxidation. The case of CO-assisted O_2 dissociation does not simply obey this rule. We have proved this opposite trend by deriving the relationship of energy barrier and

adsorption energy with Sabatier principle. Compared with pure noble metal such as Pd, Pt or Au, the proposed 2L-Pd/Cu(111) has low CO-assisted O_2 dissociation barrier and low CO oxidation barrier. We hope our calculations can be useful for experimental works for designing oxidation catalyst.

Pt-Cu bimetal alloy is found to be effective for fuel cell anode catalyst. We have focused on 2L-Pt/Cu(111) due to good stability. Two criterions are selected to evaluate the catalytic ability: the CO-tolerance ability and H_2 dissociation ability. The CO-tolerance ability is estimated by calculating the CO saturation coverage. 2L-Pt/Cu(111) has much lower CO saturation coverage (40%) compared with that of Pt(111) (75%). The H_2 dissociation barriers with various CO and H_2 coverage are calculated and the results show that the dissociation barrier from H_2 to H becomes higher with increased CO and/or H_2 coverage. Under the saturation coverage (40%), the dissociation barrier for 2L-Pt/Cu(111) is less than 0.4eV. Especially, under the low coverage of CO, the dissociation barrier can be ignored. A mathematical model is applied to study the competition effect of CO and H_2 adsorption. The results show that at the same operating temperature, the surface H coverage on 2L-Pt/Cu(111) is dramatically increased compared with that of Pt(111). Pt/Ru is proposed by previous papers to be an efficient anode material.[192, 195] Our calculations show that the proposed 2L-Pt/Cu(111) has even lower barrier than Pt/Ru alloy. We hope our calculation can stimulate the exploration of catalysis of Pt/Cu bimetallic alloy.

8.1.2 Pd Monolayer Model of Pd Single-layer Supported on Pd-M (M=Cu, Fe, Ni) Intermetallic Alloy

The proposed Pd monolayer model consists of Pd monolayer and Pd-M (M=Cu, Fe, Ni) intermetallic alloy substrate. Due to phase transformation, the substrate has either *bcc* (PdCu) or *fct* (PdNi, PdFe) structure. The ratio of Pd and M is 50:50 for these ordered intermetallic alloy. We have evaluated the ORR ability with Gibbs free energy and dissolution potential analysis. O_2 is found to undergo direct dissociation mechanism on Pd/PdCu(110) but hydrogenation into OOH on Pd/PdM(111) (M=Ni, Fe). The adsorption energies of ORR species (O_2, OOH, OH) and intermediates increase in the following order: Pd/PdFe(111) < Pd/PdNi(111) < Pd/PdCu(110) < Pd(111). The enhanced activity for Pd monolayer structures is ascribed to moderate adsorption strength for ORR intermediates due to compression strain and substrate electron transfer. The dissolution potential analysis confirms that the proposed Pd-monolayer structures are stable under operating conditions.

8.1.3 Single Atom Alloy (SAA) Model of Pt/Cu(111)

Two models including slab model and nanocluster model have been adopted to simulate single atom alloy Pt/Cu(111). The formation energy (stability) is first addressed to study the structure of Pt/Cu(111). For single Pt atom substitution, the Pt atom tends to occupy surface site (slab model) or outmost shell site (nanocluster model). It is noted that, for outmost shell site, there are two different sites, *edge* site

and *top* site. Especially, the calculated stability is -0.68eV for *edge* site substitution and -0.62eV for *top* site substitution. This is not affected by increasing the size of nanocluster from 55-atom nanocluster to 147-atom nanocluster. When adding additional Pt atom, for slab model, surface isolated structure (-0.70eV) is more stable than surface dimmer structure (-0.65eV); for nanocluster model, the added Pt atom tends to occupy the surface disjunctive edge site (-1.42eV for Pt_2/Cu_{55} and -1.69eV for Pt_2/Cu_{147}). The H_2 adsorption energy is calculated to study the facile H_2 dissociation process. It is found that the most stable configurations do not always correspond to the most effective structure for H_2 dissociation. Additionally, with the help of subsurface Pt substitution (slab model) or inner Pt substitution (nanocluster), the ability for dissociation of H_2 is improved and surface isolated Pt atoms can serve as multi-active sites for H_2 dissociation.

8.2 Recommendations for Further Research

Current thesis is focused on the catalytic activity by calculating the adsorption energies and reaction barriers with the combination mathematical model or theoretical theory (such as *d*-band theory). There are more studies can be done for heterogeneous catalysis with computational tool. For example, the understanding of catalytic properties of single atom alloys from theoretical point of view and the corresponding computational design rule are still full of challenge.[237] Moreover, the scaling relationships[135] have been developed recently to study the catalytic trend with bond

order conservation principles. These scaling relationships expand the application of traditional Brønsted-Evans-Polanyi relation. Furthermore, for alloy structures, it is interesting to expand from bimetal alloy to ternary alloy. The Monte Carlo method can be applied to study the possible alloy structure.

Author's Publications

Journal publications related to this thesis

1. Liu, J.; Fan, X.; Sun, C. Q.; Zhu, W., DFT Study on bimetallic Pt/Cu (111) as efficient catalyst for H_2 dissociation. *Applied Surface Science* **2018**, 441, 23-28. (Chapter 5)

2. Liu, J.; Fan, X.; Sun, C. Q.; Zhu, W., DFT Study on Intermetallic Pd–Cu alloy with cover layer Pd as efficient catalyst for oxygen reduction reaction. *Materials* **2017**, 11 (1), 33. (Chapter 6)

3. Liu, J.; Fan, X.; Sun, C. Q.; Zhu, W., Layer effect on catalytic activity of Pd-Cu bimetal for CO oxidation. *Applied Catalysis A: General* **2017**, 538, 66-73. (Chapter 4)

4. Liu, J.; Sun, C.; Zhu, W., Origin of efficient oxygen reduction reaction on Pd monolayer supported on Pd-M (M=Ni, Fe, Fe) intermetallic alloy. *Electrochimica Acta* **2018**, 282, 680-686. (Chapter 6)

5. Liu, J.; Sun, C. Q.; Zhu, W., A comparative study on single atom alloy of Pt doped Cu flat surface and nanoclsuter. In preparasion. (Chapter 7)

Journal publications related to other projects

6. Liu, J.; Fan, X.; Sun, C.; Zhu, W., Transparent conductivity modulation of ZnO by group-IVA doping. *Chemical Physics Letters* **2016**, 649, 78-83.

7. Liu, J.; Fan, X.; Sun, C.; Zhu, W., Oxidation of the titanium (0001) surface: diffusion processes of oxygen from DFT. *RSC Advances* **2016**, 6 (75), 71311-71318.

Bibliography

1. Dulub, O.; Hebenstreit, W.; Diebold, U., Imaging cluster surfaces with atomic resolution: the strong metal-support interaction state of Pt supported on TiO 2 (110). *Physical Review Letters* **2000,** *84* (16), 3646.

2. Liu, Z. P.; Hu, P.; Alavi, A., Catalytic role of gold in gold-based catalysts: a density functional theory study on the CO oxidation on gold. *J Am Chem Soc* **2002,** *124* (49), 14770-9.

3. Wahlström, E.; Lopez, N.; Schaub, R.; Thostrup, P.; Rønnau, A.; Africh, C.; Lægsgaard, E.; Nørskov, J. K.; Besenbacher, F., Bonding of Gold Nanoclusters to Oxygen Vacancies on Rutile TiO2(110). *Physical review letters* **2003,** *90* (2), 026101.

4. Gong, X. Q.; Liu, Z. P.; Raval, R.; Hu, P., A systematic study of CO oxidation on metals and metal oxides: density functional theory calculations. *J Am Chem Soc* **2004,** *126* (1), 8-9.

5. Sa, J.; Bernardi, J.; Anderson, J. A., Imaging of low temperature induced SMSI on Pd/TiO2 catalysts. *Catal Lett* **2007,** *114* (1-2), 91-95.

6. Han, Y.; Zhang, M.; Li, W.; Zhang, J., Effect of TiO 2 support on the structural and electronic properties of Pd m Ag n clusters: a first-principles study. *Physical Chemistry Chemical Physics* **2012,** *14* (24), 8683-8692.

7. Yu, S.; Yun, H. J.; Lee, D. M.; Yi, J., Preparation and characterization of Fe-doped TiO 2 nanoparticles as a support for a high performance CO oxidation catalyst. *Journal of Materials Chemistry* **2012,** *22* (25), 12629-12635.

8. Wang, Y.-G.; Yoon, Y.; Glezakou, V.-A.; Li, J.; Rousseau, R., The role of reducible oxide–metal cluster charge transfer in catalytic processes: new insights on the catalytic mechanism of CO oxidation on Au/TiO2 from ab initio molecular dynamics. *Journal of the American Chemical Society* **2013,** *135* (29), 10673-10683.

9. Yuan, Z.; Li, X.-N.; He, S.-G., CO oxidation promoted by gold atoms loosely attached in AuFeO3–cluster anions. *The journal of physical chemistry letters* **2014,** *5* (9), 1585-1590.

10. Toda, T.; Igarashi, H.; Watanabe, M., Enhancement of the electrocatalytic O-2 reduction on Pt-Fe alloys. *Journal of Electroanalytical Chemistry* **1999,** *460* (1-2), 258-262.

11. Greeley, J.; Mavrikakis, M., Alloy catalysts designed from first principles. *Nature materials* **2004,** *3* (11), 810.

12. Royer, S.; Duprez, D., Catalytic Oxidation of Carbon Monoxide over Transition Metal Oxides. *Chemcatchem* **2011,** *3* (1), 24-65.

13. Shido, T.; Iwasawa, Y., Reactant-promoted reaction mechanism for water-gas shift reaction on Rh-doped CeO2. *Journal of catalysis* **1993,** *141* (1), 71-81.

14. Idriss, H.; Diagne, C.; Hindermann, J. P.; Kiennemann, A.; Barteau, M. A., Reactions of Acetaldehyde on Ceo2 and Ceo2-Supported Catalysts. *Journal of Catalysis* **1995,** *155* (2), 219-237.

15. Kugai, J.; Velu, S.; Song, C. S., Low-temperature reforming of ethanol over CeO2-supported Ni-Rh bimetallic catalysts for hydrogen production. *Catal Lett* **2005,** *101* (3-4), 255-264.

16. Deng, W.; Frenkel, A. I.; Si, R.; Flytzani-Stephanopoulos, M., Reaction-relevant gold structures in the low temperature water-gas shift reaction on Au-CeO2. *J Phys Chem C* **2008,** *112* (33), 12834-12840.

17. Panagiotopoulou, P.; Kondarides, D. I., Effect of morphological characteristics of TiO 2-supported noble metal catalysts on their activity for the water–gas shift reaction. *Journal of catalysis* **2004,** *225* (2), 327-336.

18. Park, K.-W.; Seol, K.-S., Nb-TiO 2 supported Pt cathode catalyst for polymer electrolyte membrane fuel cells. *Electrochemistry Communications* **2007,** *9* (9), 2256-2260.

19. Rodríguez, J. A.; Evans, J.; Graciani, J.; Park, J.-B.; Liu, P.; Hrbek, J.; Sanz, J. F., High Water− Gas Shift Activity in TiO2 (110) Supported Cu and Au Nanoparticles: Role of the Oxide and Metal Particle Size. *The Journal of Physical Chemistry C* **2009,** *113* (17), 7364-7370.

20. Parida, K.; Sahu, N.; Tripathi, A.; Kamble, V., Gold Promoted S, N− Doped TiO2: An Efficient Catalyst for CO Adsorption and Oxidation. *Environmental science & technology* **2010,** *44* (11), 4155-4160.

21. Lin, S. D.; Vannice, M. A., Hydrogenation of aromatic hydrocarbons over supported Pt catalysts. III. Reaction models for metal surfaces and acidic sites on oxide supports. *Journal of Catalysis* **1993,** *143* (2), 563-572.

22. Lordi, V.; Yao, N.; Wei, J., Method for supporting platinum on single-walled carbon nanotubes for a selective hydrogenation catalyst. *Chemistry of Materials* **2001,** *13* (3), 733-737.

23. Pena, D. A.; Uphade, B. S.; Smirniotis, P. G., TiO 2-supported metal oxide catalysts for low-temperature selective catalytic reduction of NO with NH 3: I. Evaluation and characterization of first row transition metals. *Journal of catalysis* **2004,** *221* (2), 421-431.

24. Henry, C. R., Surface studies of supported model catalysts. *Surf Sci Rep* **1998,** *31* (7-8), 235-325.

25. Chusuei, C. C.; Lai, X.; Luo, K.; Goodman, D., Modeling heterogeneous catalysts: metal clusters on planar oxide supports. *Topics in Catalysis* **2000,** *14* (1-4), 71-83.

26. Santra, A.; Goodman, D., Oxide-supported metal clusters: models for heterogeneous catalysts. *Journal of Physics: Condensed Matter* **2002,** *15* (2), R31.

27. Lopez, N.; Norskov, J. K., Catalytic CO oxidation by a gold nanoparticle: a density functional study. *J Am Chem Soc* **2002,** *124* (38), 11262-3.

28. Ferrando, R.; Jellinek, J.; Johnston, R. L., Nanoalloys: from theory to applications of alloy clusters and nanoparticles. *Chem Rev* **2008,** *108* (3), 845-910.

29. Prinz, J.; Gaspari, R.; Stockl, Q. S.; Gille, P.; Armbruster, M.; Brune, H.; Groning, O.; Pignedoli, C. A.; Passerone, D.; Widmer, R., Ensemble Effect Evidenced by CO Adsorption on the 3-Fold PdGa Surfaces. *J Phys Chem C* **2014,** *118* (23), 12260-12265.

30. Bauer, J. C.; Mullins, D.; Li, M.; Wu, Z.; Payzant, E. A.; Overbury, S. H.; Dai, S., Synthesis of silica supported AuCu nanoparticle catalysts and the effects of pretreatment conditions for the CO oxidation reaction. *Physical chemistry chemical physics : PCCP* **2011,** *13* (7), 2571-81.

31. Sakong, S.; Mosch, C.; Gross, A., CO adsorption on Cu-Pd alloy surfaces: ligand versus ensemble effects. *Physical chemistry chemical physics : PCCP* **2007,** *9* (18), 2216-25.

32. Zhang, J.; Jin, H.; Sullivan, M. B.; Lim, F. C. H.; Wu, P., Study of Pd–Au bimetallic catalysts for CO oxidation reaction by DFT calculations. *Physical Chemistry Chemical Physics* **2009,** *11* (9), 1441-1446.

33. Ramírez-Caballero, G. E.; Ma, Y.; Callejas-Tovar, R.; Balbuena, P. B., Surface segregation and stability of core–shell alloy catalysts for oxygen reduction in acid medium. *Physical Chemistry Chemical Physics* **2010,** *12* (9), 2209-2218.

34. Shin, K.; Kim, D. H.; Yeo, S. C.; Lee, H. M., Structural stability of AgCu bimetallic nanoparticles and their application as a catalyst: A DFT study. *Catalysis Today* **2012,** *185* (1), 94-98.

35. Kim, H. Y.; Henkelman, G., CO Adsorption-Driven Surface Segregation of Pd on Au/Pd Bimetallic Surfaces: Role of Defects and Effect on CO Oxidation. *Acs Catal* **2013,** *3* (11), 2541-2546.

36. Liao, F. L.; Lo, T. W. B.; Tsang, S. C. E., Recent Developments in Palladium-Based Bimetallic Catalysts. *Chemcatchem* **2015,** *7* (14), 1998-2014.

37. Hammer, B.; Norskov, J. K., Theoretical surface science and catalysis - Calculations and concepts. *Adv Catal* **2000,** *45*, 71-129.

38. Rodriguez, J. A.; Goodman, D. W., The nature of the metal-metal bond in bimetallic surfaces. *Science* **1992,** *257* (5072), 897-903.

39. Zhang, S.; Zhang, X.; Jiang, G.; Zhu, H.; Guo, S.; Su, D.; Lu, G.; Sun, S., Tuning nanoparticle structure and surface strain for catalysis optimization. *J Am Chem Soc* **2014,** *136* (21), 7734-9.

40. Pinto, L. M.; Maia, G., Oxygen adsorption on PdPt/Au (111)–DFT calculations. *The Journal of Physical Chemistry C* **2015,** *119* (15), 8213-8216.

41. Yang, F.; Deng, D. H.; Pan, X. L.; Fu, Q.; Bao, X. H., Understanding nano effects in catalysis. *Natl Sci Rev* **2015,** *2* (2), 183-201.

42. Mccue, A. J.; Anderson, J. A., CO induced surface segregation as a means of improving surface composition and enhancing performance of CuPd bimetallic catalysts. *Journal of Catalysis* **2015,** *329*, 538-546.

43. Alfonso, D. R., Comparative studies of CO and H2O interactions with Pd(111) surface: A theoretical study of poisoning. *Appl Phys Lett* **2006,** *88* (5), 1908.

44. Shao, M.; Liu, P.; Zhang, J.; Adzic, R., Origin of enhanced activity in palladium alloy electrocatalysts for oxygen reduction reaction. *The journal of physical chemistry. B* **2007,** *111* (24), 6772-5.

45. Paulus, U. A.; Wokaun, A.; Scherer, G. G.; Schmidt, T. J.; Stamenkovic, V.; Radmilovic, V.; Markovic, N. M.; Ross, P. N., Oxygen reduction on carbon-supported Pt-Ni and Pt-Co alloy catalysts. *Journal of Physical Chemistry B* **2002,** *106* (16), 4181-4191.

46. Orita, H.; Itoh, N.; Inada, Y., All electron scalar relativistic calculations on adsorption of CO on Pt(111) with full-geometry optimization: a correct estimation for CO site-preference. *Chem Phys Lett* **2004,** *384* (4-6), 271-276.

47. Xu, Y.; Ruban, A. V.; Mavrikakis, M., Adsorption and dissociation of O2 on Pt-Co and Pt-Fe alloys. *J Am Chem Soc* **2004,** *126* (14), 4717-25.

48. Miller, S. D.; Kitchin, J. R., Relating the coverage dependence of oxygen adsorption on Au and Pt fcc(111) surfaces through adsorbate-induced surface electronic structure effects. *Surface Science* **2009,** *603* (5), 794-801.

49. Jayasayee, K.; Van Veen, J. A. R.; Manivasagam, T. G.; Celebi, S.; Hensen, E. J. M.; de Bruijn, F. A., Oxygen reduction reaction (ORR) activity and durability of carbon supported PtM (Co, Ni, Cu) alloys: Influence of particle size and non-noble metals. *Appl Catal B-Environ* **2012,** *111*, 515-526.

50. Lankiang, S.; Chiwata, M.; Baranton, S.; Uchida, H.; Coutanceau, C., Oxygen reduction reaction at binary and ternary nanocatalysts based on Pt, Pd and Au. *Electrochimica Acta* **2015,** *182*, 131-142.

51. Yu, L.; Liu, Y.; Yang, F.; Evans, J.; Rodriguez, J. A.; Liu, P., CO oxidation on gold-supported iron oxides: New insights into strong oxide–metal interactions. *The Journal of Physical Chemistry C* **2015,** *119* (29), 16614-16622.

52. Mancera, L. A.; Behm, R. J.; Gross, A., Structure and local reactivity of PdAg/Pd(111) surface alloys. *Physical chemistry chemical physics : PCCP* **2013,** *15* (5), 1497-508.

53. Ma, Y. S.; Diemant, T.; Bansmann, J.; Behm, R. J., The interaction of CO with PdAg/Pd(111) surface alloys-A case study of ensemble effects on a bimetallic surface. *Physical Chemistry Chemical Physics* **2011,** *13* (22), 10741-10754.

54. Kyriakou, G.; Boucher, M. B.; Jewell, A. D.; Lewis, E. A.; Lawton, T. J.; Baber, A. E.; Tierney, H. L.; Flytzani-Stephanopoulos, M.; Sykes, E. C. H., Isolated metal atom geometries as a strategy for selective heterogeneous hydrogenations. *Science* **2012,** *335* (6073), 1209-1212.

55. Fu, Q.; Luo, Y., Active sites of Pd-doped flat and stepped Cu (111) surfaces for H2 dissociation in heterogeneous catalytic hydrogenation. *Acs Catal* **2013,** *3* (6), 1245-1252.

56. Thomas, J. M.; Raja, R.; Lewis, D. W., Single-site heterogeneous catalysts. *Angewandte Chemie International Edition* **2005,** *44* (40), 6456-6482.

57. Qiao, B.; Wang, A.; Yang, X.; Allard, L. F.; Jiang, Z.; Cui, Y.; Liu, J.; Li, J.; Zhang, T., Single-atom catalysis of CO oxidation using Pt1/FeOx. *Nature chemistry* **2011,** *3* (8), 634-641.

58. Novotný, Z.; Argentero, G.; Wang, Z.; Schmid, M.; Diebold, U.; Parkinson, G. S., Ordered array of single adatoms with remarkable thermal stability: Au/Fe 3 O 4 (001). *Physical review letters* **2012,** *108* (21), 216103.

59. Yang, X. F.; Wang, A.; Qiao, B.; Li, J.; Liu, J.; Zhang, T., Single-atom catalysts: a new frontier in heterogeneous catalysis. *Acc Chem Res* **2013,** *46* (8), 1740-8.

60. Duan, H.; Li, M. H.; Zhang, G. H.; Gallagher, J. R.; Huang, Z. L.; Sun, Y.; Luo, Z.; Chen, H. Z.; Miller, J. T.; Zou, R. Q.; Lei, A. W.; Zhao, Y. L., Single-Site Palladium(II) Catalyst for Oxidative Heck Reaction: Catalytic Performance and Kinetic Investigations. *Acs Catal* **2015,** *5* (6), 3752-3759.

61. Liang, S. X.; Hao, C.; Shi, Y. T., The Power of Single-Atom Catalysis. *Chemcatchem* **2015,** *7* (17), 2559-2567.

62. Qiao, B. T.; Liang, J. X.; Wang, A. Q.; Xu, C. Q.; Li, J.; Zhang, T.; Liu, J. Y., Ultrastable single-atom gold catalysts with strong covalent metal-support interaction (CMSI). *Nano Res* **2015,** *8* (9), 2913-2924.

63. Liu, C. S.; Ye, X. J.; Wang, X. F.; Yan, X. H.; Zeng, Z., Quantum-size effect on the electronic and optical properties of hybrid TiO2/Au clusters. *J Chem Phys* **2014,** *141* (5), 054301.

64. Yang, X.-F.; Wang, A.; Qiao, B.; Li, J.; Liu, J.; Zhang, T., Single-atom catalysts: a new frontier in heterogeneous catalysis. *Accounts of chemical research* **2013,** *46* (8), 1740-1748.

65. Ghosh, T. K.; Nair, N. N., Rh1/γ-Al2O3 Single-Atom Catalysis of O2 Activation and CO Oxidation: Mechanism, Effects of Hydration, Oxidation State, and Cluster Size. *ChemCatChem* **2013,** *5* (7), 1811-1821.

66. Liang, J.-X.; Lin, J.; Yang, X.-F.; Wang, A.-Q.; Qiao, B.-T.; Liu, J.; Zhang, T.; Li, J., Theoretical and Experimental Investigations on Single-Atom Catalysis: Ir1/FeO x for CO Oxidation. *The Journal of Physical Chemistry C* **2014,** *118* (38), 21945-21951.

67. Tang, Y.; Yang, Z.; Dai, X., A theoretical simulation on the catalytic oxidation of CO on Pt/graphene. *Physical chemistry chemical physics : PCCP* **2012,** *14* (48), 16566-72.

68. Sun, S. H.; Zhang, G. X.; Gauquelin, N.; Chen, N.; Zhou, J. G.; Yang, S. L.; Chen, W. F.; Meng, X. B.; Geng, D. S.; Banis, M. N.; Li, R. Y.; Ye, S. Y.; Knights, S.; Botton, G. A.; Sham, T. K.; Sun, X. L., Single-atom Catalysis Using Pt/Graphene Achieved through Atomic Layer Deposition. *Scientific Reports* **2013,** *3*.

69. Kwak, J. H.; Hu, J. Z.; Mei, D.; Yi, C. W.; Kim, D. H.; Peden, C. H. F.; Allard, L. F.; Szanyi, J., Coordinatively Unsaturated Al3+ Centers as Binding Sites for Active Catalyst Phases of Platinum on gamma-Al2O3. *Science* **2009,** *325* (5948), 1670-1673.

70. Li, F.; Li, Y.; Zeng, X. C.; Chen, Z., Exploration of High-Performance Single-Atom Catalysts on Support M1/FeO x for CO Oxidation via Computational Study. *Acs Catal* **2014,** *5* (2), 544-552.

71. Moses-DeBusk, M.; Yoon, M.; Allard, L. F.; Mullins, D. R.; Wu, Z. L.; Yang, X. F.; Veith, G.; Stocks, G. M.; Narula, C. K., CO Oxidation on Supported Single Pt Atoms: Experimental and ab Initio Density Functional Studies of CO Interaction with Pt Atom on theta-Al2O3(010) Surface. *Journal of the American Chemical Society* **2013,** *135* (34), 12634-12645.

72. Zhang, R. Q.; Lee, T. H.; Yu, B. D.; Stampfl, C.; Soon, A., The role of titanium nitride supports for single-atom platinum-based catalysts in fuel cell technology. *Physical chemistry chemical physics : PCCP* **2012,** *14* (48), 16552-7.

73. Cao, X. R.; Fu, Q.; Luo, Y., Catalytic activity of Pd-doped Cu nanoparticles for hydrogenation as a single-atom-alloy catalyst. *Physical Chemistry Chemical Physics* **2014,** *16* (18), 8367-8375.

74. Fu, Q.; Luo, Y., Catalytic Activity of Single Transition-Metal Atom Doped in Cu(111) Surface for Heterogeneous Hydrogenation. *J Phys Chem C* **2013,** *117* (28), 14618-14624.

75. Council, N. R., *Catalysis looks to the future*. National Academies Press: 1992.

76. Ross, J. R., *Heterogeneous catalysis: fundamentals and applications*. Elsevier: 2011.

77. Van Santen, R. A.; Neurock, M., *Molecular heterogeneous catalysis: a conceptual and computational approach*. John Wiley & Sons: 2009.

78. Haruta, M.; Yamada, N.; Kobayashi, T.; Iijima, S., Gold catalysts prepared by coprecipitation for low-temperature oxidation of hydrogen and of carbon monoxide. *Journal of catalysis* **1989,** *115* (2), 301-309.

79. Haruta, M., Size-and support-dependency in the catalysis of gold. *Catalysis today* **1997,** *36* (1), 153-166.

80. Hansgen, D. A.; Vlachos, D. G.; Chen, J. G., Using first principles to predict bimetallic catalysts for the ammonia decomposition reaction. *Nature chemistry* **2010,** *2* (6), 484.

81. Alonso, D. M.; Wettstein, S. G.; Dumesic, J. A., Bimetallic catalysts for upgrading of biomass to fuels and chemicals. *Chemical Society Reviews* **2012,** *41* (24), 8075-8098.

82. Yu, W.; Porosoff, M. D.; Chen, J. G., Review of Pt-based bimetallic catalysis: from model surfaces to supported catalysts. *Chemical reviews* **2012,** *112* (11), 5780-5817.

83. Strohl, J. K.; King, T. S., Monte Carlo simulations of supported bimetallic catalysts. *Journal of Catalysis* **1989,** *116* (2), 540-555.

84. Alayoglu, S.; Nilekar, A. U.; Mavrikakis, M.; Eichhorn, B., Ru–Pt core–shell nanoparticles for preferential oxidation of carbon monoxide in hydrogen. *Nature materials* **2008,** *7* (4), 333.

85. Gauthier, Y.; Schmid, M.; Padovani, S.; Lundgren, E.; Buš, V.; Kresse, G.; Redinger, J.; Varga, P., Adsorption sites and ligand effect for CO on an alloy surface: a direct view. *Physical review letters* **2001,** *87* (3), 036103.

86. Liu, P.; Nørskov, J. K., Ligand and ensemble effects in adsorption on alloy surfaces. *Physical Chemistry Chemical Physics* **2001,** *3* (17), 3814-3818.

87. Hammer, B., Special sites at noble and late transition metal catalysts. *Topics in Catalysis* **2006,** *37* (1), 3-16.

88. Koh, S.; Strasser, P., Electrocatalysis on bimetallic surfaces: modifying catalytic reactivity for oxygen reduction by voltammetric surface dealloying. *Journal of the American Chemical Society* **2007,** *129* (42), 12624-12625.

89. Wang, Y.-G.; Mei, D.; Glezakou, V.-A.; Li, J.; Rousseau, R., Dynamic formation of single-atom catalytic active sites on ceria-supported gold nanoparticles. *Nature communications* **2015,** *6*, 6511.

90. Sun, S.; Zhang, G.; Gauquelin, N.; Chen, N.; Zhou, J.; Yang, S.; Chen, W.; Meng, X.; Geng, D.; Banis, M. N., Single-atom catalysis using Pt/graphene achieved through atomic layer deposition. *Scientific reports* **2013,** *3*, 1775.

91. Groß, A., Tailoring the reactivity of bimetallic overlayer and surface alloy systems. *Journal of Physics: Condensed Matter* **2009,** *21* (8), 084205.

92. Hammer, B.; Norskov, J., Why gold is the noblest of all the metals. *Nature* **1995,** *376* (6537), 238.

93. Hammer, B.; Nørskov, J., Electronic factors determining the reactivity of metal surfaces. *Surface Science* **1995,** *343* (3), 211-220.

94. Hammer, B.; Nørskov, J. K., Theoretical surface science and catalysis—calculations and concepts. In *Advances in catalysis*, Elsevier: 2000; Vol. 45, pp 71-129.

95. Nørskov, J. K.; Bligaard, T.; Logadottir, A.; Bahn, S.; Hansen, L. B.; Bollinger, M.; Bengaard, H.; Hammer, B.; Sljivancanin, Z.; Mavrikakis, M., Universality in heterogeneous catalysis. *Journal of Catalysis* **2002,** *209* (2), 275-278.

96. Bligaard, T.; Nørskov, J. K.; Dahl, S.; Matthiesen, J.; Christensen, C. H.; Sehested, J., The Brønsted–Evans–Polanyi relation and the volcano curve in heterogeneous catalysis. *Journal of Catalysis* **2004,** *224* (1), 206-217.

97. Cheng, J.; Hu, P.; Ellis, P.; French, S.; Kelly, G.; Lok, C. M., Brønsted− Evans− Polanyi relation of multistep reactions and volcano curve in heterogeneous catalysis. *The Journal of Physical Chemistry C* **2008,** *112* (5), 1308-1311.

98. Nørskov, J. K.; Abild-Pedersen, F.; Studt, F.; Bligaard, T., Density functional theory in surface chemistry and catalysis. *Proceedings of the National Academy of Sciences* **2011,** *108* (3), 937-943.

99. Nørskov, J. K.; Bligaard, T.; Rossmeisl, J.; Christensen, C. H., Towards the computational design of solid catalysts. *Nature chemistry* **2009,** *1* (1), 37.

100. Nørskov, J. K.; Bligaard, T.; Hvolbæk, B.; Abild-Pedersen, F.; Chorkendorff, I.; Christensen, C. H., The nature of the active site in heterogeneous metal catalysis. *Chemical Society Reviews* **2008,** *37* (10), 2163-2171.

101. Schrödinger, E., An undulatory theory of the mechanics of atoms and molecules. *Physical review* **1926,** *28* (6), 1049.

102. Jensen, F., *Introduction to computational chemistry*. John wiley & sons: 2017.

103. Born, M.; Oppenheimer, R., Zur quantentheorie der molekeln. *Annalen der Physik* **1927,** *389* (20), 457-484.

104. Gaunt, J. In *A Theory of Hartree's Atomic Fields*, Mathematical Proceedings of the Cambridge Philosophical Society, Cambridge University Press: 1928; pp 328-342.

105. Hartree, D. R. In *The wave mechanics of an atom with a non-Coulomb central field. Part I. Theory and methods*, Mathematical Proceedings of the Cambridge Philosophical Society, Cambridge University Press: 1928; pp 89-110.

106. Slater, J. C., The theory of complex spectra. *Physical Review* **1929,** *34* (10), 1293.

107. Robert, G.; Weitao, Y., Density-functional theory of atoms and molecules. Oxford University Press New York: 1989.

108. Hohenberg, P.; Kohn, W., Inhomogeneous electron gas. *Physical review* **1964,** *136* (3B), B864.

109. Gilbert, T., Hohenberg-Kohn theorem for nonlocal external potentials. *Physical Review B* **1975,** *12* (6), 2111.

110. Kohn, W.; Sham, L. J., Self-consistent equations including exchange and correlation effects. *Physical review* **1965,** *140* (4A), A1133.

111. Hedin, L.; Lundqvist, B. I., Explicit local exchange-correlation potentials. *Journal of Physics C: Solid state physics* **1971,** *4* (14), 2064.

112. Ceperley, D. M.; Alder, B., Ground state of the electron gas by a stochastic method. *Physical Review Letters* **1980,** *45* (7), 566.

113. Ceperley, D. M.; Alder, B. J., Ground State of the Electron Gas by a Stochastic Method. *Physical Review Letters* **1980,** *45* (7), 566-569.

114. Becke, A. D., Density-functional thermochemistry. I. The effect of the exchange-only gradient correction. *The Journal of Chemical Physics* **1992,** *96* (3), 2155-2160.

115. Becke, A. D., Density-functional thermochemistry. II. The effect of the Perdew–Wang generalized-gradient correlation correction. *The Journal of chemical physics* **1992,** *97* (12), 9173-9177.

116. Becke, A. D., Density-functional thermochemistry. III. The role of exact exchange. *The Journal of chemical physics* **1993,** *98* (7), 5648-5652.

117. Perdew, J. P.; Wang, Y., Accurate and simple analytic representation of the electron-gas correlation energy. *Physical Review B* **1992,** *45* (23), 13244.

118. Perdew, J. P.; Burke, K.; Ernzerhof, M., Generalized gradient approximation made simple. *Physical review letters* **1996,** *77* (18), 3865.

119. Lee, C.; Yang, W.; Parr, R. G., Development of the Colle-Salvetti correlation-energy formula into a functional of the electron density. *Physical review B* **1988,** *37* (2), 785.

120. Heyd, J.; Scuseria, G. E.; Ernzerhof, M., Hybrid functionals based on a screened Coulomb potential. *The Journal of chemical physics* **2003,** *118* (18), 8207-8215.

121. Heyd, J.; Scuseria, G. E., Assessment and validation of a screened Coulomb hybrid density functional. *The Journal of chemical physics* **2004,** *120* (16), 7274-7280.

122. Blöchl, P. E., Projector augmented-wave method. *Physical review B* **1994,** *50* (24), 17953.

123. Kresse, G.; Joubert, D., From ultrasoft pseudopotentials to the projector augmented-wave method. *Physical Review B* **1999,** *59* (3), 1758.

124. Curtarolo, S.; Hart, G. L.; Nardelli, M. B.; Mingo, N.; Sanvito, S.; Levy, O., The high-throughput highway to computational materials design. *Nature materials* **2013,** *12* (3), 191.

125. Jain, A.; Shin, Y.; Persson, K. A., Computational predictions of energy materials using density functional theory. *Nature Reviews Materials* **2016,** *1* (1), 15004.

126. Hammer, B.; Morikawa, Y.; Nørskov, J. K., CO chemisorption at metal surfaces and overlayers. *Physical review letters* **1996,** *76* (12), 2141.

127. Stamenkovic, V. R.; Mun, B. S.; Arenz, M.; Mayrhofer, K. J.; Lucas, C. A.; Wang, G.; Ross, P. N.; Markovic, N. M., Trends in electrocatalysis on extended and nanoscale Pt-bimetallic alloy surfaces. *Nature materials* **2007,** *6* (3), 241.

128. Bronsted, J., Acid and Basic Catalysis. *Chemical Reviews* **1928,** *5* (3), 231-338.

129. Evans, M.; Polanyi, M., Inertia and driving force of chemical reactions. *Transactions of the Faraday Society* **1938,** *34*, 11-24.

130. Munter, T. R.; Bligaard, T.; Christensen, C. H.; Nørskov, J. K., BEP relations for N 2 dissociation over stepped transition metal and alloy surfaces. *Physical Chemistry Chemical Physics* **2008,** *10* (34), 5202-5206.

131. Logadottir, A.; Rod, T. H.; Nørskov, J. K.; Hammer, B.; Dahl, S.; Jacobsen, C., The Brønsted–Evans–Polanyi relation and the volcano plot for ammonia synthesis over transition metal catalysts. *Journal of Catalysis* **2001,** *197* (2), 229-231.

132. Alcala, R.; Mavrikakis, M.; Dumesic, J. A., DFT studies for cleavage of C C and C O bonds in surface species derived from ethanol on Pt (111). *Journal of Catalysis* **2003,** *218* (1), 178-190.

133. Michaelides, A.; Liu, Z.-P.; Zhang, C.; Alavi, A.; King, D. A.; Hu, P., Identification of general linear relationships between activation energies and enthalpy changes for dissociation reactions at surfaces. *Journal of the American Chemical Society* **2003,** *125* (13), 3704-3705.

134. Balandin, A., Modern State of the Multiplet Theor of Heterogeneous Catalysis. In *Advances in catalysis*, Elsevier: 1969; Vol. 19, pp 1-210.

135. Greeley, J., Theoretical heterogeneous catalysis: scaling relationships and computational catalyst design. *Annual review of chemical and biomolecular engineering* **2016,** *7*, 605-635.

136. Abild-Pedersen, F.; Greeley, J.; Studt, F.; Rossmeisl, J.; Munter, T.; Moses, P. G.; Skulason, E.; Bligaard, T.; Nørskov, J. K., Scaling properties of adsorption energies for hydrogen-containing molecules on transition-metal surfaces. *Physical review letters* **2007,** *99* (1), 016105.

137. Baxter, R.; Hu, P., Insight into why the Langmuir–Hinshelwood mechanism is generally preferred. *The Journal of chemical physics* **2002,** *116* (11), 4379-4381.

138. Kumar, K. V.; Porkodi, K.; Rocha, F., Langmuir–Hinshelwood kinetics–a theoretical study. *Catalysis Communications* **2008,** *9* (1), 82-84.

139. Cacciatore, M.; Rutigliano, M.; Billing, G. D., Eley-Rideal and Langmuir-Hinshelwood recombination coefficients for oxygen on silica surfaces. *Journal of Thermophysics and Heat Transfer* **1999,** *13* (2), 195-203.

140. He, W.; Wu, X.; Liu, J.; Hu, X.; Zhang, K.; Hou, S.; Zhou, W.; Xie, S., Design of AgM bimetallic alloy nanostructures (M= Au, Pd, Pt) with tunable morphology and peroxidase-like activity. *Chemistry of Materials* **2010,** *22* (9), 2988-2994.

141. Zhu, C.; Guo, S.; Dong, S., PdM (M= Pt, Au) Bimetallic Alloy Nanowires with Enhanced Electrocatalytic Activity for Electro-oxidation of Small Molecules. *Advanced Materials* **2012,** *24* (17), 2326-2331.

142. Singh, A. K.; Xu, Q., Synergistic catalysis over bimetallic alloy nanoparticles. *ChemCatChem* **2013,** *5* (3), 652-676.

143. Luo, M.; Sun, Y.; Wang, L.; Guo, S., Tuning multimetallic ordered intermetallic nanocrystals for efficient energy electrocatalysis. *Advanced Energy Materials* **2017,** *7* (11).

144. Ramesh, G. V.; Kodiyath, R.; Tanabe, T.; Manikandan, M.; Fujita, T.; Matsumoto, F.; Ishihara, S.; Ueda, S.; Yamashita, Y.; Ariga, K., NbPt3 Intermetallic Nanoparticles: Highly Stable and CO-Tolerant Electrocatalyst for Fuel Oxidation. *ChemElectroChem* **2014,** *1* (4), 728-732.

145. Lang, X. Y.; Han, G. F.; Xiao, B. B.; Gu, L.; Yang, Z. Z.; Wen, Z.; Zhu, Y. F.; Zhao, M.; Li, J. C.; Jiang, Q., Mesostructured Intermetallic Compounds of Platinum and Non-Transition Metals for Enhanced Electrocatalysis of Oxygen Reduction Reaction. *Advanced Functional Materials* **2015,** *25* (2), 230-237.

146. Chen, L.; Bock, C.; Mercier, P.; MacDougall, B., Ordered alloy formation for Pt3Fe/C, PtFe/C and Pt5. 75Fe5. 75Cuy/CO2-reduction electro-catalysts. *Electrochimica Acta* **2012,** *77*, 212-224.

147. Abild-Pedersen, F.; Greeley, J.; Nørskov, J. K., Understanding the effect of steps, strain, poisons, and alloying: Methane activation on Ni surfaces. *Catal Lett* **2005,** *105* (1-2), 9-13.

148. Norskov, J. K.; Bligaard, T.; Rossmeisl, J.; Christensen, C. H., Towards the computational design of solid catalysts. *Nat Chem* **2009,** *1* (1), 37-46.

149. Poizot, P.; Dolhem, F., Clean energy new deal for a sustainable world: from non-CO 2 generating energy sources to greener electrochemical storage devices. *Energy & Environmental Science* **2011,** *4* (6), 2003-2019.

150. Sakong, S.; Mosch, C.; Groß, A., CO adsorption on Cu–Pd alloy surfaces: ligand versus ensemble effects. *Physical Chemistry Chemical Physics* **2007,** *9* (18), 2216-2225.

151. Öberg, H.; Anniyev, T.; Vojvodic, A.; Kaya, S.; Ogasawara, H.; Friebel, D.; Miller, D. J.; Nordlund, D.; Bergmann, U.; Ljungberg, M. P., Stability of Pt-modified Cu (111) in the presence of oxygen and its implication on the overall electronic structure. *The Journal of Physical Chemistry C* **2013,** *117* (32), 16371-16380.

152. Song, C., Fuel processing for low-temperature and high-temperature fuel cells: Challenges, and opportunities for sustainable development in the 21st century. *Catalysis today* **2002,** *77* (1), 17-49.

153. Wang, D.; Villa, A.; Porta, F.; Prati, L.; Su, D., Bimetallic gold/palladium catalysts: Correlation between nanostructure and synergistic effects. *The Journal of Physical Chemistry C* **2008,** *112* (23), 8617-8622.

154. Freund, H. J.; Meijer, G.; Scheffler, M.; Schlögl, R.; Wolf, M., CO oxidation as a prototypical reaction for heterogeneous processes. *Angewandte Chemie International Edition* **2011,** *50* (43), 10064-10094.

155. Cheng, X.; Shi, Z.; Glass, N.; Zhang, L.; Zhang, J. J.; Song, D. T.; Liu, Z. S.; Wang, H. J.; Shen, J., A review of PEM hydrogen fuel cell contamination: Impacts, mechanisms, and mitigation. *J Power Sources* **2007,** *165* (2), 739-756.

156. Liu, B.; Liu, J.; Li, T.; Zhao, Z.; Gong, X. Q.; Chen, Y.; Duan, A. J.; Jiang, G. Y.; Wei, Y. C., Interfacial Effects of CeO2-Supported Pd Nanorod in Catalytic CO Oxidation: A Theoretical Study. *J Phys Chem C* **2015,** *119* (23), 12923-12934.

157. Schmittinger, W.; Vahidi, A., A review of the main parameters influencing long-term performance and durability of PEM fuel cells. *J Power Sources* **2008,** *180* (1), 1-14.

158. Shao, M.-H.; Sasaki, K.; Adzic, R. R., Pd-Fe nanoparticles as electrocatalysts for oxygen reduction. *Journal of the American Chemical Society* **2006,** *128* (11), 3526-3527.

159. Suo, Y.; Zhuang, L.; Lu, J., First-Principles Considerations in the Design of Pd-Alloy Catalysts for Oxygen Reduction. *Angewandte Chemie International Edition* **2007,** *46* (16), 2862-2864.

160. Liu, B.; Zhao, Z.; Henkelman, G.; Song, W., Computational Design of a CeO2-Supported Pd-Based Bimetallic Nanorod for CO Oxidation. *The Journal of Physical Chemistry C* **2016,** *120* (10), 5557-5564.

161. Ruban, A.; Skriver, H. L.; Nørskov, J. K., Surface segregation energies in transition-metal alloys. *Physical Review B* **1999,** *59* (24), 15990.

162. Groß, A., Reactivity of bimetallic systems studied from first principles. *Topics in Catalysis* **2006,** *37* (1), 29-39.

163. Jelic, J.; Meyer, R. J., A DFT study of pseudomorphic monolayer Pt and Pd catalysts for NO x storage reduction applications. *Catalysis Today* **2008,** *136* (1), 76-83.

164. Monkhorst, H. J.; Pack, J. D., Special points for Brillouin-zone integrations. *Physical review B* **1976,** *13* (12), 5188.

165. Kresse, G.; Furthmüller, J., Efficient iterative schemes for ab initio total-energy calculations using a plane-wave basis set. *Phys Rev B* **1996,** *54*, 11169.

166. Perdew, J. P.; Chevary, J. A.; Vosko, S. H.; Jackson, K. A.; Pederson, M. R.; Singh, D. J.; Fiolhais, C., Atoms, molecules, solids, and surfaces: Applications of the generalized gradient approximation for exchange and correlation. *Phys Rev B* **1992,** *46*, 6671.

167. Yuan, D. W.; Liu, Z. R.; Chen, J. H., Catalytic activity of Pd ensembles over Au(111) surface for CO oxidation: a first-principles study. *J Chem Phys* **2011,** *134* (5), 054704.

168. Kresse, G.; Gil, A.; Sautet, P., Significance of single-electron energies for the description of CO on Pt (111). *Physical Review B* **2003,** *68* (7), 073401.

169. Gambardella, P.; Šljivančanin, Ž.; Hammer, B.; Blanc, M.; Kuhnke, K.; Kern, K., Oxygen dissociation at Pt steps. *Physical review letters* **2001,** *87* (5), 056103.

170. Henkelman, G.; Uberuaga, B. P.; Jónsson, H., A climbing image nudged elastic band method for finding saddle points and minimum energy paths. *The Journal of chemical physics* **2000,** *113* (22), 9901-9904.

171. Zhang, C. J.; Hu, P., CO oxidation on Pd(100) and Pd(111): A comparative study of reaction pathways and reactivity at low and medium coverages. *Journal of the American Chemical Society* **2001,** *123* (6), 1166-1172.

172. Zhang, C.; Baxter, R.; Hu, P.; Alavi, A.; Lee, M.-H., A density functional theory study of carbon monoxide oxidation on the Cu3Pt (111) alloy surface: Comparison with the reactions on Pt (111) and Cu (111). *The Journal of Chemical Physics* **2001,** *115* (11), 5272-5277.

173. Falsig, H.; Hvolbaek, B.; Kristensen, I. S.; Jiang, T.; Bligaard, T.; Christensen, C. H.; Norskov, J. K., Trends in the catalytic CO oxidation activity of nanoparticles. *Angewandte Chemie* **2008,** *47* (26), 4835-9.

174. Jiang, T.; Mowbray, D.; Dobrin, S.; Falsig, H.; Hvolbæk, B.; Bligaard, T.; Nørskov, J. K., Trends in CO oxidation rates for metal nanoparticles and close-packed, stepped, and kinked surfaces. *The Journal of Physical Chemistry C* **2009,** *113* (24), 10548-10553.

175. Borup, R.; Meyers, J.; Pivovar, B.; Kim, Y. S.; Mukundan, R.; Garland, N.; Myers, D.; Wilson, M.; Garzon, F.; Wood, D., Scientific aspects of polymer electrolyte fuel cell durability and degradation. *Chemical reviews* **2007,** *107*, 3904-3951.

176. Cheng, X.; Shi, Z.; Glass, N.; Zhang, L.; Zhang, J.; Song, D.; Liu, Z.-S.; Wang, H.; Shen, J., A review of PEM hydrogen fuel cell contamination: Impacts, mechanisms, and mitigation. *J Power Sources* **2007,** *165*, 739-756.

177. Farrell, C.; Gardner, C.; Ternan, M., Experimental and modelling studies of CO poisoning in PEM fuel cells. *J Power Sources* **2007,** *171*, 282-293.

178. Shao, Y.; Yin, G.; Gao, Y., Understanding and approaches for the durability issues of Pt-based catalysts for PEM fuel cell. *J Power Sources* **2007,** *171*, 558-566.

179. Yang, C.; Costamagna, P.; Srinivasan, S.; Benziger, J.; Bocarsly, A., Approaches and technical challenges to high temperature operation of proton exchange membrane fuel cells. *J Power Sources* **2001,** *103*, 1-9.

180. Bashyam, R.; Zelenay, P., A class of non-precious metal composite catalysts for fuel cells. *Nature* **2006,** *443*, 63-66.

181. Liu, Z.; Ma, L.; Zhang, J.; Hongsirikarn, K.; Goodwin Jr, J. G., Pt alloy electrocatalysts for proton exchange membrane fuel cells: a review. *Catal Rev* **2013,** *55*, 255-288.

182. Igarashi, H.; Fujino, T.; Zhu, Y.; Uchida, H.; Watanabe, M., CO tolerance of Pt alloy electrocatalysts for polymer electrolyte fuel cells and the detoxification mechanism. *Physical Chemistry Chemical Physics* **2001,** *3*, 306-314.

183. Han, B.; Ceder, G., Effect of coadsorption and Ru alloying on the adsorption of CO on Pt. *Physical Review B* **2006,** *74*, 205418.

184. Nilekar, A. U.; Sasaki, K.; Farberow, C. A.; Adzic, R. R.; Mavrikakis, M., Mixed-metal Pt monolayer electrocatalysts with improved CO tolerance. *Journal of the American Chemical Society* **2011,** *133*, 18574-18576.

185. Watanabe, M.; Zhu, Y.; Igarashi, H.; Uchida, H., Mechanism of CO tolerance at Pt-alloy anode catalysts for polymer electrolyte fuel cells. *Electrochemistry* **2000,** *68*, 244-251.

186. Markovic, N. R.; Ross, P., New electrocatalysts for fuel cells from model surfaces to commercial catalysts. *Cattech* **2000,** *4*, 110-126.

187. Giorgi, L.; Pozio, A.; Bracchini, C.; Giorgi, R.; Turtu, S., H_2 and H_2/CO oxidation mechanism on Pt/C, Ru/C and Pt–Ru/C electrocatalysts. *Journal of applied electrochemistry* **2001,** *31*, 325-334.

188. Christoffersen, E.; Stoltze, P.; Nørskov, J. K., Monte Carlo simulations of adsorption-induced segregation. *Surface science* **2002,** *505*, 200-214.

189. Han, B.; Van der Ven, A.; Ceder, G.; Hwang, B.-J., Surface segregation and ordering of alloy surfaces in the presence of adsorbates. *Physical Review B* **2005,** *72*, 205409.

190. Feibelman, P. J.; Hammer, B.; Nørskov, J. K.; Wagner, F.; Scheffler, M.; Stumpf, R.; Watwe, R.; Dumesic, J., The CO/Pt (111) puzzle. *The journal of physical chemistry. B* **2001,** *108*, 4018-4025.

191. Schimka, L.; Harl, J.; Stroppa, A.; Grüneis, A.; Marsman, M.; Mittendorfer, F.; Kresse, G., Accurate surface and adsorption energies from many-body perturbation theory. *Nat Mater* **2010,** *9*, 741-744.

192. Nilekar, A. U.; Alayoglu, S.; Eichhorn, B.; Mavrikakis, M., Preferential CO oxidation in hydrogen: reactivity of core− shell nanoparticles. *Journal of the American Chemical Society* **2010,** *132*, 7418-7428.

193. Jensen, J. A.; Rider, K. B.; Salmeron, M.; Somorjai, G. A., High pressure adsorbate structures studied by scanning tunneling microscopy: CO on Pt (111) in equilibrium with the gas phase. *Physical review letters* **1998,** *80* (6), 1228.

194. Davies, J. C.; Nielsen, R.; Thomsen, L. B.; Chorkendorff, I.; Logadottir, A.; Lodziana, Z.; Nørskov, J. K.; Li, W.; Hammer, B.; Longwitz, S., CO desorption rate dependence on CO partial pressure over platinum fuel cell catalysts. *Fuel Cells* **2004,** *4*, 309-319.

195. Christoffersen, E.; Liu, P.; Ruban, A.; Skriver, H. L.; Nørskov, J. K., Anode materials for low-temperature fuel cells: a density functional theory study. *Journal of Catalysis* **2001,** *199*, 123-131.

196. Wang, B., Recent development of non-platinum catalysts for oxygen reduction reaction. *J Power Sources* **2005,** *152*, 1-15.

197. Stamenkovic, V.; Mun, B. S.; Mayrhofer, K. J.; Ross, P. N.; Markovic, N. M.; Rossmeisl, J.; Greeley, J.; Nørskov, J. K., Changing the activity of electrocatalysts for oxygen reduction by tuning the surface electronic structure. *Angew. Chem* **2006,** *118* (18), 2963-2967.

198. Jaouen, F.; Proietti, E.; Lefèvre, M.; Chenitz, R.; Dodelet, J.-P.; Wu, G.; Chung, H. T.; Johnston, C. M.; Zelenay, P., Recent advances in non-precious metal catalysis for oxygen-reduction reaction in polymer electrolyte fuel cells. *Energy Environ. Sci.* **2011,** *4* (1), 114-130.

199. Wang, C.; Markovic, N. M.; Stamenkovic, V. R., Advanced platinum alloy electrocatalysts for the oxygen reduction reaction. *ACS Catal.* **2012,** *2* (5), 891-898.

200. Shao, M.; Shoemaker, K.; Peles, A.; Kaneko, K.; Protsailo, L., Pt monolayer on porous Pd− Cu alloys as oxygen reduction electrocatalysts. *Journal of the American Chemical Society* **2010,** *132* (27), 9253-9255.

201. Shrestha, S.; Liu, Y.; Mustain, W. E., Electrocatalytic activity and stability of Pt clusters on state-of-the-art supports: a review. *Cat. Rev.* **2011,** *53* (3), 256-336.

202. Gómez-Marín, A. M.; Rizo, R.; Feliu, J. M., Oxygen reduction reaction at Pt single crystals: a critical overview. *Catal. Sci. Technol.* **2014,** *4* (6), 1685-1698.

203. Tang, W.; Zhang, L.; Henkelman, G., Catalytic activity of Pd/Cu random alloy nanoparticles for oxygen reduction. *J. Phys. Chem. Lett.* **2011,** *2* (11), 1328-1331.

204. Li, X.; Zhong, W.; Cui, P.; Li, J.; Jiang, J., Design of efficient catalysts with double transition metal atoms on C2N layer. *J. Phys. Chem. Lett.* **2016,** *7* (9), 1750-1755.

205. Zuluaga, S.; Stolbov, S., Factors controlling the energetics of the oxygen reduction reaction on the Pd-Co electro-catalysts: Insight from first principles. *J. Chem. Phys.* **2011,** *135* (13), 134702.

206. Chen, Z. Z.; Zhang, X.; Lu, G., Multiscale Computational Design of Core/Shell Nanoparticles for Oxygen Reduction Reaction. *J. Phys. Chem. C* **2017,** *121* (3), 1964-1973.

207. Fernández, J. L.; Raghuveer, V.; Manthiram, A.; Bard, A. J., Pd− Ti and Pd− Co− Au electrocatalysts as a replacement for platinum for oxygen reduction in proton exchange membrane fuel cells. *Journal of the American Chemical Society* **2005,** *127* (38), 13100-13101.

208. Kariuki, N. N.; Wang, X.; Mawdsley, J. R.; Ferrandon, M. S.; Niyogi, S. G.; Vaughey, J. T.; Myers, D. J., Colloidal synthesis and characterization of carbon-supported Pd− Cu nanoparticle oxygen reduction electrocatalysts. *Chemistry of Materials* **2010,** *22* (14), 4144-4152.

209. Shao, M., Palladium-based electrocatalysts for hydrogen oxidation and oxygen reduction reactions. *J. Power Sources* **2011,** *196* (5), 2433-2444.

210. Wang, C.; Chen, D. P.; Sang, X.; Unocic, R. R.; Skrabalak, S. E., Size-Dependent Disorder–Order Transformation in the Synthesis of Monodisperse Intermetallic PdCu Nanocatalysts. *ACS nano* **2016,** *10* (6), 6345-6353.

211. Yan, Y.; Du, J. S.; Gilroy, K. D.; Yang, D.; Xia, Y.; Zhang, H., Intermetallic Nanocrystals: Syntheses and Catalytic Applications. *Advanced Materials* **2017**.

212. Antolini, E., Alloy vs. intermetallic compounds: effect of the ordering on the electrocatalytic activity for oxygen reduction and the stability of low temperature fuel cell catalysts. *Appl. Catal. B.* **2017**.

213. Jiang, G.; Zhu, H.; Zhang, X.; Shen, B.; Wu, L.; Zhang, S.; Lu, G.; Wu, Z.; Sun, S., Core/shell face-centered tetragonal FePd/Pd nanoparticles as an efficient non-Pt catalyst for the oxygen reduction reaction. *ACS nano* **2015,** *9* (11), 11014-11022.

214. Liu, J.; Fan, X.; Sun, C. Q.; Zhu, W., Layer effect on catalytic activity of Pd-Cu bimetal for CO oxidation. *Applied Catalysis A: General* **2017,** *538*, 66-73.

215. Nørskov, J. K.; Rossmeisl, J.; Logadottir, A.; Lindqvist, L.; Kitchin, J. R.; Bligaard, T.; Jonsson, H., Origin of the overpotential for oxygen reduction at a fuel-cell cathode. *J. Phys. Chem. B* **2004,** *108* (46), 17886-17892.

216. Greeley, J.; Norskov, J. K., Electrochemical dissolution of surface alloys in acids: Thermodynamic trends from first-principles calculations. *Electrochim. Acta* **2007,** *52* (19), 5829-5836.

217. Noh, S. H.; Han, B.; Ohsaka, T., First-principles computational study of highly stable and active ternary PtCuNi nanocatalyst for oxygen reduction reaction. *Nano Res* **2015,** *8* (10), 3394-3403.

218. Canzian, A.; Mosca, H. O.; Bozzolo, G., Atomistic modeling of Pt deposition on Cu (111) and Cu deposition on Pt (111). *Surface Review and Letters* **2004,** *11* (02), 235-243.

219. Dastoor, P. C.; O'Connor, D. J.; MacLaren, D.; Allison, W.; Noakes, T.; Bailey, P., Step mediated surface alloy formation of Pt/Cu (1 1 1). *Surface science* **2005,** *588* (1-3), 101-107.

220. Liu, J., Catalysis by supported single metal atoms. *Acs Catal* **2016,** *7* (1), 34-59.

221. Fako, E.; Łodziana, Z.; López, N., Comparative single atom heterogeneous catalysts (SAHCs) on different platforms: a theoretical approach. *Catalysis Science & Technology* **2017,** *7* (19), 4285-4293.

222. Kim, J.; Roh, C. W.; Sahoo, S. K.; Yang, S.; Bae, J.; Han, J. W.; Lee, H., Highly Durable Platinum Single-Atom Alloy Catalyst for Electrochemical Reactions. *Advanced Energy Materials* **2018,** *8* (1).

223. Thirumalai, H.; Kitchin, J. R., Investigating the Reactivity of Single Atom Alloys Using Density Functional Theory. *Topics in Catalysis* **2018,** *61* (5-6), 462-474.

224. Zhang, H.; Liu, G.; Shi, L.; Ye, J., Single-Atom Catalysts: Emerging Multifunctional Materials in Heterogeneous Catalysis. *Advanced Energy Materials* **2018**.

225. Gates, B. C.; Flytzani-Stephanopoulos, M.; Dixon, D. A.; Katz, A., Atomically dispersed supported metal catalysts: perspectives and suggestions for future research. *Catalysis Science & Technology* **2017,** *7* (19), 4259-4275.

226. Zaera, F., The Surface Chemistry of Metal-Based Hydrogenation Catalysis. *Acs Catal* **2017,** *7* (8), 4947-4967.

227. Lucci, F. R.; Liu, J.; Marcinkowski, M. D.; Yang, M.; Allard, L. F.; Flytzani-Stephanopoulos, M.; Sykes, E. C. H., Selective hydrogenation of 1, 3-butadiene on platinum–copper alloys at the single-atom limit. *Nature communications* **2015,** *6*, 8550.

228. Cui, X.-H.; Duan, X.-M., The stability and electronic properties of Pt-modified Cu (1 1 0) and Cu (1 1 1) in the absence/presence of small molecules: a density-functional theory modeling. *Journal of Physics: Condensed Matter* **2016,** *28* (8), 085001.

229. Simonovis, J. P.; Hunt, A.; Palomino, R. M.; Senanayake, S. D.; Waluyo, I., Enhanced Stability of Pt-Cu Single-Atom Alloy Catalysts: In Situ Characterization of the Pt/Cu (111) Surface in an Ambient Pressure of CO. *The Journal of Physical Chemistry C* **2018,** *122* (8), 4488-4495.

230. Gao, F.; Wang, Y.; Goodman, D. W., CO oxidation over AuPd (100) from ultrahigh vacuum to near-atmospheric pressures: the critical role of contiguous Pd atoms. *Journal of the American Chemical Society* **2009,** *131* (16), 5734-5735.

231. Linke, R.; Schneider, U.; Busse, H.; Becker, C.; Schröder, U.; Castro, G.; Wandelt, K., Interaction of hydrogen with Cu3Pt (111): dissociation via isolated platinum atoms. *Surface science* **1994,** *307*, 407-411.

232. Lucci, F. R.; Lawton, T. J.; Pronschinske, A.; Sykes, E. C. H., Atomic scale surface structure of Pt/Cu (111) surface alloys. *The Journal of Physical Chemistry C* **2014,** *118* (6), 3015-3022.

233. Lucci, F. R.; Marcinkowski, M. D.; Lawton, T. J.; Sykes, E. C. H., H2 Activation and Spillover on Catalytically Relevant Pt–Cu Single Atom Alloys. *The Journal of Physical Chemistry C* **2015,** *119* (43), 24351-24357.

234. Marcinkowski, M. D.; Liu, J.; Murphy, C. J.; Liriano, M. L.; Wasio, N. A.; Lucci, F. R.; Flytzani-Stephanopoulos, M.; Sykes, E. C. H., Selective formic acid dehydrogenation on Pt-Cu single-atom alloys. *Acs Catal* **2016,** *7* (1), 413-420.

235. Marcinkowski, M. D.; Darby, M. T.; Liu, J.; Wimble, J. M.; Lucci, F. R.; Lee, S.; Michaelides, A.; Flytzani-Stephanopoulos, M.; Stamatakis, M.; Sykes, E. C. H., Pt/Cu single-atom alloys as coke-resistant catalysts for efficient C–H activation. *Nature Chemistry* **2018**.

236. Cao, X.; Fu, Q.; Luo, Y., Catalytic activity of Pd-doped Cu nanoparticles for hydrogenation as a single-atom-alloy catalyst. *Physical Chemistry Chemical Physics* **2014,** *16* (18), 8367-8375.

237. Darby, M. T.; Reocreux, R.; Sykes, E. C. H.; Michaelides, A.; Stamatakis, M., Elucidating the Stability and Reactivity of Surface Intermediates on Single Atom Alloy Catalysts. *Acs Catal* **2018**.